T H E U N I V E R S I T Y O F M I C H I G A N

COLLEGE OF ENGINEERING
Department of Chemical and Metallurgical Engineering

Technical Report

THE PLASTIC DEFORMATION OF MAGNESIUM

E. W. Kelley
W. F. Hosford, Jr., Project Director

ORA Project 07164

under contract with:

U. S. ARMY RESEARCH OFFICE-DURHAM
CONTRACT NO. DA-31-124-ARO-D-321
DURHAM, NORTH CAROLINA

administered through:

OFFICE OF RESEARCH ADMINISTRATION ANN ARBOR

February 1967

This report was also a dissertation submitted by the first author in partial fulfillment of the requirements for the degree of Doctor of Philosophy in The University of Michigan, 1967.

TABLE OF CONTENTS

LIST OF TABLES

LIST OF FIGURES

The Plastic Deformation of Magnesium

by Eugene Wallace Kelley

ABSTRACT

Deformation studies have been conducted at room temperature on single crystals and textured polycrystals of magnesium and magnesium alloys with thorium and with lithium. Single crystals oriented to suppress shear on the easily activated basal slip systems were deformed by plane-strain compression. Compression along the c-axis was accommodated by $\{10\bar{1}1\}$ banding. Compression perpendicular to the unconstrained c-axis activated $\{10\bar{1}2\}$ twinning, and, after virtually complete twinning, deformation continued by $\{10\bar{1}1\}$ banding in the twinned material. Compression perpendicular to the constrained c-axis was accommodated by the simultaneous operation of $\{10\bar{1}2\}$ twinning against the constraint and $\{10\bar{1}1\}$ banding. Although this orientation was favorable for $\{10\bar{1}0\}\langle 1\bar{2}10\rangle$ prism and $\{10\bar{1}1\}\langle 1\bar{2}10\rangle$ pyramidal slip, these modes were not observed in pure magnesium or in Mg-.5%Th. However, $\{10\bar{1}0\}\langle 1\bar{2}10\rangle$ prism slip was active in crystals of Mg-4%Li during compression perpendicular to the constrained c-axis. Fracture in all materials occurred parallel to $\{11\bar{2}4\}$ or $\{10\bar{1}1\}$ depending on the orientation and composition of the specimen.

Anisotropy of strength in textured polycrystals was determined in uniaxial compression and tension as well as plane-strain compression. The results are correlated with the orientation texture and the deformation modes observed in single crystals, and have been used to establish yield loci for the materials.

INTRODUCTION

Metals which crystallize in the hexagonal close packed (HCP) structure are becoming more and more important as engineering performance requirements increase with the growing technology. The various combinations of strength, density and high temperature properties that can be attained in these metals make them extremely useful in many applications. The mechanical behavior of the HCP metals is strongly influenced by the inherent anisotropy that results from the HCP crystallographic structure. Although a variety of slip systems have been reported the slip is commonly in the directions of closest packing, the $\langle 1\bar{2}10 \rangle$.(1) Because $\langle 1\bar{2}10 \rangle$ slip directions are confined to the basal plane the slip modes do not produce strains parallel to the c-axis. Hence the inherent anisotropy.

Magnesium, a HCP metal, has been structurally important for many years because of its high strength-to-weight characteristics. At room temperature the deformation mode most easily activated is $(0001)\langle 1\bar{2}10 \rangle$ basal slip. $\{10\bar{1}0\}\langle 1\bar{2}10 \rangle$ prism slip and $\{10\bar{1}1\}\langle 1\bar{2}10 \rangle$ pyramidal slip have also been reported in magnesium, primarily at elevated temperatures. (2,3,4) However, at room temperature the resolved shear stresses to activate the prism and pyramidal modes are in excess of a hundred-fold greater than that required to initiate basal slip. Thus prism and pyramidal

slip may be expected to occur only under special conditions of loading. Because all three of these deformation modes have $\langle 1\bar{2}10\rangle$ slip directions, none of them, either singly or in combination with the others, can produce strains out of the basal plane.

Strains normal to the basal plane can be produced by twinning, however. (5) Magnesium twinning modes which have been reported include $\{10\bar{1}1\}$, $\{10\bar{1}2\}$, $\{10\bar{1}3\}$, $\{10\bar{1}4\}$, $\{10\bar{1}5\}$, $\{11\bar{2}1\}$, and $\{11\bar{2}4\}$. (1) Of these, $\{10\bar{1}2\}$ twinning is by far the most common and is relatively easily activated by tension parallel, or compression perpendicular, to the c-axis. Twinning, of course, is dependent upon the sign of the shear stress. If a shear in one direction can activate a given twinning mode a shear in the opposite direction cannot. Thus magnesium can deform by $\{10\bar{1}2\}$ twinning when stressed by tension along the c-axis but cannot deform by this mode when compressed along the c-axis. $\{10\bar{1}1\}$ twinning on the other hand is activated in magnesium by compression along the c-axis and not by tension.

In addition to primary twinning it is possible for secondary twinning or slip to occur within the reoriented material of primary twins. (6) For this reason many combined deformation systems are theoretically possible although the only systems that become active are those that require the least resolved shear stresses for the loading and constraint conditions imposed.

Plastic deformation within the individual grains of a polycrystalline aggregate must occur by the activation of crystallographic deformation modes. Because the individual grains are constrained by their neighbors it is seldom that a grain is able to plastically deform by basal slip alone. In general at least five independent shear systems must be available to bring about an arbitrary shape change such as that which must be accommodated in the individual grains of a deforming polycrystalline material. (7) In magnesium this requirement means that in some grains, depending upon their crystallographic orientation with respect to the load, deformation modes other than basal slip and primary $\{10\bar{1}2\}$ twinning must be brought into play. If the complete deformation characteristics of a magnesium polycrystalline aggregate are to be properly understood, all of the possible deformation modes must be identified and investigated.

Researchers in the past have made observations upon the less common deformation modes through the examination and crystallographic analysis of either deformed polycrystalline aggregates or oriented single crystals. Much of the work in such investigations has involved deformation resulting from uniaxial tension or, in fewer instances, from uniaxial compression. These two methods of loading can initiate all of the possible deformation modes in polycrystalline aggregates but the identification of the less common modes becomes extremely arduous and the direct

evaluation of the resolved shear stresses to activate them is not feasible. In oriented single crystals, however, some of the possible deformation modes are not activated by uniaxial tension or compression. This is because the easily activated basal slip and $\{10\bar{1}2\}$ twinning modes cannot both be suppressed simultaneously under uniaxial loading in most of the many orientations which can occur in a polycrystalline material. The only two exceptions are tension perpendicular to the c-axis and compression along the c-axis.

By deforming oriented single crystals under conditions of plane-strain compression it should be possible to activate all possible deformation modes. Single crystal specimens carefully prepared should also make the identification of active deformation systems relatively easy and should permit direct evaluation of the resolved shear stresses required to activate such systems. Wonsiewicz and Backofen (8) have recently completed an investigation of pure magnesium at various temperatures utilizing plane-strain compression of single crystals. Through the selective crystallographic orientation of the monocrystals they were able to suppress both basal slip and $\{10\bar{1}2\}$ twinning and thereby force other deformation modes that require higher shear stresses for activation.

In planning the present work it was thought that by loading single crystals under plane-strain compression in various specific crystallographic orientations it would be

possible to initiate, identify and evaluate all of the possible modes that can participate in the deformation of the materials of interest. Thus, plane-strain compression along the c-axis should activate some deformation mode other than basal, prism or pyramidal slip, or $\{10\bar{1}2\}$ twinning. This is because compressive stress along the c-axis is perpendicular to the $\langle 1\bar{2}10\rangle$ slip direction of basal, prism or pyramidal slip and is in the opposite direction of that necessary for $\{10\bar{1}2\}$ twinning. In another crystal orientation where the material is compressed perpendicular to the c-axis while c-axis elongation is constrained, prism or pyramidal slip would be expected to take place. In this orientation basal slip is suppressed because the load is applied parallel to the basal plane with no possibility for shear strain and $\{10\bar{1}2\}$ twinning is suppressed by the c-axis constraint of the plane-strain condition. In a third crystal orientation where the compressive load is applied perpendicular to an unconstrained c-axis the three slip modes would be suppressed but not $\{10\bar{1}2\}$ twinning.

The primary objectives of the present investigation were to study the various deformation modes in magnesium with special emphasis on those that are less easily activated, to investigate the effects of certain alloying elements upon the deformation of magnesium, and to relate the plastic deformation characteristics of textured polycrystalline magnesium to the deformation modes that are

found to be active in single crystals. The two alloying elements, thorium and lithium, both commercially important, were to be used in that part of the work involving the study of alloying effects.

In view of the foregoing an experimental program was initiated to deform by plane-strain compression various orientations of single crystal specimens of pure magnesium as well as thorium and lithium alloys of magnesium. The active deformation modes were to be identified by examination of the specimens after compression, and the stress-strain relationships for the various modes were to be evaluated from the load-deformation data taken during compression. In addition, similar plane-strain compression tests plus uniaxial tension and compression tests were to be conducted upon textured polycrystalline specimens of the same alloys. Because of the scope of the experimental program only room temperature testing was planned.

EXPERIMENTAL PROCEDURE

Single crystal production

The initial requirement in the experimental program was to produce single crystals of a suitable size, shape and crystallographic orientation for subsequent testing under conditions of plane-strain compression. The raw materials were three textured sheets provided by Dow Chemical Company. These had received approximately 80% reduction in the process of being hot-rolled to their final 1/4 in. thicknesses. The nominal compositions of the sheets were pure magnesium, Mg-.5%Th and Mg-4%Li. Analyses, also furnished by Dow, for the textured sheets and for single crystals grown from the alloy sheets, are given in Table 1.

Table 1.

Magnesium Alloy Compositions

	Pure Mg	Mg-Th		Mg-Li	
	Sheet	Sheet	Xtals	Sheet	Xtals
Al	<.0005%	<.0005%	<.03	<.0005%	<.03
Ca	<.01	<.01	<.01	<.01	<.01
Cu	<.001	<.001	<.001	<.001	<.001
Fe	.001	.002	.004	.014	.015
Mn	<.0006	<.0006	<.01	<.0006	<.01
Ni	<.001	<.001	<.001	<.001	<.001
Pb	<.003	<.003	<.01	<.003	<.01
Si	<.001	<.001	<.01	<.001	<.01
Sn	<.001	<.001	<.01	<.001	<.01
Zn	<.01	<.01	<.02	<.01	<.02
Th	-	.49	.30-.50	-	-
Li	-	-	-	3.84	3.2-3.8
Mg	>99.97	>99.48	>99.4	>96.11	>96.1

For each of these compositions single crystals approximately 1/4 in. by 1/2 in. by 6 in. were grown to furnish specimens of specific crystallographic orientations. The seven desired orientations and the code letters which have been assigned to facilitate their identification are indicated in Table 2.

The single crystals were grown from the melt in graphite molds by a modified Bridgeman method utilizing oriented seed crystals. A flowing helium atmosphere was used in the crystal furnace. Seeds were aligned and the orientations of single crystals were checked by the Laue back reflection x-ray method. The details of the crystal growing procedure are presented in Appendix A.

Preparation of specimens for testing

Single crystals were carefully removed from the graphite mold and lightly cleaned with 10% HCl. Those determined by x-ray to be within 2° of the desired orientation were sectioned with an acid saw into compression test specimens roughly 3/8 in. in length. Because the surfaces of the crystals were considered to be too rough in the as-grown condition to permit satisfactory results in the compression tests the specimens were carefully polished successively on wet 400 and 600 grit silicon carbide papers. This was followed by a light chemical polish with 10% HNO_3 to remove the markings and minute surface twins that were produced by the mechanical

Table 2.

Single Crystal Orientations
used in Plane-strain Compression Testing

Assigned Identification	Orientation	Compression Direction	Constraint Direction
A	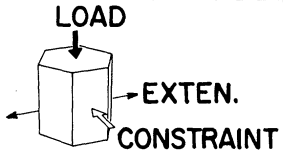	⟨0001⟩	⟨10$\bar{1}$0⟩
B	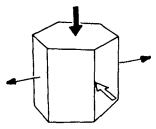	⟨0001⟩	⟨1$\bar{2}$10⟩
C	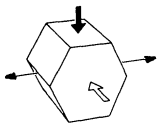	⟨10$\bar{1}$0⟩	⟨0001⟩
D	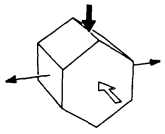	⟨1$\bar{2}$10⟩	⟨0001⟩
E	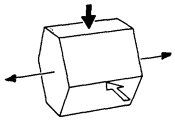	⟨10$\bar{1}$0⟩	⟨1$\bar{2}$10⟩
F	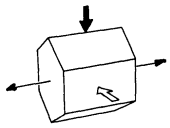	⟨1$\bar{2}$10⟩	⟨10$\bar{1}$0⟩
G	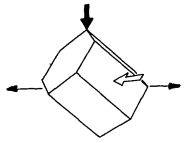	⟨0001⟩@45°	⟨10$\bar{1}$0⟩

polishing. The resulting test specimens, with a nominal size of 1/4 in. thick by 3/8 in. long by 1/2 in. wide, were smooth to within an estimated .0002 in. with sides parallel to within .0002 in. and with all six surfaces polished for metallographic examination.

Textured polycrystalline specimens were prepared for testing in a manner similar to that used for single crystals. They were cut from the 1/4 in. sheet material with a silicon carbide wheel and sized, shaped and mechanically polished on wet 400 and 600 grit papers. The specimens were prepared in the six orientations of interest, these being the six combinations of rolling, transverse and thickness directions serving as loading, extension and constraint directions in the plane-strain compression test. All polycrystalline specimens were stress-relieved at 550°F for one-half hour as the final step in their preparation for testing.

Specimen testing

Test specimens were plastically deformed under conditions of plane-strain compression in a hardened steel fixture incorporating an adjustable-width channel (Fig. 1). Five interchangeable steel indentors with slightly varying widths were used so that specimens .480 in. to .500 in. wide could be tested under width constraint. The indentors, which were .450 in. long, extended beyond both ends of most specimens. A few specimens longer than the indentors were

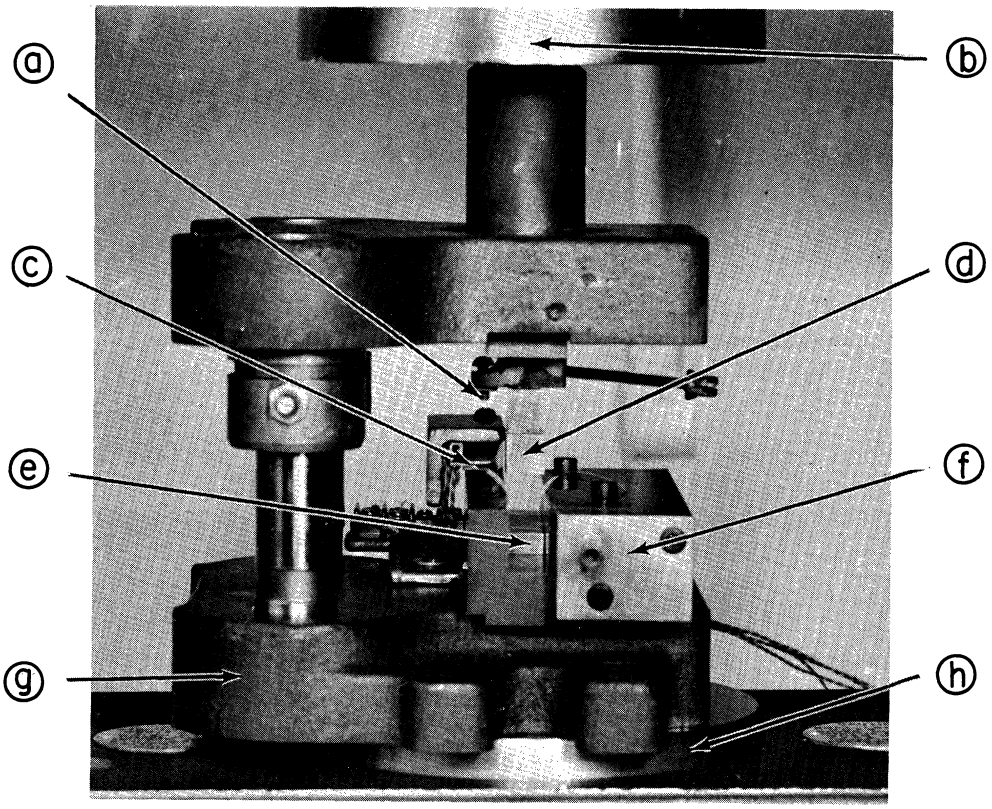

Fig. 1. Plane-strain compression fixture. (a) Deflectometer actuator, (b) Instron crosshead, (c) deflectometer, (d) indentor, (e) specimen, (f) adjustable-width fixture, (g) die holder, (h) compression load cell.

tested without appreciably different results.

During compression testing a 2-mil teflon film between the specimen and the test fixture acted as a lubricant and also served to cushion the specimen surfaces and protect them from smearing as deformation occurred. This protection was sufficient to permit direct microscopic observation of the deformed surfaces.

To insure reproducibility, at least four duplicate monocrystal specimens of each of the six crystallographic orientations A through F were tested in each of the three compositions under study. Crystals of the G (or easy basal glide) orientation were prepared and tested only for pure magnesium. At least three duplicate polycrystalline specimens were tested for each of the six orientations for each of the three compositions. The textured materials were also tested in uniaxial compression in the rolling, transverse and thickness directions, and in uniaxial tension in the rolling and transverse directions. The uniaxial tests supplemented those in plane-strain compression to provide data for the construction of yield loci for each of the three textured materials. In addition to the textured specimens one set of randomly oriented polycrystalline specimens of pure magnesium was prepared and tested in plane-strain compression. The experimental details of the testing procedure are given in Appendix B.

Determination of pole figures

Basal pole figures of the three textured polycrystalline materials were determined by x-ray diffractometer reflection. The resulting pole figures are presented in Figs. 17, 19 and 21.

Evaluation of frictional effects

Uniaxial compression test results are inherently in error owing to the frictional resistance to sliding that occurs between the specimen and the loading platens. For plane-strain compression in a channel these effects are even greater because of the added frictional resistance imposed by the channel walls. The friction was reduced and made reasonably consistent in this investigation by the use of the teflon film, but its role could not be neglected.

The magnitude of the frictional effect was evaluated by comparing the results obtained from compressive and tensile tests made on aluminum, an essentially isotropic material. The frictional contribution in the compression tests was taken to be that compressive true stress in excess of the tensile true stress for a corresponding true strain. From these experiments correction factors, f, were determined which have been used to convert all observed values of compressive stress to frictionless values. These factors are:

$$f_{\text{plane-strain}} = .89$$

$$f_{\text{uniaxial}} = .91$$

An analysis of the frictional effects involved in compression testing is presented in Appendix C.

Analysis of the data

The plane-strain compression tests, as well as the uniaxial compression and tension tests, provided load vs. plastic deformation data which were converted to true stress vs. true strain using the relationships:

(1) $\epsilon_{true} = \ln (L/L_o)$ true strain

(2) $\sigma_{true} = f\ P/\ A_o\ e^{-\epsilon}{}_{true}$ true stress

where: L = specimen height in loading direction

A_o = specimen original area normal to the loading direction

P = applied load

f = correction factor for friction

The specimens were examined microscopically prior to compression testing and again after testing. Direct post-compression observation of the as-deformed surfaces was possible because of the protection to those surfaces provided by the teflon film. Active deformation modes were identified in the specimens by three-surface trace analysis. A few specimens were sectioned with an acid saw, mechanically polished, chemically polished and etched, and metallographically examined to check the interior structure.

RESULTS AND DISCUSSION

Pure magnesium single crystal deformation

The plane-strain compression stress-strain curves for the pure magnesium crystals are given in Figs. 2, 4 and 5. Fig. 2 shows the results of the compression along the c-axis (orientations A and B). The results of compression perpendicular to the unconstrained c-axis (orientations E and F) where $\{10\bar{1}2\}$ twinning is not suppressed are presented in Fig. 4. Fig. 5 gives the results of compression perpendicular to the constrained c-axis (orientations C and D) where $\{10\bar{1}2\}$ twinning is resisted. Easy basal glide results obtained from the compression of orientation G are presented in Fig. 4.

Compression along the c-axis: The curves for orientations A and B (Fig. 2) differ significantly only in the values of fracture stress. Both orientations work hardened rapidly up to about 4% strain at a loading stress of 43 to 45 ksi. A decreasing slope at this point led to abrupt failure within a fraction of a percent additional strain. The dominant modes responsible for each of the three portions of the curves are discussed below.

The initial 4% strain is attributed to $(0001)\langle 1\bar{2}10\rangle$ basal slip since traces on this system were the only ones observed. Although c-axis compression would not activate basal slip if the alignment of the compression axis with the

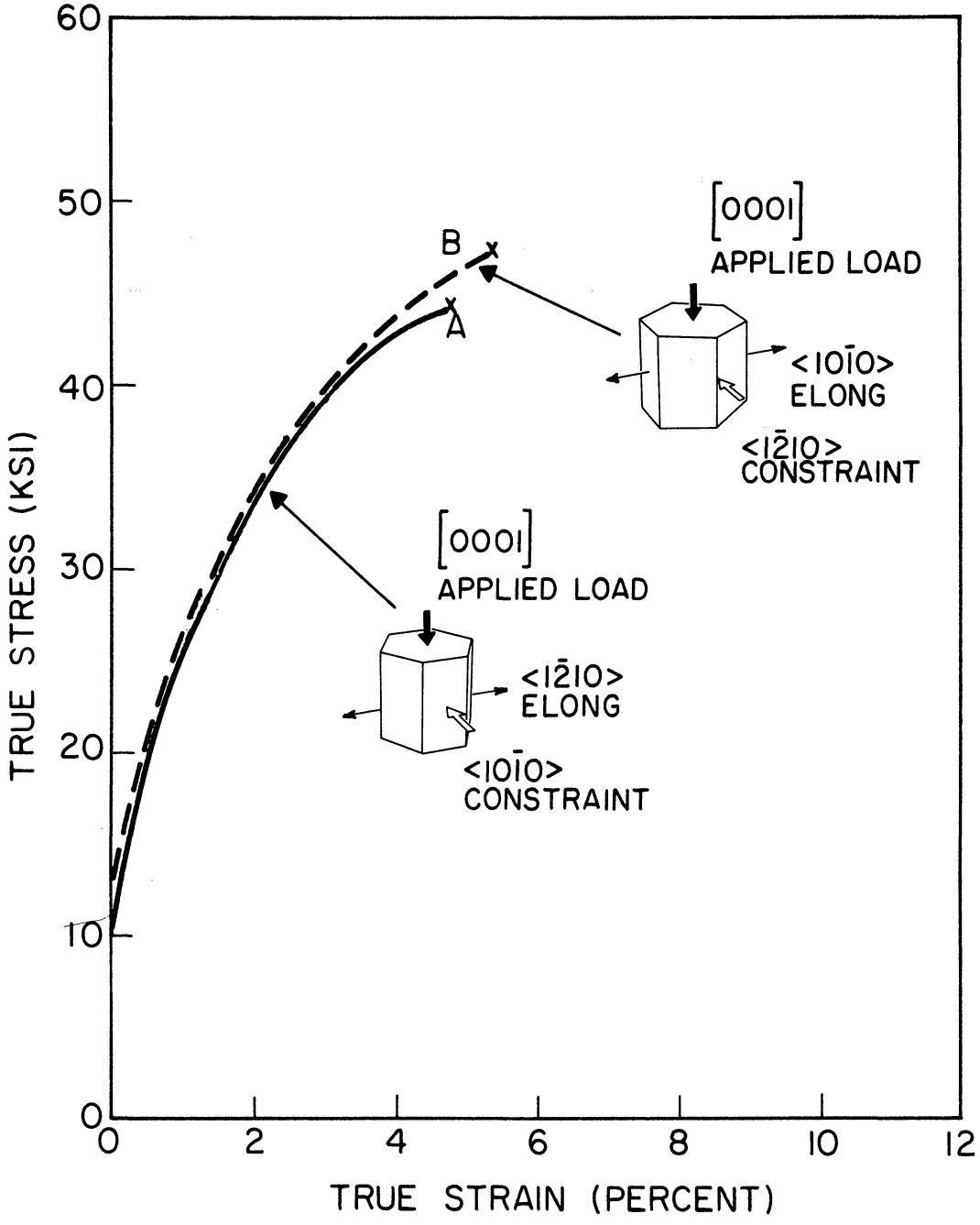

Fig. 2. Stress vs. Strain in Pure Magnesium Single Crystals compressed along the c-axis.

c-axis were ideal, only a very slight misalignment would be required for the basal slip systems to operate. Using values of τ = 70 psi for the critical resolved shear stress (2,9,14) and σ = 10 ksi as the compressive stress to produce the first plastic strain (see Fig. 2), Schmid's law, $\tau = \sigma \cos\phi \cos\lambda$, is satisfied when ϕ (the angle between the compression and c axes) is only .4° or larger. Since a misalignment of this magnitude is not at all unreasonable, basal slip should not be unexpected. Although the slight misalignment that is involved can not account for 4% strain by itself, surface asperities and imperfect constraint in conjunction with a small misalignment may well account for the initial strain in the curves of Fig. 2.

At stresses above ~40 ksi, sharp bands parallel to $\{10\bar{1}1\}$ were observed in both orientations. The decreased work hardening just prior to fracture undoubtedly resulted from the deformation associated with these bands. Such bands have been explained by Couling, Pashak and Sturkey (10) and by Reed-Hill (11) as resulting from $\{10\bar{1}1\}$ twins followed almost immediately by $\{10\bar{1}2\}$ retwinning and then by basal slip within the doubly twinned material.

Fracture occurred along $\{11\bar{2}4\}$ planes as can be observed in the specimen shown in Fig. 3. No evidence was found to indicate that $\{11\bar{2}4\}$ slip or $\{11\bar{2}4\}$ twinning occurred as a prelude to $\{11\bar{2}4\}$ fracture. The fracture stress for orientation B, where constraint was imposed

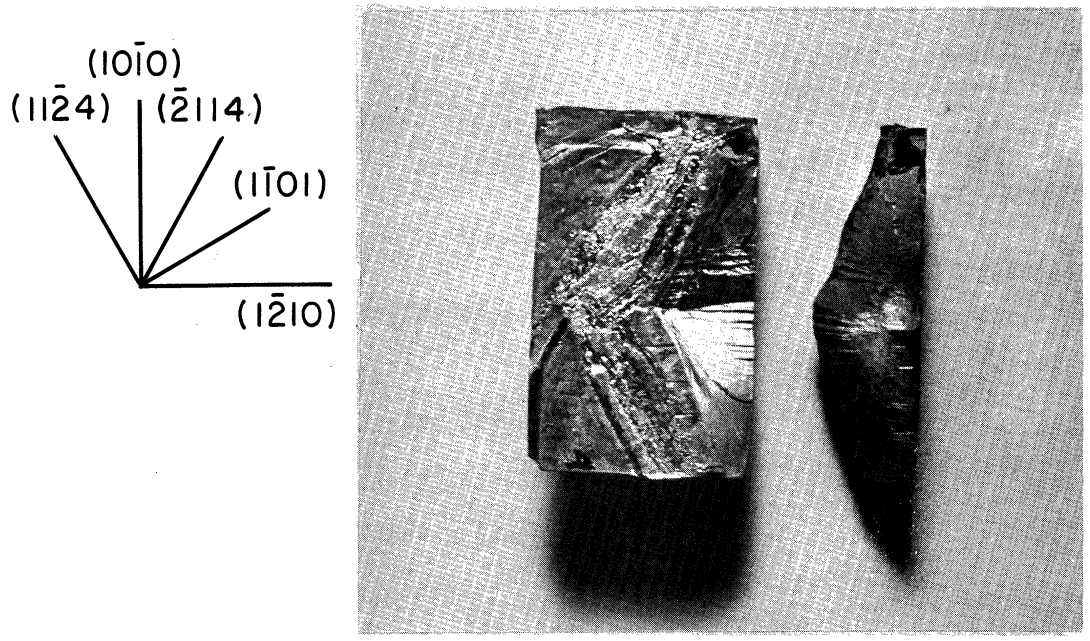

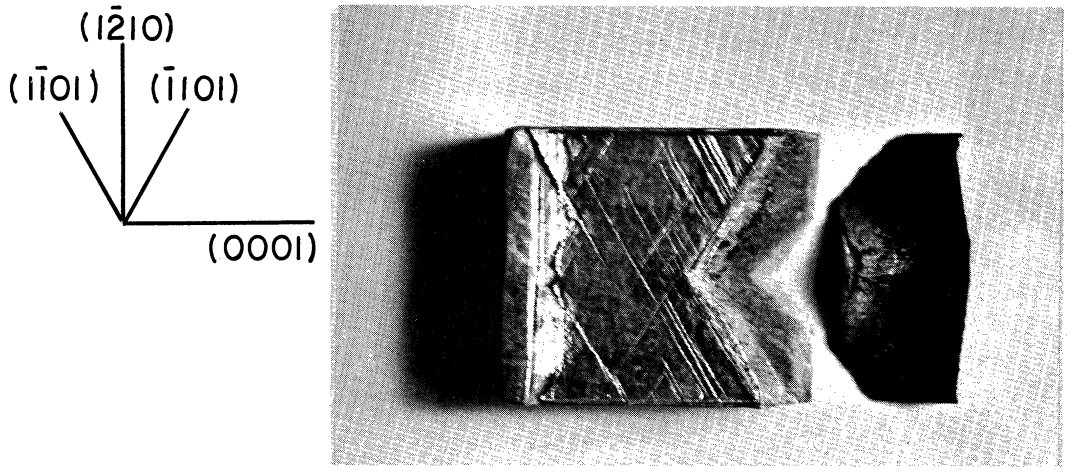

Fig. 3. Fractures in Pure Magnesium Single Crystals. Top: The (0001) compression surface showing $\{11\bar{2}4\}$ fracture in a B-oriented specimen. Bottom: The $\{10\bar{1}0\}$ compression surface in a C-oriented specimen showing $\{10\bar{1}1\}$ fracture. The sharp lines on the top surface of the specimen are $\{10\bar{1}1\}$ traces. Note: In both specimens the small portion on the right has been tipped 90° to better see the fracture surface.

along a $\langle 1\bar{2}10 \rangle$ direction, was significantly greater than that for orientation A where constraint was imposed along a $\langle 10\bar{1}0 \rangle$ direction. This is consistent with the fact that shear on active $\{11\bar{2}4\}$ planes is resisted in orientation B by a component of the constraint stress, whereas in orientation A this is not the case. Couling (12) has reported $\{11\bar{2}4\}$ fracture under compression in an environment of high hydrostatic pressure, and this fracture habit has also been observed by Reed Hill and Robertson (13) for magnesium under tension at -190°C. Wonsiewicz and Backofen (8), on the other hand, did not observe $\{11\bar{2}4\}$ fracture under conditions of plane-strain compression similar to those of this investigation. Instead, in the limited number of specimens which they strained to fracture they reported the fracture surface orientation to be "variable".

Magnesium compressed along the c-axis should not undergo $\{10\bar{1}2\}$ twinning because this mode produces an extension in the c-axis direction. In spite of this numerous $\{10\bar{1}2\}$ twins were found in specimens which had been compressed in orientations A and B. Wonsiewicz and Backofen (8) also observed this twinning mode under similar circumstances and experimentally determined that the $\{10\bar{1}2\}$ twins which occur in compression along the c-axis are actually generated by residual stresses during the unloading of the compressive force.

Compression perpendicular to the unconstrained c-axis: In plane-strain orientations E and F $\{10\bar{1}2\}$ twinning is not

suppressed. Deformation by this mode was therefore expected to proceed until the crystals were completely twinned at about 6% strain and other deformation modes were then expected to come into play in the reoriented material to accommodate further strain. These expectations were borne out by the results that are presented in Fig. 4.

$\{10\bar{1}2\}$ twinning was initiated in orientation E at a loading stress of perhaps 1,000 psi, with the two equally favored twinning systems producing lattice rotations of the opposite sense. After the $\pm 86.3^{\circ}$ reorientation due to twinning the crystal was only $\sim 3.7^{\circ}$ away from a B orientation. At ~6% strain, twinning was complete (the theoretical strain for complete $\{10\bar{1}2\}$ twinning in pure magnesium is 6.4%) and the stress then rose sharply to a maximum of slightly over 50 ksi at a total strain of 9%. $\{10\bar{1}1\}$ banding within the essentially B-oriented material was evident during the final fraction of a percent strain and fracture occurred primarily along $\{11\bar{2}4\}$ planes, with some fracture segments along $\{10\bar{1}1\}$. Thus the deformation of the fully twinned crystals was almost identical to that of B-oriented specimens as described previously. Crystals of E orientation exhibited a fracture strength 8 to 10% greater than that of B-oriented crystals and this is attributed to the strengthening of the E-oriented crystals by the twin boundaries generated during the initial $\{10\bar{1}2\}$ twinning process.

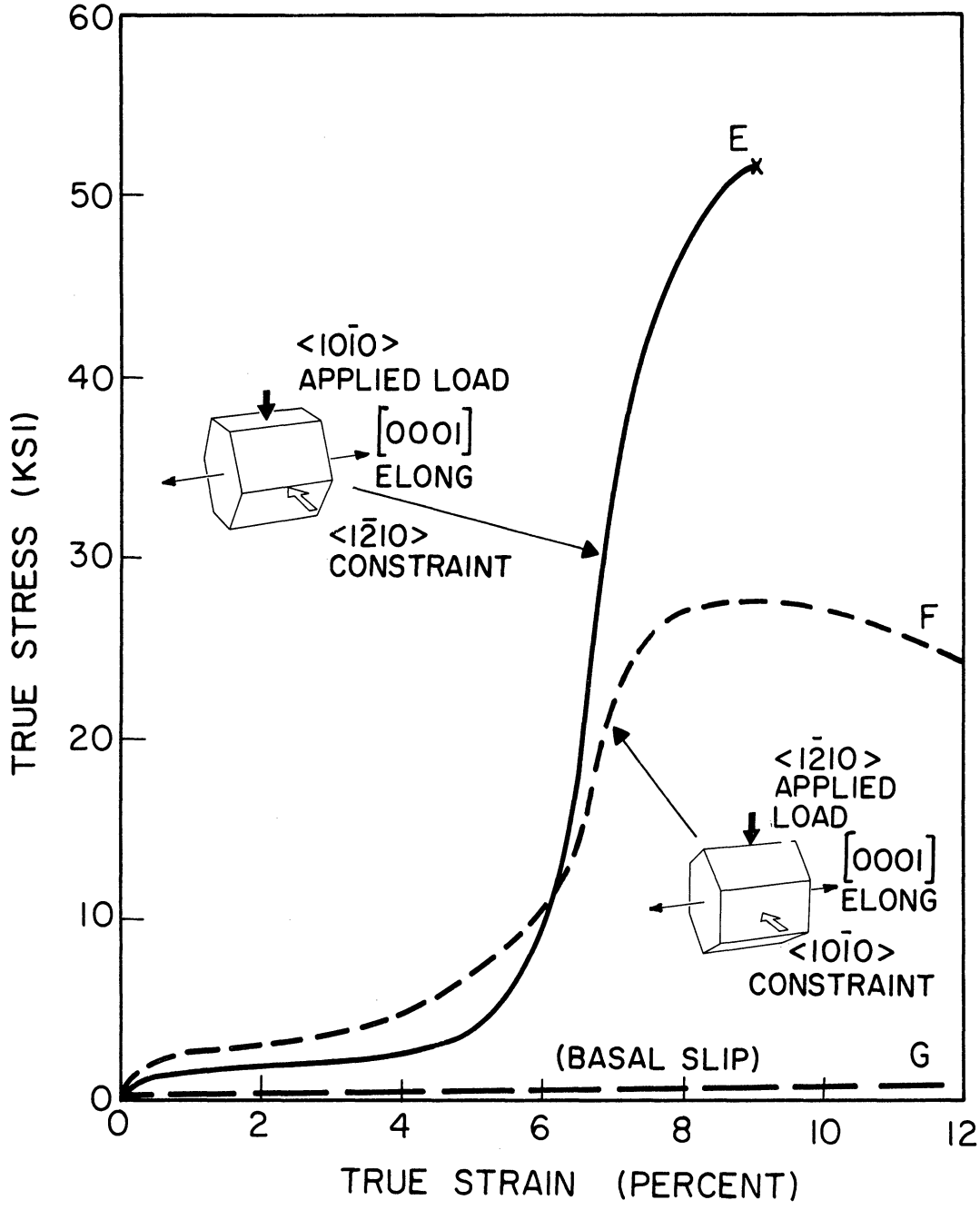

Fig. 4. Stress vs. Strain in Pure Magnesium Single Crystals compressed perpendicular to the unconstrained c-axis, and compressed to activate easy basal glide.

F-oriented single crystals deformed in general very much like those of E orientation in that $\{10\bar{1}2\}$ twinning produced an initial strain of about 6% (because of the orientation the theoretical strain in the compression direction for complete $\{10\bar{1}2\}$ twinning of F-oriented crystals is 5.6%). This was followed by other deformation modes which produced additional strain within the twinned material. With the F orientation a greater loading stress is necessary to produce a given shear stress on the active $\{10\bar{1}2\}$ twin planes than with the E orientation. This explains the higher level of loading stress for the initial ~6% strain (Fig. 4). The four equally favored twinning systems reoriented the lattice so that the basal plane normal formed an angle of $\pm 31^{\circ}$ with the loading stress direction rather than the $\sim 3.7^{\circ}$ of the twinned E orientation. Because of the realignment the twinned F was favorable for basal slip although such slip was resisted by the side constraint imposed by the plane-strain fixture. Actually this constraint was relieved somewhat during the twinning because in this orientation the active $\{10\bar{1}2\}$ systems produce a slight contraction in the constraint direction. A small amount of basal slip was therefore able to operate within the twins.

As the strain continued beyond the ~6% to cause complete $\{10\bar{1}2\}$ twinning the stress increased moderately to a maximum of about 32 ksi at a strain of approximately 10% where $\{10\bar{1}1\}$ banding was activated within the reoriented lattice. When the strain was increased beyond this point

the crystal became so disrupted by the $\{10\bar{1}2\}$ twinning, basal slip, $\{10\bar{1}1\}$ banding, lattice rotation, kinking and cracking that the stress decreased again as the crystal continued to deform. It was not possible in the disrupted structure to identify a crystallographic fracture plane.

Compression perpendicular to the constrained c-axis: The plane-strain compression curves for orientations C and D (Fig. 5) differ markedly from those for compression along the c-axis. Since these are the most favorable orientations for $\{10\bar{1}0\}\langle 1\bar{2}10\rangle$ prism slip and $\{10\bar{1}1\}\langle 1\bar{2}10\rangle$ pyramidal slip, it was anticipated that one or both of these modes would be active. However, no traces of slip on these systems could be found. Instead, deformation occurred primarily by a combination of $\{10\bar{1}2\}$ twinning and $\{10\bar{1}1\}$ banding as shown in Fig. 6.

Although compression perpendicular to the c-axis tends to activate $\{10\bar{1}2\}$ twinning, this mode was not expected to operate since the lateral constraint in orientations C and D resisted the c-axis extension accompanying $\{10\bar{1}2\}$ twinning. However, constraint was not perfect because of the elasticity of the lubricating film, the test channel walls and the specimen itself, so a limited amount of $\{10\bar{1}2\}$ twinning could therefore occur. The resulting expansion against the constraint induced a lateral compressive stress which increased with the imposed load. When this lateral constraining stress reached a sufficiently high value, it caused $\{10\bar{1}1\}$ twinning. The c-axis contraction caused by

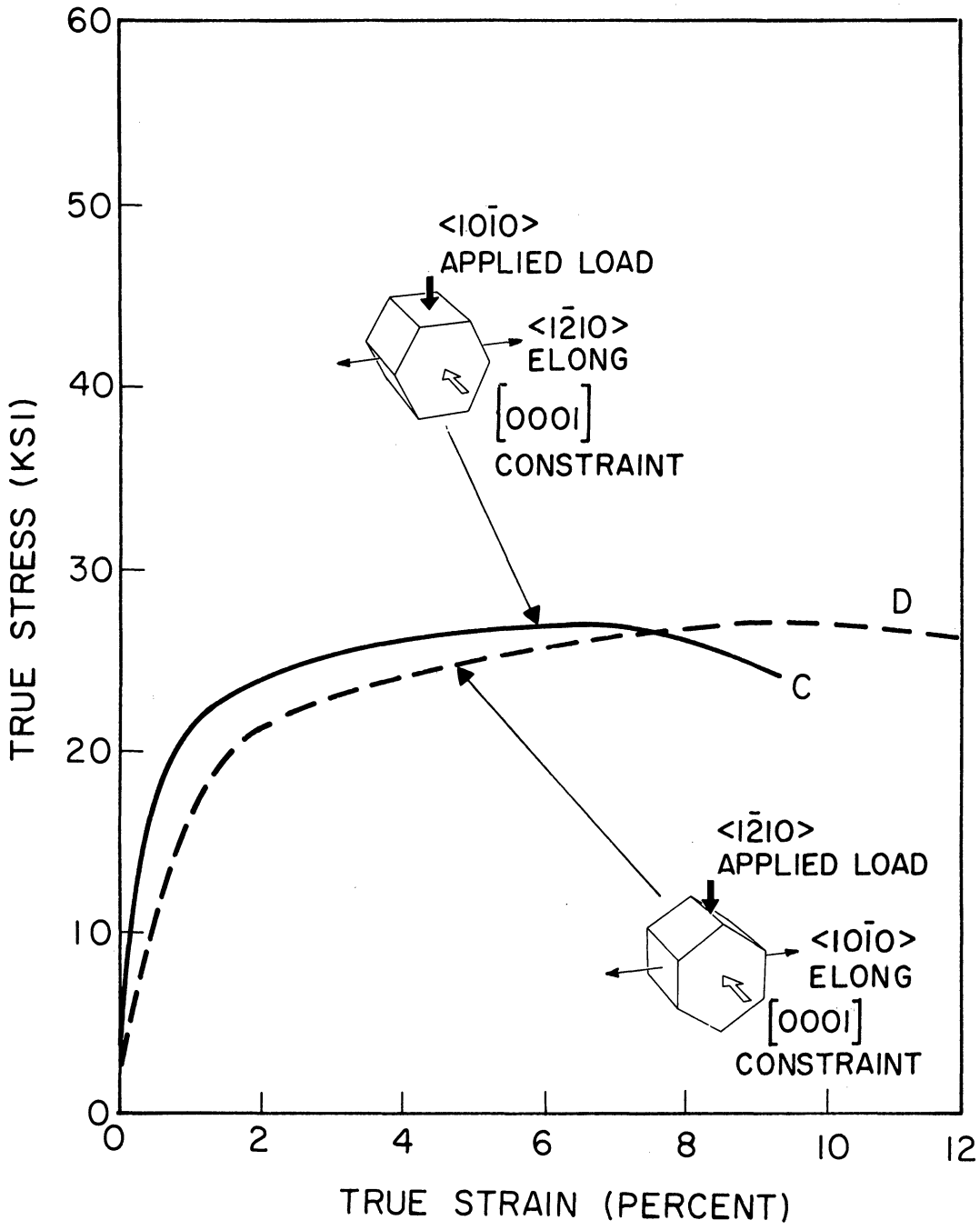

Fig. 5. Stress vs. Strain in Pure Magnesium Single Crystals compressed perpendicular to the constrained c-axis.

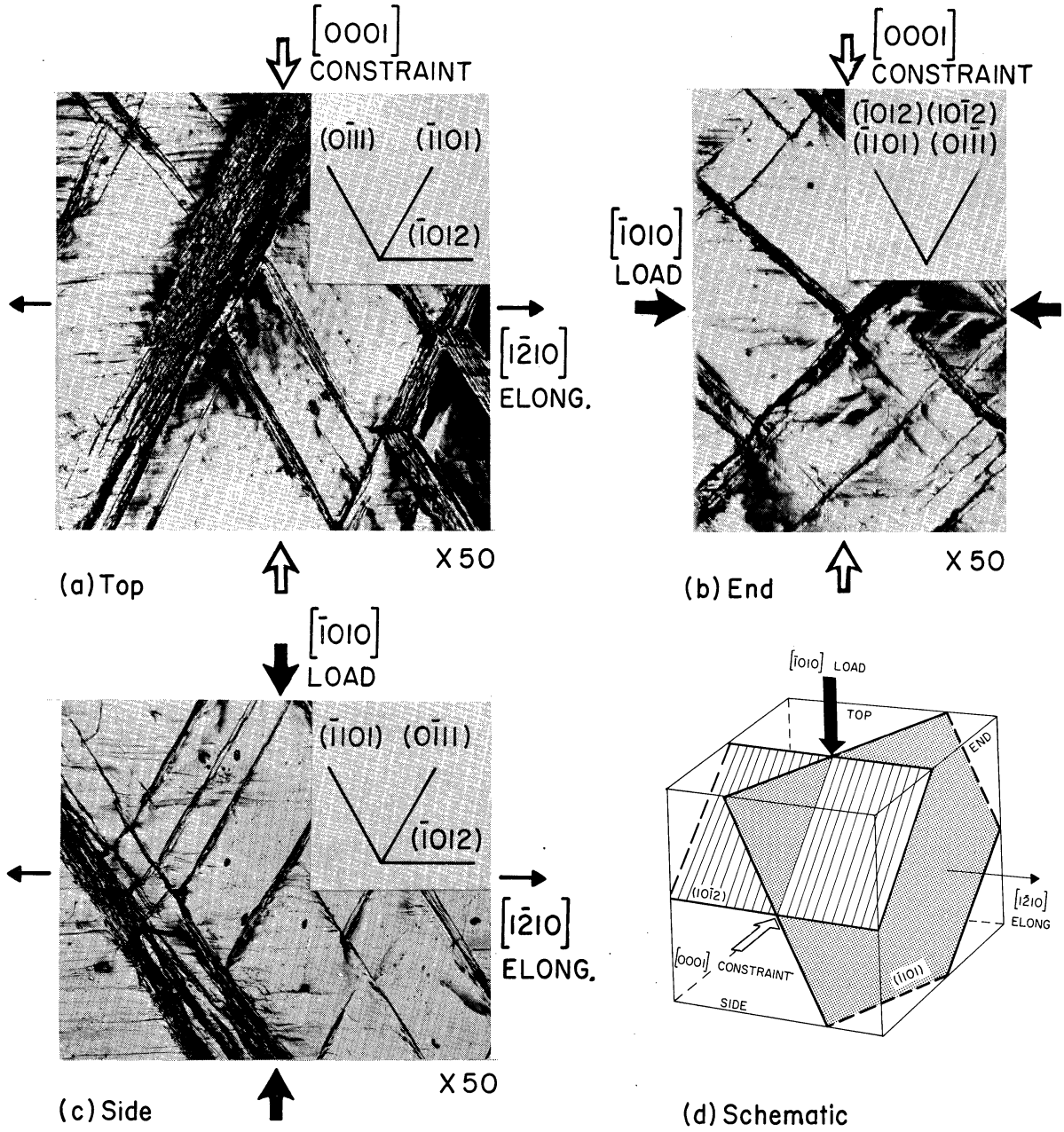

Fig. 6. Simultaneous {10$\bar{1}$2} Twinning and {10$\bar{1}$1} Banding in a C-oriented Single Crystal. Polished surfaces protected during deformation by teflon. (a) (10$\bar{1}$0) compression surface showing {10$\bar{1}$1} bands with band-widening and horizontal {10$\bar{1}$2} twins. (b) Unconstrained (1$\bar{2}$10) surface. Heavy traces are {10$\bar{1}$1} bands. (c) Constrained (0001) surface showing {10$\bar{1}$1} bands and horizontal {10$\bar{1}$2} twins. (d) Schematic. Only one each of two active {10$\bar{1}$2} and four active {10$\bar{1}$1} systems are depicted. The load causes {10$\bar{1}$2} twinning with extension against constraint, building up a constraining stress. This then causes {10$\bar{1}$1} twinning which leads to banding, and elongation in the unconstrained direction.

the $\{10\bar{1}1\}$ twins compensated for the simultaneous c-axis extension of the $\{10\bar{1}2\}$ twins. The $\{10\bar{1}1\}$ twinning initiated the $\{10\bar{1}1\}$ banding described earlier.

In view of the foregoing it is evident that the resolved shear stresses to activate prism and pyramidal slip at room temperature in magnesium are both greater than that to activate the combination of $\{10\bar{1}2\}$ twinning against constraint plus $\{10\bar{1}1\}$ banding. The experimental data shows that the loading stress for activating $\{10\bar{1}1\}$ banding for crystals of orientations C and D was about 20 ksi. For a stress of this magnitude, Schmid's law gives values of ~8.7 ksi for the resolved shear stress on operable prism planes and ~7.6 ksi on pyramidal planes. Since these modes were not observed, the shear stresses to initiate prism and pyramidal slip must be greater than ~8.7 ksi and ~7.6 ksi respectively in pure magnesium at room temperature. These results are in significant disagreement with those of previous investigators who have reported room temperature prism slip in magnesium in tension. (2, 4,15) Reed-Hill and Robertson (2) reported a CRSS of ~5.7 ksi for prism slip and Flynn, Mote and Dorn (4) reported ~7.5 ksi. Both values were based upon a very few specimens and Flynn, Mote and Dorn further reported that only extremely limited strain by prism slip occurred before fracture.

In an attempt to duplicate the experimental results of these investigators a monocrystal tensile specimen was

prepared with a $\{10\bar{1}0\}$ tensile axis and strained at a rate of .00005 sec^{-1}. This specimen underwent a limited amount of $\{10\bar{1}2\}$ twinning owing to inadvertant bending stresses during testing and then deformed by $\{10\bar{1}1\}$ banding at a loading stress of ~20 ksi (i.e., a resolved shear stress of ~8.7 ksi), which is identical to the value found by plane-strain compression. After a very small strain, fracture occurred on $\{10\bar{1}1\}$ planes. Again, no evidence of prism slip could be observed. If prism slip can be activated at room temperature by shear stresses less than 8.7 ksi as reported by Reed-Hill and the others, it must have been suppressed in this investigation by the duplex loading of the plane-strain conditions and/or the occurrence of $\{10\bar{1}2\}$ twinning.

The stress-strain curve for orientation C is significantly steeper than that for orientation D in the region of initial strain. The initial deformation in both cases was due to basal slip that occurred as a result of surface asperities and minor misalignment of the specimen with respect to the loading direction. $\{10\bar{1}2\}$ twinning activated against constraint also contributed to the initial strain. In the C orientation the two active $\{10\bar{1}2\}$ twinning systems reoriented the twinned material $\pm 86.3^{\circ}$ to a new crystallographic orientation where the twinned basal planes were almost normal to the loading direction, and basal slip within the twinned material was therefore suppressed.

In the D orientation however, the resolving factor was such that the resolved shear stress on the four active $\{10\bar{1}2\}$ twin planes was about 1/3 less than that in the C orientation for a given loading stress. Once the $\{10\bar{1}2\}$ twinning systems were activated in the D crystals though, the twinned material was realigned so that the twinned basal plane was $\pm 59^{\circ}$ out of the loading direction, making basal slip very favorable within the twins (see Fig. 8). Thus, under the initial loading stresses, orientation D could accommodate plastic deformation by basal slip within the twinned material whereas orientation C could not. This accounts for the difference in the slopes of the initial portions of the stress-strain curves.

In both orientations C and D, $\{10\bar{1}1\}$ banding was active at a loading stress of about 20 ksi after which the stress-strain curves were much less steep. Although the crystallographic resolution of stresses involved is different for the two orientations, the loading stresses for $\{10\bar{1}1\}$ banding were essentially the same in both C and D. Theoretically these loading stresses should be identical as is demonstrated in Appendix D.

Microscopic examination of C-oriented crystals showed that once the $\{10\bar{1}1\}$ bands were formed, additional deformation occurred by a widening of the bands as indicated in Fig. 6. Furthermore, it was apparent that the bulk of the deformation strain occurred within the $\{10\bar{1}1\}$ bands. The incremental steps that appeared on the surfaces of the

specimens could be associated with deformation in the $\{10\bar{1}1\}$ bands, and the material within the bands was almost entirely recrystallized at room temperature soon after the deformation occurred (see Fig. 7). This is indicative of a high degree of local strain within these deformation areas. The evidence strongly suggests that deformation within the $\{10\bar{1}1\}$ bands contributed directly to the further contraction of the crystal along the loading direction, rather than in conjunction with $\{10\bar{1}2\}$ twinning, once the bands were initiated. If this were not the case and all of the contraction did occur by $\{10\bar{1}2\}$ twinning, the loading stress would have been expected to increase sharply after the crystal had undergone complete $\{10\bar{1}2\}$ twinning (at no more than 6.4% strain). An increase in loading stress of this nature was not observed.

In the D orientation a different situation existed in that the $\{10\bar{1}1\}$ bands could not contribute directly to contraction in the loading direction because the bands formed principally along those $\{10\bar{1}1\}$ planes containing the loading direction. Post-deformation examination revealed little widening of the $\{10\bar{1}1\}$ bands in this orientation. Rather, basal slip within the $\{10\bar{1}2\}$ twins produced extensive deformation (see Fig. 8).

Single crystals of orientations C and D tended to undergo large strains before failure. Failures did occur, though not on $\{11\bar{2}4\}$ planes as was the case in orientations A and B. Instead, cracks appeared in C-oriented crystals

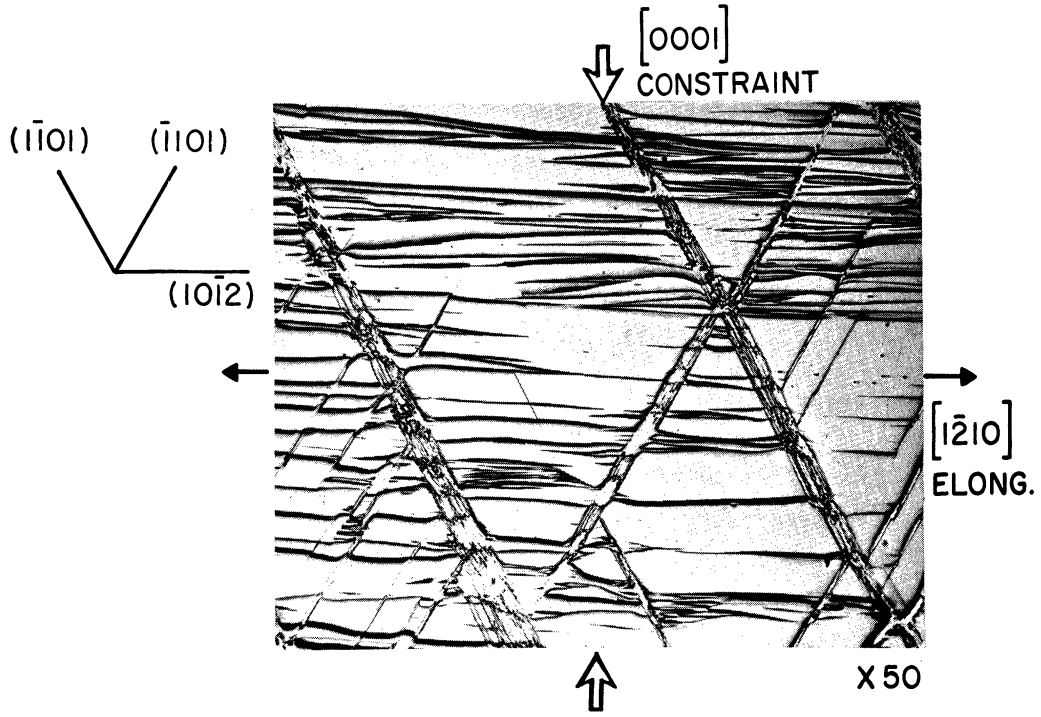

Fig. 7. (10$\bar{1}$0) compression surface of a c-oriented pure magnesium single crystal showing horizontal {10$\bar{1}$2} twins and recrystallization within {10$\bar{1}$1} bands. Polished and etched after deformation.

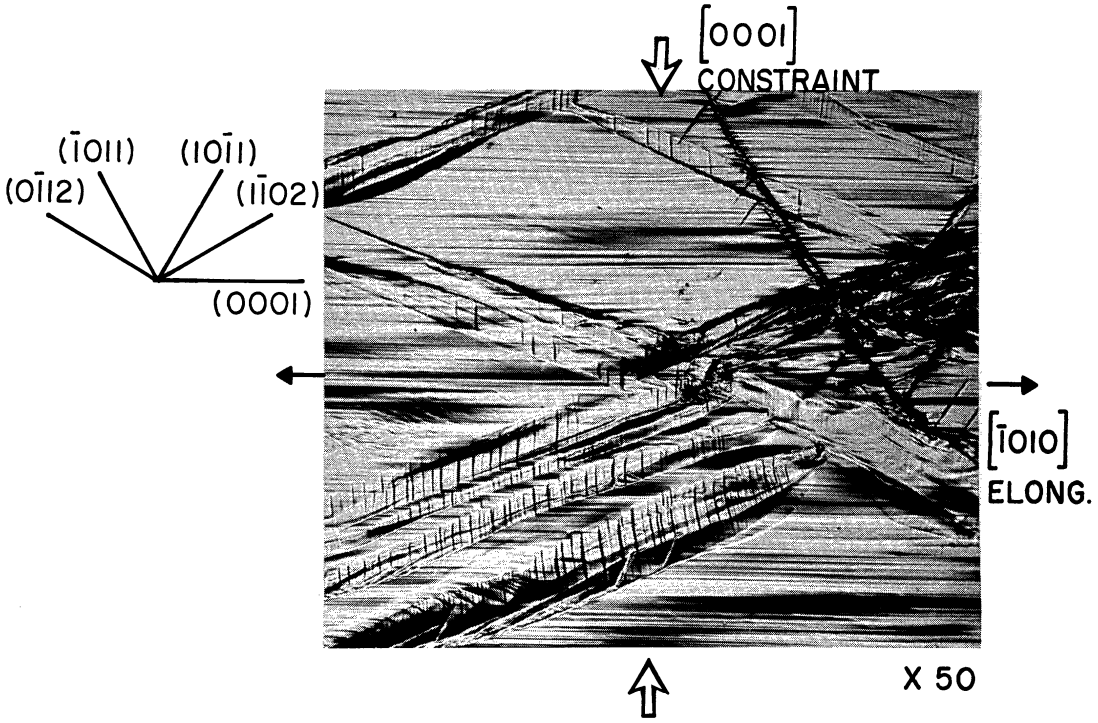

Fig. 8. (1$\bar{2}$10) compression surface of a D-oriented pure magnesium single crystal showing {10$\bar{1}$1} bands, horizontal basal slip, and basal slip in {10$\bar{1}$2} twins. Polished surface protected by teflon during deformation.

along $\{10\bar{1}1\}$ bands after perhaps 10% strain and cracking became more widespread with additional strain. In some specimens fractures occurred rather abruptly on surfaces parallel to $\{10\bar{1}1\}$. A typical C-oriented specimen that fractured in this manner is shown in Fig. 3. Cracking was not as prevalent in the D orientation as in the C, but where it did occur it generally followed a $\{10\bar{1}1\}$ trace. More often $\{10\bar{1}2\}$ twinning, $\{10\bar{1}1\}$ banding, basal slip within $\{10\bar{1}2\}$ twins, lattice rotations and kinking so disrupted the structure after some 15% strain that the specimens lost much of their single crystal character and the crystallographic orientation of fractures could not be determined.

Basal slip: Orientation G is favorable for (0001) $\langle 1\bar{2}10\rangle$ easy basal glide; that is, the single crystal is so aligned that all of the plastic strain can be accommodated by a single active basal slip system. Furthermore, in orientation G the basal pole lies $\sim 45^{\circ}$ from the loading direction, minimizing the load necessary to initiate basal slip. Fig. 4 gives the stress-strain results for basal slip as obtained by plane-strain compression of G-oriented crystals. The critical resolved shear stress in pure magnesium was measured to be approximately 140 psi. That this is twice the value generally reported for basal slip in pure magnesium is understandable because in the plane-strain compression test a slight misalignment of the crystal with respect to the constraint direction creates additional resistance to basal slip. Furthermore, measurements are

affected by friction within the experimental apparatus and this is difficult to correct for at the low stresses involved. Despite this the results of the compression of G-oriented specimens provided an order-of-magnitude check upon the operation of the plane-strain compression apparatus and also clearly demonstrated the extreme crystallographic anisotropy to plastic deformation that exists in magnesium.

$\{10\bar{1}1\}$ Twinning: $\{10\bar{1}1\}$ twinning is the initial and key step to $\{10\bar{1}1\}$ banding, and the activation stress for the twinning mode is also the stress to initiate $\{10\bar{1}1\}$ banding. Other investigators (8,16) have concluded that a simple critical resolved shear stress law does not exist for $\{10\bar{1}1\}$ twinning. It has been postulated by these investigators that stress concentrations produced by the intersection of various non-basal slip systems may be necessary for the activation of this twinning mode. The results obtained in this work tend to support this concept in that those orientations most favorable for non-basal slip exhibited the lowest shear stress to activate $\{10\bar{1}1\}$ banding. Thus, the C and D orientations, most favorable for non-basal slip, had resolved shear stresses of only ~7 ksi when banding was activated, whereas orientations A, B and $\{10\bar{1}2\}$-twinned-E, in which it is theoretically impossible to generate the non-basal systems of $\{10\bar{1}0\}\langle 1\bar{2}10\rangle$ prism or $\{10\bar{1}1\}\langle 1\bar{2}10\rangle$ pyramidal slip, had high shear stresses (~19 ksi) when $\{10\bar{1}1\}$ banding was initiated.

Reed-Hill and Robertson (17) reported minute amounts of $\{11\bar{2}2\}$ slip out of the basal plane at -190°C and this mode could be a factor in the initiation of banding in orientations A, B and E. Orientation F, reoriented by $\{10\bar{1}2\}$ twinning, is only moderately favorable for non-basal slip and exhibited a resolved shear stress of ~10 ksi at the time that $\{10\bar{1}1\}$ banding was activated.

$\{10\bar{1}1\}$ banding is a combined system of deformation consisting of $\{10\bar{1}1\}$ twinning followed immediately by $\{10\bar{1}2\}$ retwinning at a reduced activation shear stress, with this being followed by basal slip in the retwinned band at a still lower critical resolved shear stress. Thus, once a small volume of material has undergone $\{10\bar{1}1\}$ twinning as a result of a compressive stress, an extended strain within the twin should occur, and the stress required to continue strain in a band should be considerably less than that to initiate the band. The stress-strain curve would therefore be expected to have a marked yield point at the initiation of $\{10\bar{1}1\}$ twinning. Yield points were not observed, however, (see Figs. 2, 4 and 5) and this might be explained by the extremely small volume of material in a $\{10\bar{1}1\}$ twin as compared to the total volume of the specimen. High stresses in very localized regions of the crystal could be generated owing to surface asperities or to the interaction of various deformation systems. These stresses, high enough to activate local $\{10\bar{1}1\}$ twinning, would be virtually impossible to measure because of their extremely localized

nature, and the apparent stress measured over the entire crystal would be significantly less than the activation stress. Since the stresses to actuate $\{10\bar{1}2\}$ retwinning and subsequent basal slip in a band must be much less than those for the initial $\{10\bar{1}1\}$ twinning, and because a yield point is not observed, it is reasoned that the stress indicated by the stress-strain curve at the beginning of $\{10\bar{1}1\}$ banding more nearly represents the stress to continue rather than to activate the banding. This leads to the conclusion that the stress to initiate $\{10\bar{1}1\}$ twinning would be very difficult to isolate and measure.

Alloy single crystal deformation

The results of plane-strain compression testing of single crystals of the two magnesium alloys, Mg-.5%Th and Mg-4%Li, are compared with the pure magnesium results in Figs. 9 through 14. Each figure presents a comparison of the two alloys with pure magnesium for a particular orientation.

Magnesium plus .5% thorium: Single crystals of the .5 wt% thorium alloy exhibited initial strain hardening rates in orientations A, B, C and D roughly 70% greater than those encountered in pure magnesium crystals of the same orientations. As indicated earlier the initial shape of the stress-strain curve in these orientations is attributable to strain hardening of basal slip systems that were activated despite efforts to suppress this mode. Sheely et al. (18) has shown that thorium in magnesium greatly

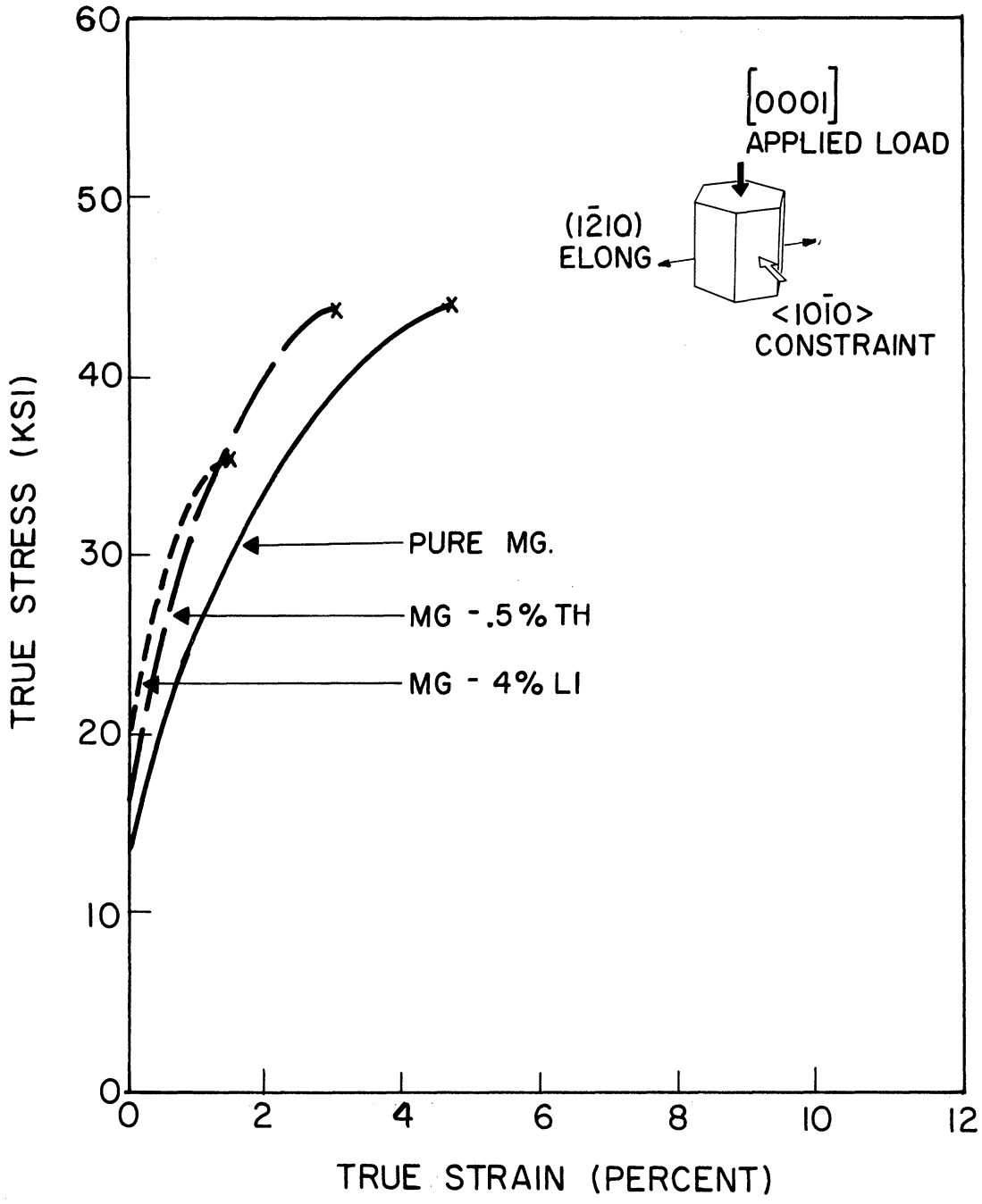

Fig. 9. Stress vs. Strain in A-oriented Single Crystals of magnesium and magnesium alloys.

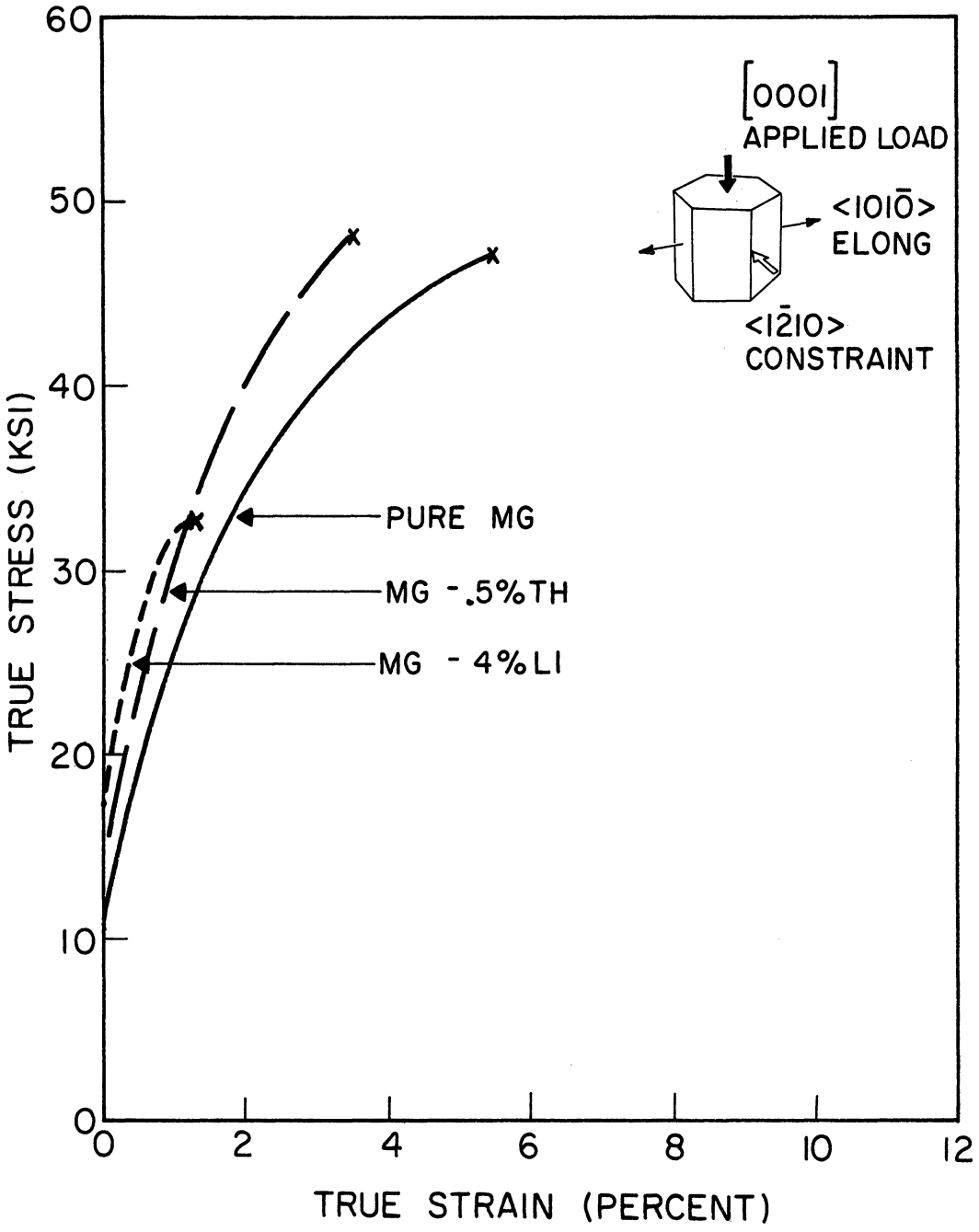

Fig. 10. Stress vs. Strain in B-oriented Single Crystals of magnesium and magnesium alloys.

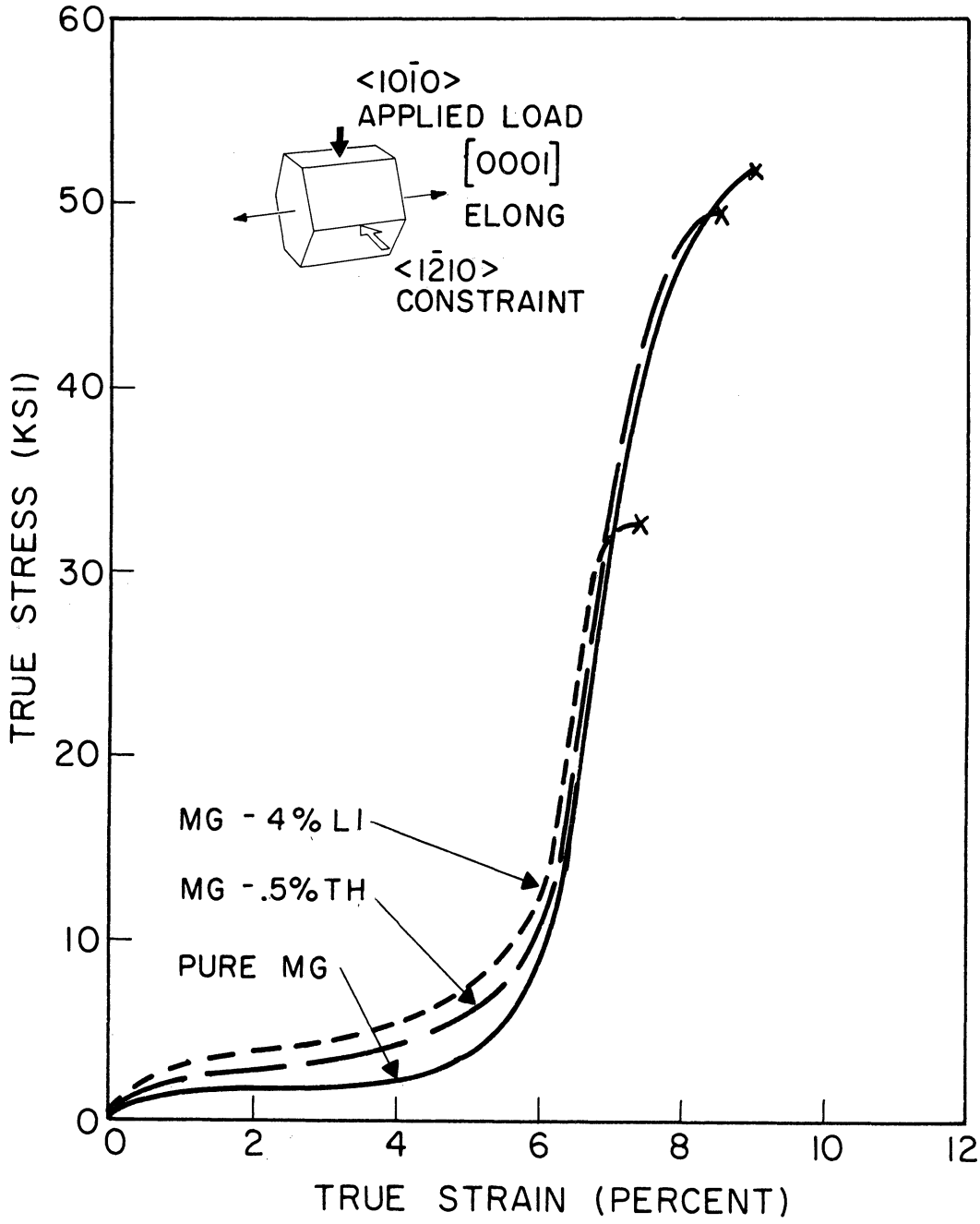

Fig. 11. Stress vs. Strain in E-oriented Single Crystals of magnesium and magnesium alloys.

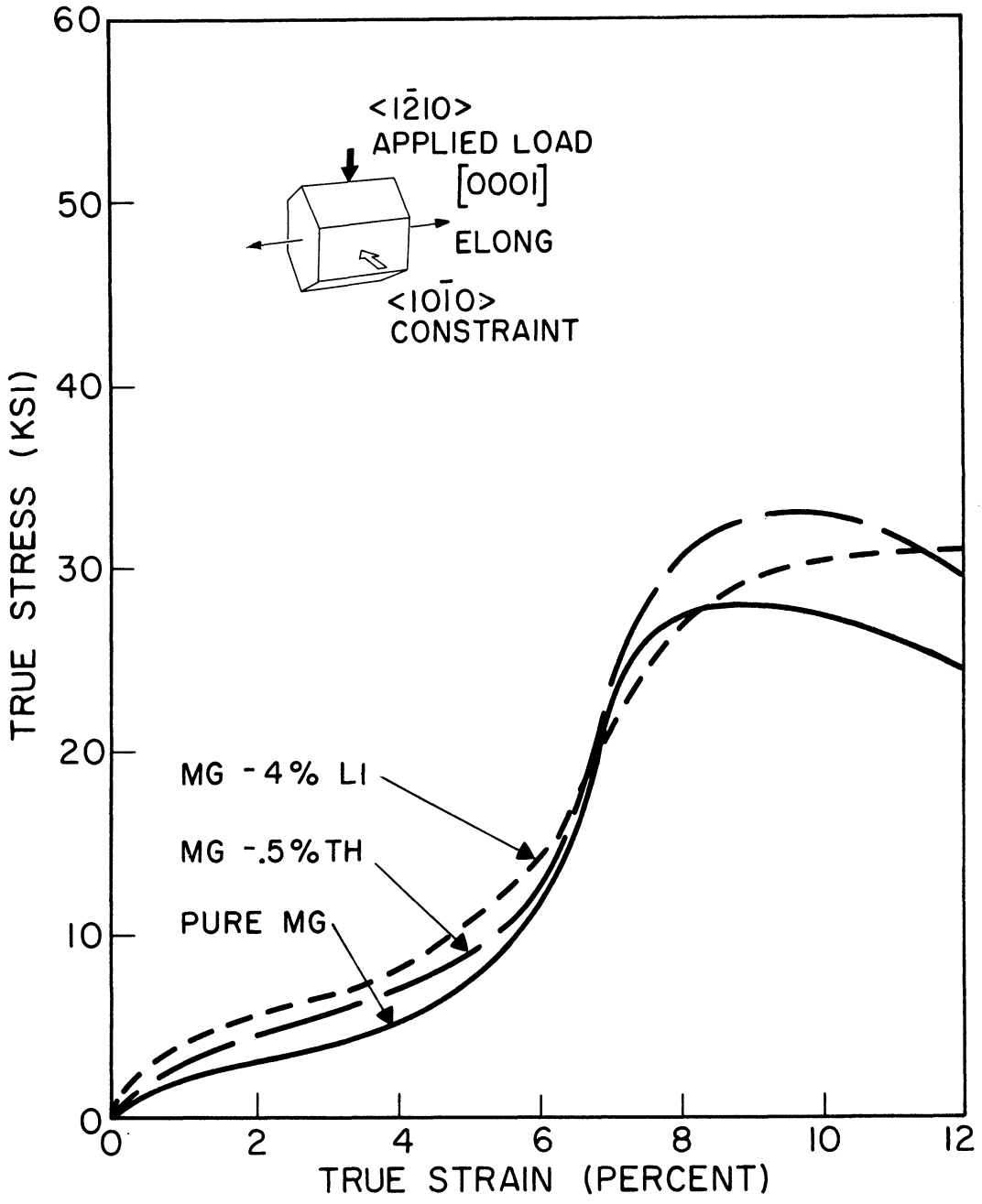

Fig. 12. Stress vs. Strain in F-oriented Single Crystals of magnesium and magnesium alloys.

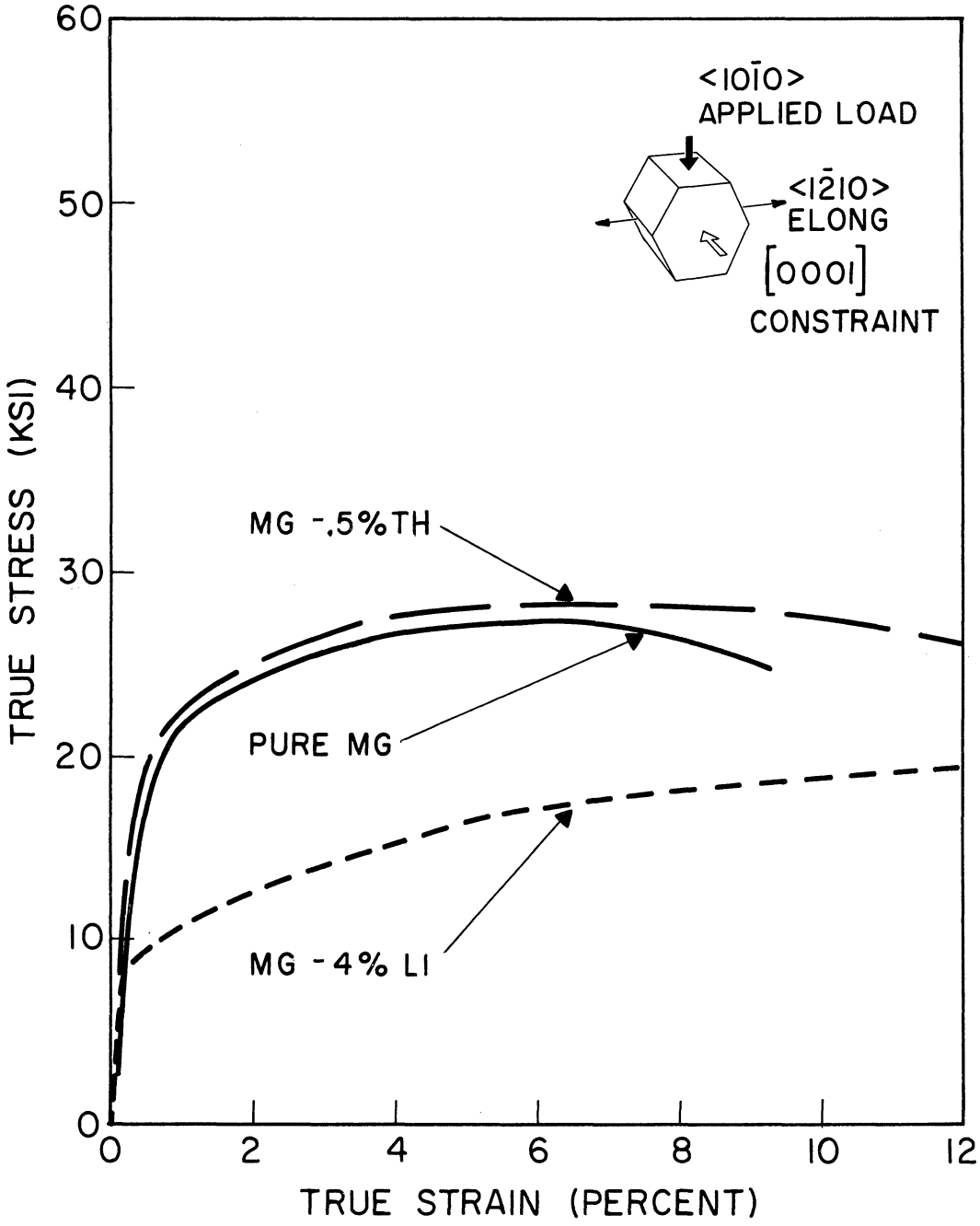

Fig. 13. Stress vs. Strain in C-oriented Single Crystals of magnesium and magnesium alloys.

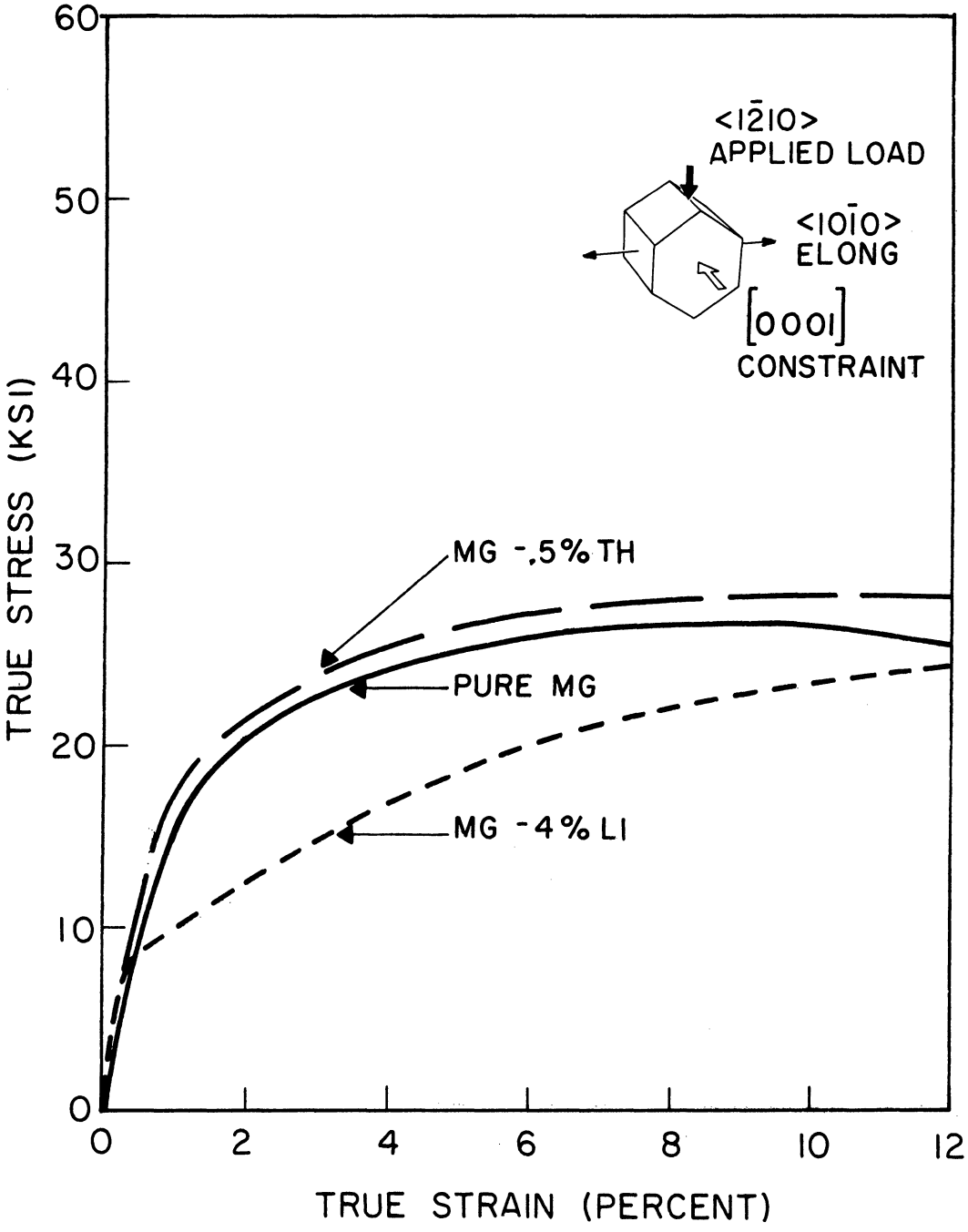

Fig. 14. Stress vs. Strain in D-oriented Single Crystals of magnesium and magnesium alloys.

increases the rate of strain hardening of the basal slip systems, which would account for the steeper stress-strain curves in the alloy crystals.

In orientations E and F a hardening against $\{10\bar{1}2\}$ twinning was encountered as is evident in Figs. 11 and 12. This too was considered to be a manifestation of the solution strengthening of the thorium, although the substructure present in the alloy single crystals may have contributed to the effect.

All other deformation characteristics of the Mg-.5%Th alloy single crystals were essentially the same as those of pure magnesium crystals. The fracture strengths and the modes of fracture were identical for the two materials and $\{10\bar{1}1\}$ banding was activated in the alloy in an equivalent manner and under loading stresses similar to those encountered in pure magnesium.

Magnesium plus 4% lithium: Like the thorium alloy crystals, single crystals of the 4 wt% lithium alloy of magnesium exhibited initial strain hardening rates some 70 to 80% greater than those of pure magnesium crystals. This strengthening effect was also attributed to the solution strengthening of the alloying element on the basal slip and $\{10\bar{1}2\}$ twinning systems. The somewhat greater hardening effect evident in the lithium alloy crystals is credited to the much greater fraction of solute element in the magnesium-lithium alloy (12 at% lithium vs. .05 at% thorium).

In orientations C and D the magnesium-lithium crystals deformed by $\{10\bar{1}0\}\langle 1\bar{2}10\rangle$ prism slip, a mode not observed in either the pure magnesium or in Mg-.5%Th. However this mode was not unexpected as it had been previously reported (19,20) for α solid solution alloys of lithium in magnesium at room temperature. The typical prism slip lines that appeared on the surfaces of a deformed Mg-4%Li crystal of C orientation are shown in Fig. 15. The room-temperature critical resolved shear stress for this mode was found to be about 3.5 ksi, which compares favorably with the results of Yoshinaga and Horiuchi (20).

Crystals of the D orientation strain hardened at a much faster rate than those of the C orientation. This is explained by the lattice rotation produced by the prism slip. Lattice rotation incident to slip deformation in compression reduces ϕ, the angle between the normal to the slip plane and the loading direction. At the same time λ, the angle between the slip direction and the loading direction, is increased toward a maximum of 90°. For prism slip in the D orientation ϕ is initially 30° and λ is 60° (see Fig. 16a). Lattice rotation caused by prism slip on system 3 of Fig. 16a tends to reduce ϕ_3 and increase λ_3 thus "hardening" that system. However, lattice rotation due to slip on system 3 rotates system 3' to a more favorable crystallographic orientation and slip should then operate on system 3' causing an opposite rotation. As deformation continues the two systems should operate

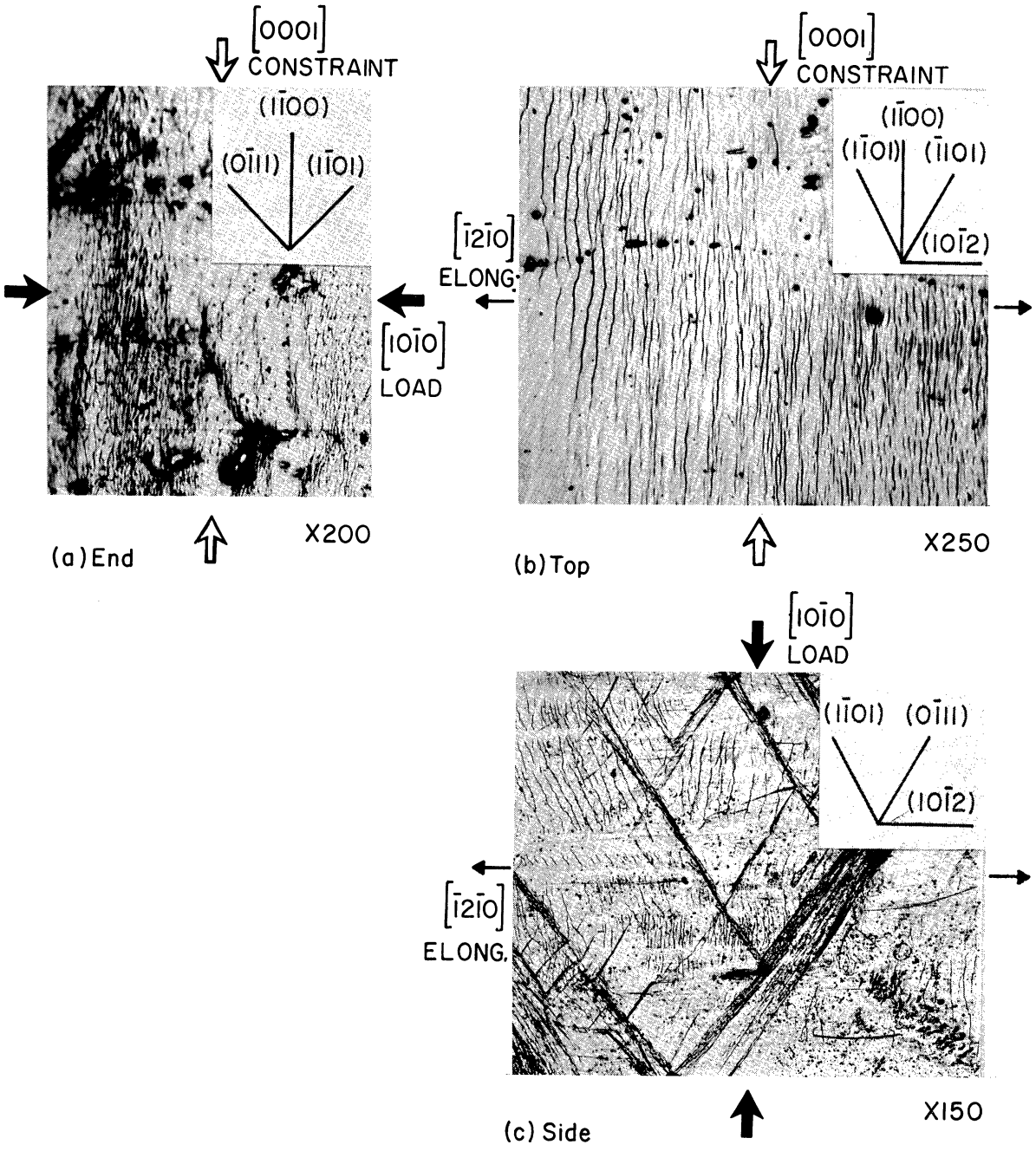

Fig. 15. $\{10\bar{1}0\}\langle\bar{1}2\bar{1}0\rangle$ Prism Slip in a C-oriented Single Crystal of Mg-4%Li. (a) $(\bar{1}2\bar{1}0)$ unconstrained surface, (b) $(10\bar{1}0)$ compression surface showing prism slip. (c) $(000\bar{1})$ constrained surface. Prism slip in material that has twinned by $\{10\bar{1}2\}$ is shown plus $\{10\bar{1}1\}$ bands. Polished surface protected by teflon during deformation.

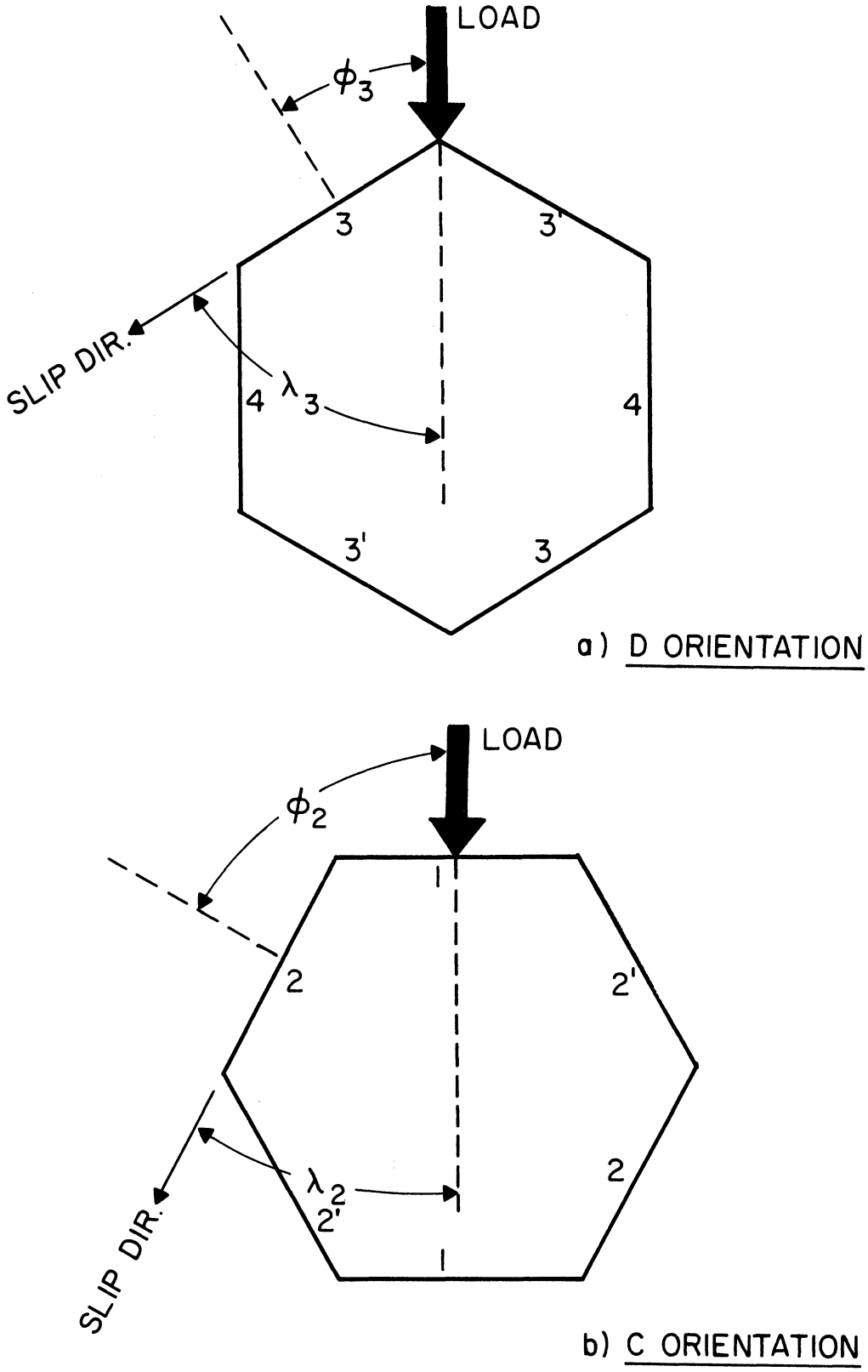

Fig. 16. $\{10\bar{1}0\}$ $\langle\bar{1}2\bar{1}0\rangle$ Prism Slip Systems in Magnesium. (a) D orientation: Systems 3 and 3' active, System 4 inactive. (b) C orientation: Systems 2 or 2' active, System 1 initially inactive but active after lattice rotation of 30°.

together. For this reason orientation D is stable with regard to lattice rotation and deformation will proceed with no net rotation.

On the other hand orientation C is unstable (see Fig. 16b). Initially prism slip on either system 2 or 2' is equally likely, but once one system operates more than the other, it becomes the favored system. If, for example, slightly more slip were to occur on system 2, the lattice would then rotate so as to reduce ϕ_2 and to increase λ_2 toward values of 45°, the orientation of easiest slip. Slip on system 2 would become more favorable, while the same rotation would make system 2' less favorable for slip. System 2 should therefore continue to operate. Because of this, orientation C is unstable with regard to lattice rotation under prism slip and once the slip has begun on a particular system it will continue on the same system. The lattice will be rotated toward the 45° orientation of easiest slip and on through this optimum toward the stable D orientation. Thus the C orientation can be expected to undergo as much as 30° of lattice rotation. During the first 15° of this, a crystallographic "work softening" will be produced which tempers the basic strain hardening of the slip system.

X-rays of deformed crystals have confirmed the stability of the D orientation and the tendency of the C orientation to rotate toward the D orientation during prism slip. The "softening" due to rotation in the C orientation

accounts for the difference between the strain hardening rates of the Mg-4%Li stress-strain curves of Figs. 13 and 14.

Although crystals of D orientation strain hardened faster during prism slip than those of C, specimens of both orientations hardened at a sufficiently rapid rate so that after some initial deformation the stress necessary to produce additional strain had increased to a value great enough to activate $\{10\bar{1}1\}$ banding, preceded as before by $\{10\bar{1}2\}$ twinning. Fig. 15 shows the three surfaces of a C-oriented specimen in which this has occurred. Both $\{10\bar{1}1\}$ bands and prism slip markings (within $\{10\bar{1}2\}$ twins in this instance) are readily identified in the (0001) surface.

Single crystals of the Mg-4%Li alloy under plane-strain compression along the c-axis exhibited fracture stresses roughly 25% lower than those of either pure magnesium or Mg-.5%Th crystals. These results are indicated in Figs. 9, 10 and 11. Furthermore, fracture occurred along $\{10\bar{1}1\}$ planes instead of along $\{11\bar{2}4\}$ planes as observed in both pure magnesium and Mg-.5%Th crystals of similar orientations. Apparently the 4% lithium in magnesium reduces the stress necessary for failure along $\{10\bar{1}1\}$ planes to a value well below that required to initiate fracture along $\{11\bar{2}4\}$.

The fracture stress of specimens of orientation A in

the Mg-4%Li alloy was about 5% greater than in B-oriented specimens. This is consistent with the fact that lateral constraint would offer a resistance to shear on active $\{10\bar{1}1\}$ planes in orientation A but not in orientation B.

Deformation of textured polycrystalline magnesium

Two major factors are responsible for the stress-strain characteristics of textured polycrystalline materials. These are the single crystal deformation characteristics of the material and the crystallographic texture of the polycrystalline aggregate.

The single crystal deformation studies have demonstrated that the individual grains within a magnesium polycrystalline aggregate must deform by basal slip, prism slip (in the lithium alloy), $\{10\bar{1}2\}$ twinning, $\{10\bar{1}1\}$ banding or combinations of these. Because the critical resolved shear stress for basal slip is very low compared to the activation stresses for other plastic deformation modes in magnesium, basal slip accounts for much of the deformation in the polycrystalline aggregate. However, since there are only three basal slip systems (and only two of these are independent) in a single grain of magnesium, and because five independent deformation modes are required for an arbitrary shape change in any material (7), it is reasonable that modes other than basal slip must account for some of the deformation.

Texture plays an extremely significant role in the

deformation of polycrystalline magnesium because of the orientation dependence of strength in the individual grains. If the texture is very strong the polycrystalline material can be expected to exhibit deformation characteristics quite similar to those of single crystals of the same composition. If the polycrystalline material has a weak texture its deformation characteristics should not differ markedly from those of a randomly oriented polycrystalline aggregate.

To assist in the identification of, and reference to, the polycrystalline specimens, each of the six orientations has been assigned a two letter identifying code. These are combinations of the letters Z (thickness direction), R (rolling direction) and T (transverse direction) with the first letter signifying the loading direction and the second letter the extension direction. Thus ZR specimens were compressed in the thickness direction while extension was permitted to operate in the rolling direction of the textured material. Polycrystalline specimens ZR and ZT have textures which resemble the orientations of single crystal specimens A and B, while TR and RT are most nearly like specimens C and D, and TZ and RZ resemble E and F.

Textured polycrystalline pure magnesium: The texture of the polycrystalline pure magnesium under investigation was found to be that represented by the pole figure in Fig. 17. This is a strong texture with the basal pole aligned predominantly in the thickness direction, and with considerably more rotation of the basal pole about the

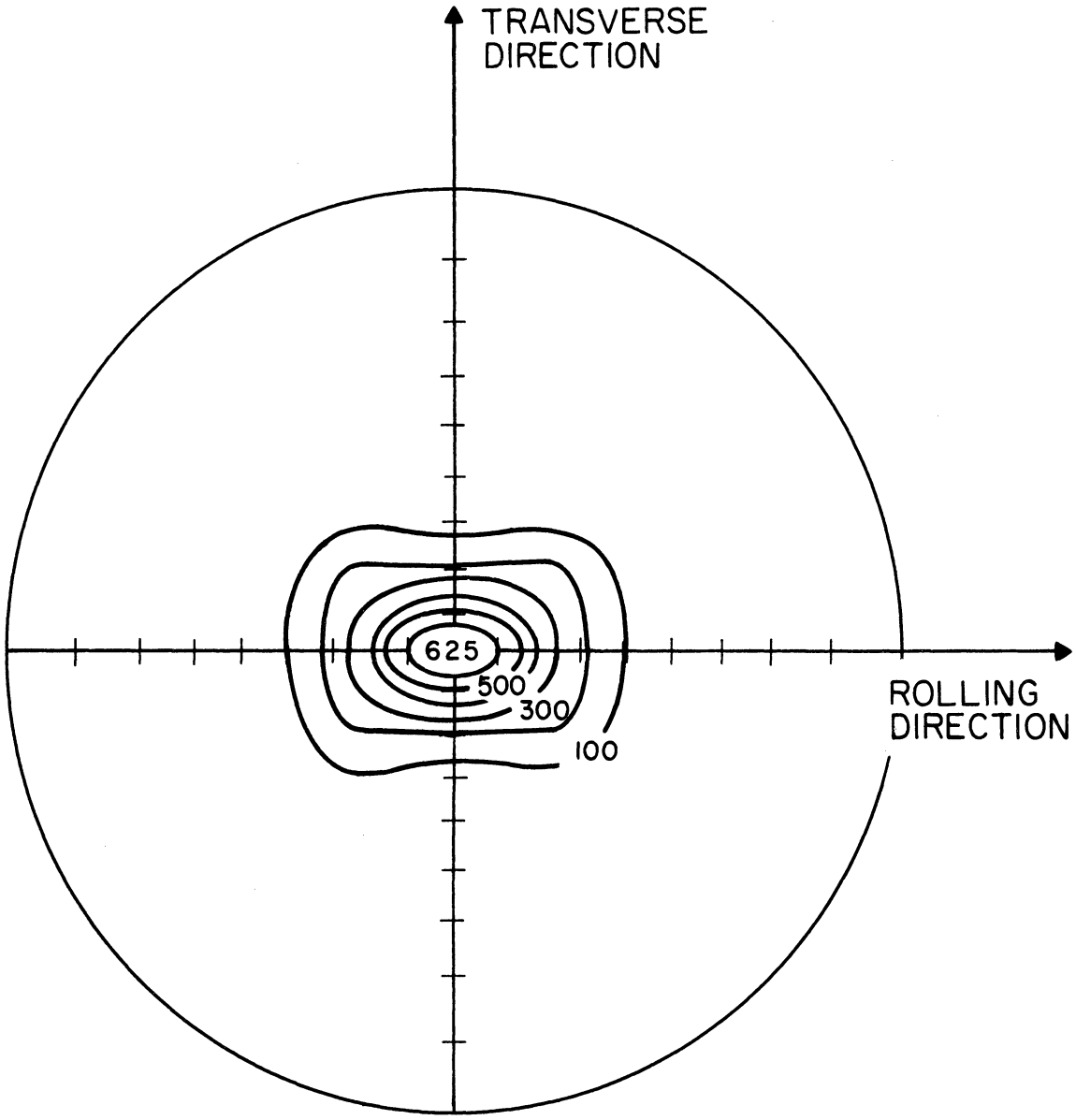

Fig. 17. [0001] Pole Figure for Textured Pure Magnesium.

transverse direction than about the rolling direction.

The stress-strain results of plane-strain compression of the textured pure magnesium specimens are presented in Fig. 18. The single crystal curves for pure magnesium are also presented for comparison. The similarity of the results of textured polycrystals and single crystals is apparent. The differences that do exist are attributable to the fact that the texture does not completely match a single crystal orientation.

Orientation ZT (compression in the thickness direction and constraint along the rolling direction) most nearly approximates single crystal orientations A and B (compression along the c-axis), differing only in that the misalignment of many of the grains of the polycrystalline specimen allows a significant amount of basal slip. This difference leads to a greatly reduced maximum stress in the polycrystalline specimens. Nevertheless, orientation ZT was found to require the largest stress to bring about a given amount of initial strain of any of the polycrystalline orientations. This is consistent with the resemblance of the ZT orientation to orientations A and B which are the strongest of the single crystal orientations.

Orientation ZR (compression also in the thickness direction but with constraint along the transverse direction) is considerably softer than orientation ZT. This is because the basal pole is more widely distributed about the

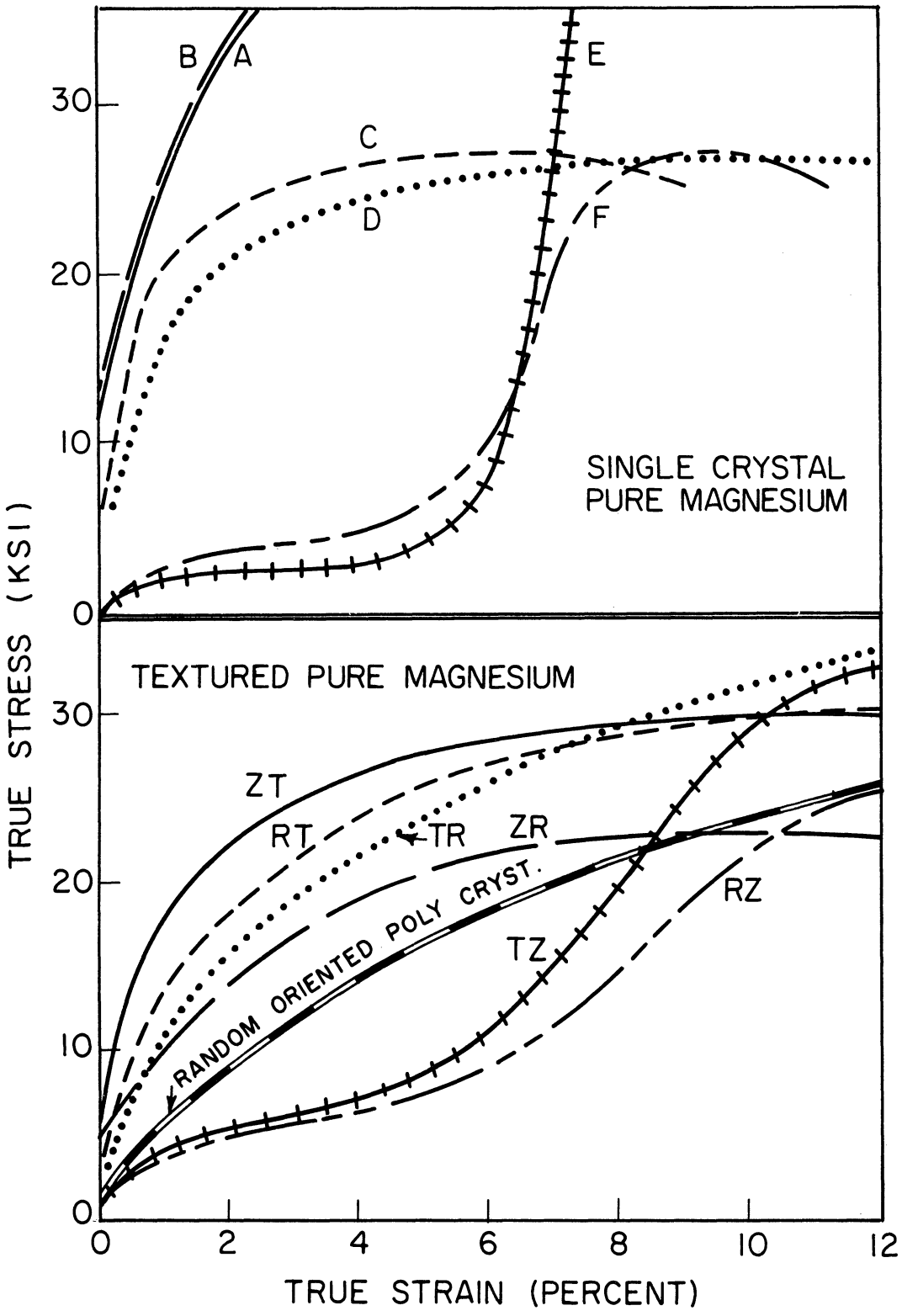

Fig. 18. Stress vs. Strain in Pure Magnesium. Top: For each of the single crystalline plane-strain orientations A, B, C, D, E, and F. Bottom: For each of the textured polycrystalline plane-strain orientations ZT, RT, ZR, TZ, TR and RZ, and for randomly oriented polycrystalline material.

transverse direction and basal slip in the ZR-oriented specimens is therefore favorable in a greater percent of the grains.

Orientations RT and TR bear a similarity to single crystal orientations C and D although, like the other polycrystalline orientations, they too contain many grains which are favorably oriented for basal slip. Since basal slip was favorable in some of the grains, the RT and TR polycrystalline specimens were deformed during the early stages of loading more easily than were the single crystals. In both the RT and TR textured specimens the deformation produced by the $\{10\bar{1}1\}$ banding and band widening was augmented in numerous grains by basal slip and/or $\{10\bar{1}2\}$ twinning where the orientations were favorable for these modes. Due to the activation of different modes in the various grains of the polycrystalline specimens the texture became more and more random as deformation progressed. The relatively widespread operation of a single mode, such as the $\{10\bar{1}1\}$ band widening in single crystal orientation C, was not possible and the stress to continue deformation increased steadily with strain. At approximately 6% strain the stress in the polycrystalline specimens rose above the maximum values observed for single crystal orientation C and D. Values as high as 35 ksi were attained in polycrystalline orientation TR, some 20% higher than the maximum values observed in the single crystals.

Orientations TZ and RZ of the textured pure magnesium

exhibited extensive $\{10\bar{1}2\}$ twinning during the first 5 to 7% strain. After this initial deformation the stress-strain curves rose more steeply as the twinning approached completion and other deformation modes were required. In these specimens the crystallographic texture resembled single crystal orientations E and F (c-axis unconstrained). The fact that the polycrystalline strengths during $\{10\bar{1}2\}$ twinning were much greater than those of the single crystal orientations is attributable to two factors. First, the polycrystalline specimens were not able, because of the diversity of the grain orientations, to accommodate all of the strain by $\{10\bar{1}2\}$ twinning as was possible in the single crystals. Instead, other modes were forced to participate in some of the grains, requiring a higher stress. In addition, the polycrystalline material was more resistant to $\{10\bar{1}2\}$ twinning owing to a grain-size effect. In a single crystal, once a $\{10\bar{1}2\}$ twin system is activated, strain can be extended relatively easily by the operation of the twinning system through the full dimension of the specimen. In a polycrystal, however, a system can operate only within the small volume of a grain, and other systems must be activated in other grains to extend the strain. This causes a hardening that varies with grain size, and this is credited in this instance for much of the difference between the polycrystalline and single crystal results.

Randomly oriented specimen results are also presented in Fig. 18 by a curve for specimens of cast cell magnesium

(99.96% Mg). Since three orthogonal specimen orientations of the cell magnesium were tested and found to be very similar, it was concluded that the material was essentially random in orientation. As might be expected, the curve for these randomly oriented specimens is a rather general average of the curves for the textured materials.

Textured polycrystalline Mg-.5%Th: The single crystal deformation results showed that the solution hardening of magnesium by .5 wt% thorium is very significant for both basal slip and $\{10\bar{1}2\}$ twinning. The differences between deformation characteristics of polycrystalline specimens of the Mg-.5%Th alloy and those of pure magnesium are explained by this solution hardening as well as by the differences in the pole figures for the two materials (Figs. 19 and 17). The Mg-.5%Th alloy has a much weaker crystallographic texture than that of the pure magnesium, the peak intensity being about one-half as great. Furthermore, the pole figure is more nearly symmetrical about the thickness direction.

The stress-strain relationships found for the textured Mg-.5%Th specimens are presented in Fig. 20 together with those for single crystals of the same alloy. The effect of the texture symmetry about the thickness direction is readily apparent as orientations ZT_{Th} and ZR_{Th} produced almost identical stress-strain curves. In a like manner pairs of similar curves resulted from TR_{Th} and RT_{Th} and from TZ_{Th} and RZ_{Th}.

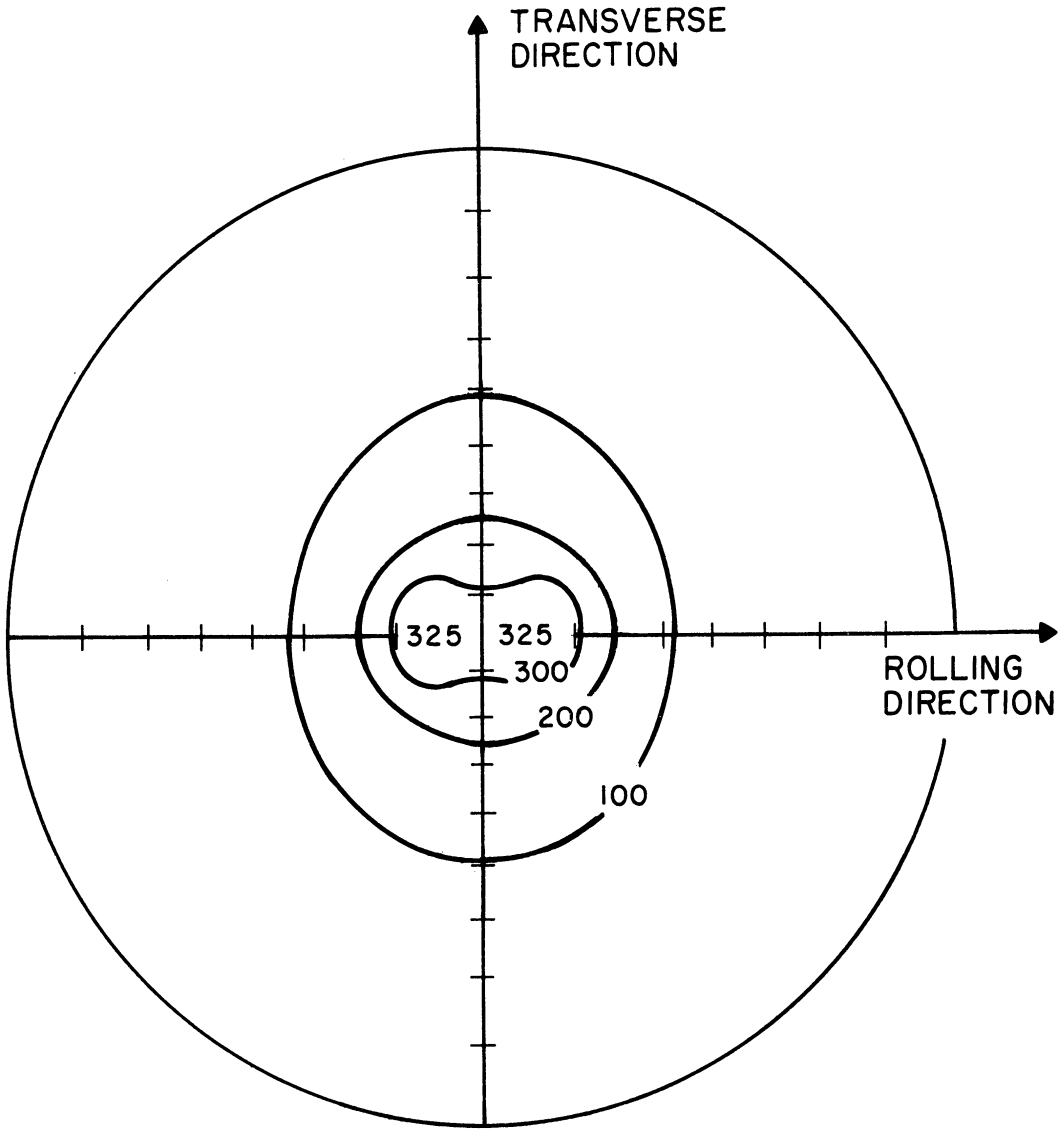

Fig. 19. [0001] Pole Figure for Textured Mg-.5%Th.

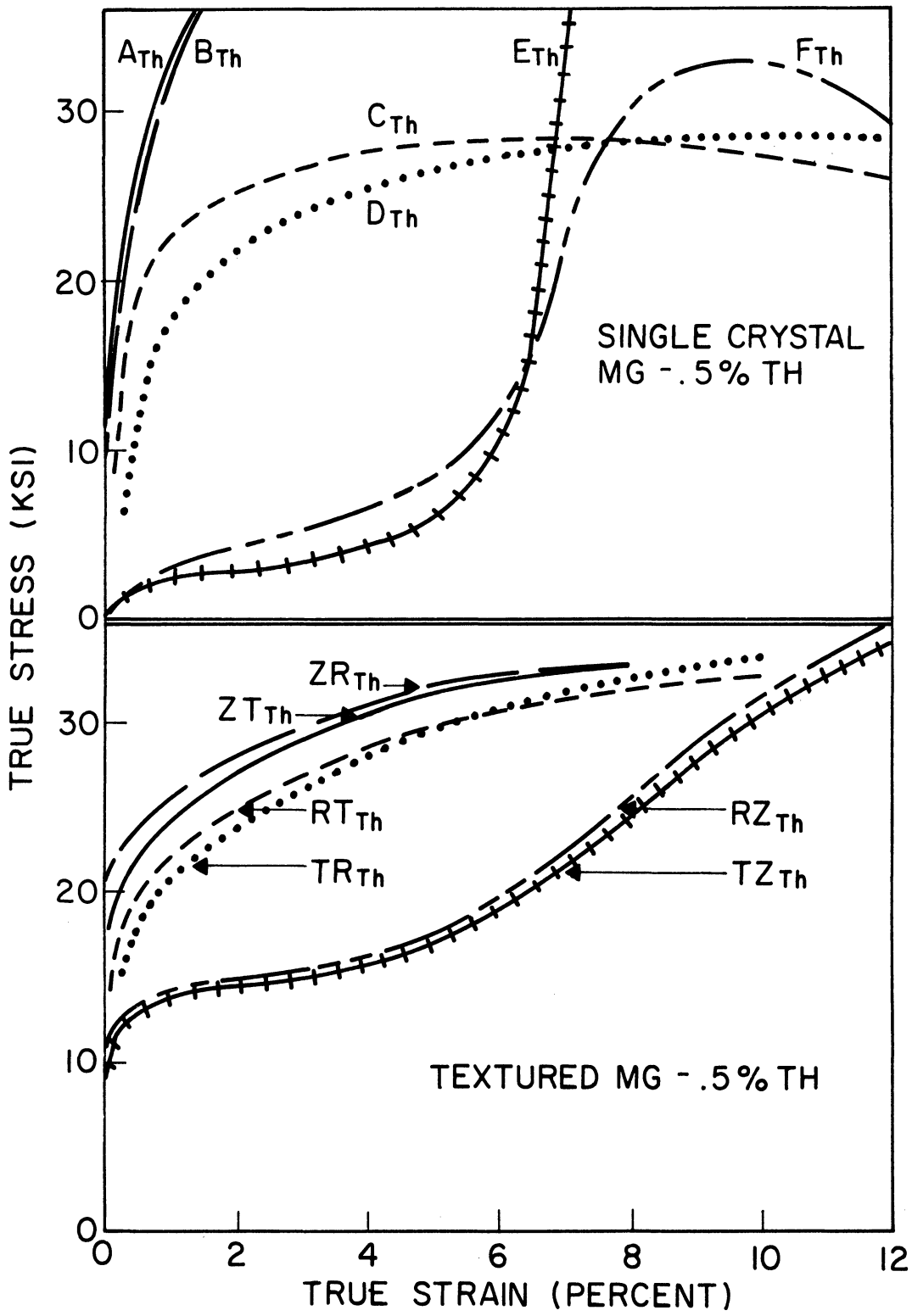

Fig. 20. Stress vs. Strain in Mg-.5%Th Alloy. Top: For each of the single crystalline plane-strain orientations A, B, C, D, E, and F. Bottom: For each of the textured polycrystalline plane-strain orientations ZT, RT, ZR, TZ, TR, and RZ.

The strengthening of the .5% thorium influenced the stress-strain relationships in all polycrystalline orientations in the form of a very steep rise in the stress to cause the first ~.2% strain. This is consistent with the high critical resolved shear stresses for basal slip and for $\{10\bar{1}2\}$ twinning in the alloy. The fact that the ZT_{Th} and ZR_{Th} specimens (compression in the thickness direction) were only 3 to 4 ksi stronger than the TR_{Th} and RT_{Th} specimens (compression perpendicular to the constrained thickness direction) is attributed to the relatively weaker texture of the alloy as compared to that for pure magnesium. The markedly greater activation stresses for $\{10\bar{1}2\}$ twinning in orientations RZ_{Th} and TZ_{Th} (compression perpendicular to the unconstrained thickness direction) were due to the hardening of the $\{10\bar{1}2\}$ twinning systems by the alloying element, to the diversity of grain orientations associated with the much less intense texture than that for the pure metal, and to the grain size effect that was described earlier.

Textured polycrystalline Mg-4%Li: The single crystal results demonstrated that the solution hardening of magnesium by 4 wt% lithium is slightly greater than that by .5 wt% thorium. The solution strengthening affects the deformation characteristics of the textured material in a similar manner. It accounts for the very steep initial portion of the stress-strain curves that are presented in Fig. 22.

The pole figure of the magnesium-lithium polycrystalline

material (Fig. 21) indicates a relatively weak texture with a peak intensity about one-third of that of the pure magnesium and less than that of the thorium alloy. The texture is almost symmetrical about the thickness direction with a slightly greater divergence about the rolling direction than about the transverse. The weakness of the texture explains the low strengths of the ZR_{Li} and the ZT_{Li} specimens (compression in the thickness direction) relative to pure magnesium and magnesium-thorium alloy specimens of similar orientations. The high activation stresses for $\{10\bar{1}2\}$ twinning in TZ_{Li} and RZ_{Li} specimens (compression perpendicular to the unconstrained thickness direction) is a consequence of the weak texture of the lithium alloy and the effect of the grain size.

The symmetry of the pole figure about the thickness direction accounts for the virtually identical behavior of the ZT_{Li} and ZR_{Li} specimens, of the TR_{Li} and RT_{Li} specimens, and of the TZ_{Li} and RZ_{Li} specimens. Specimens of TR_{Li} and RT_{Li} orientations (compression perpendicular to the thickness direction) exhibited strengths about 30% below those of the ZR_{Li} and ZT_{Li} orientations. This is in significant contrast to the behavior of the thorium alloy and is a direct result of the prism slip that is active in the lithium alloy.

Yield loci of textured materials

One of the more useful characteristics of crystallographically textured metals is the strengthening that can

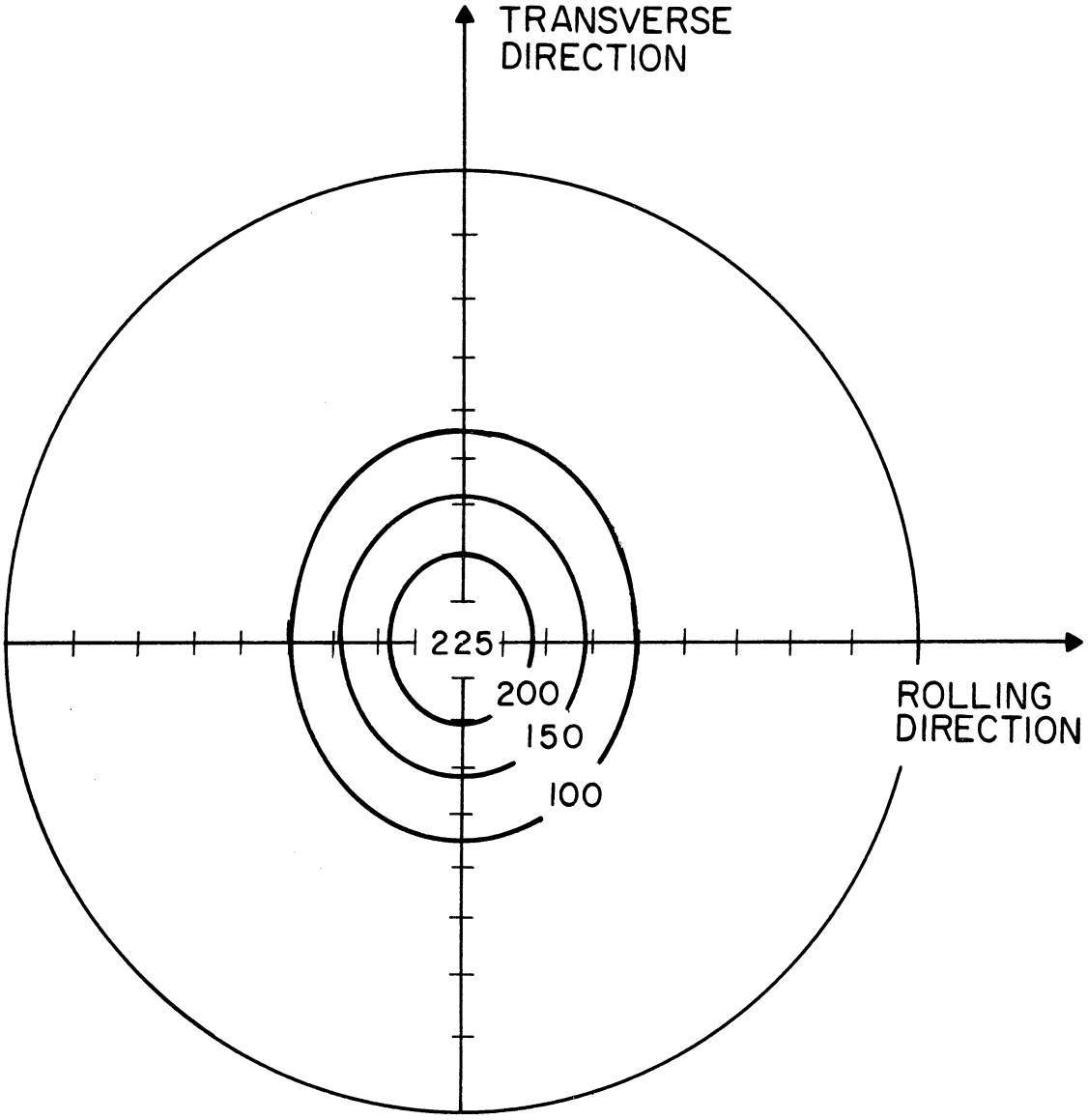

Fig. 21. [0001] Pole Figure for Textured Mg-4%Li.

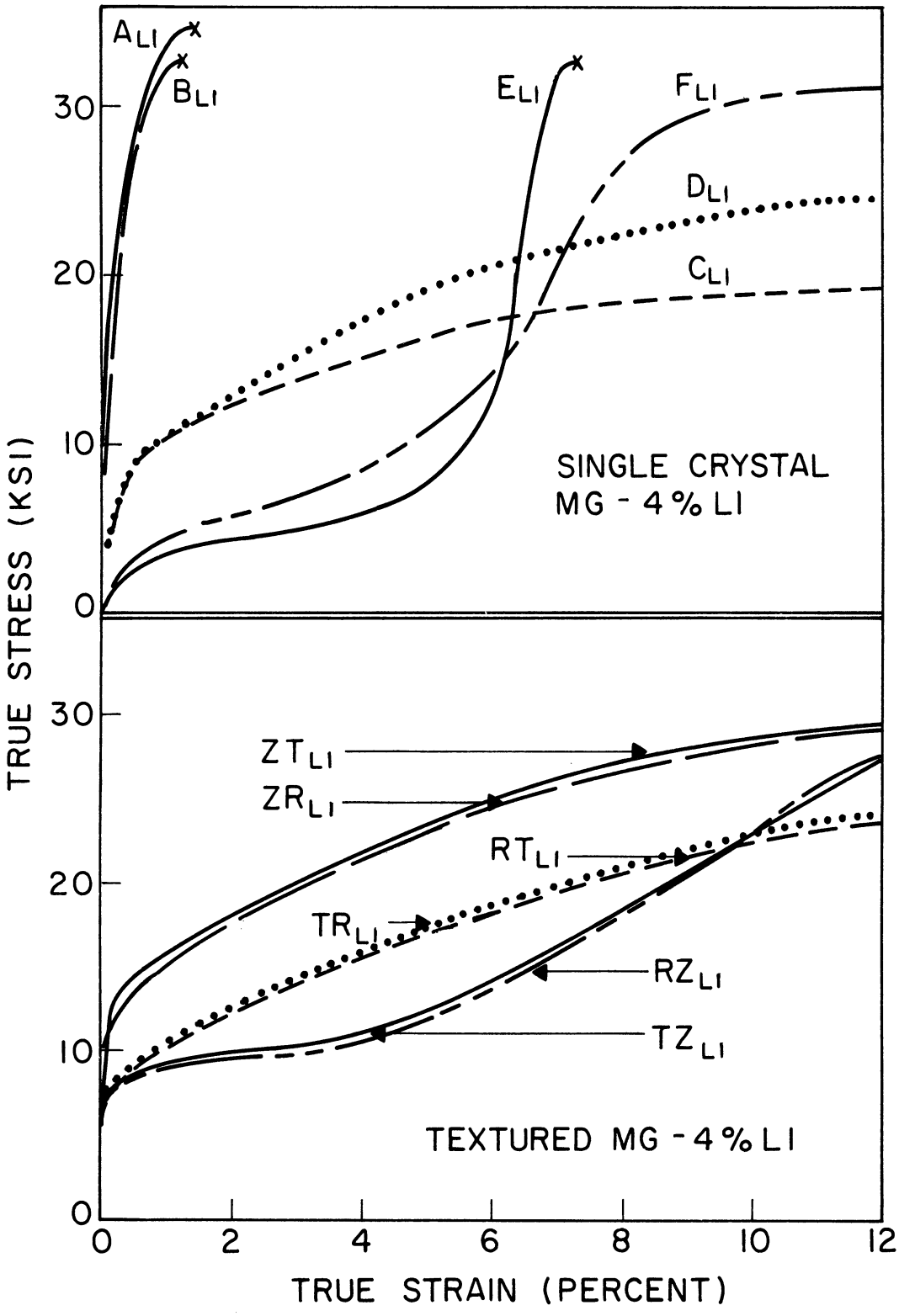

Fig. 22. Stress vs. Strain in Mg-4%Li Alloy. Top: For each of the single crystalline plane-strain orientations A, B, C, E, E, and F. Bottom: For each of the textured polycrystalline plane-strain orientations ZT, RT, ZR, TZ, TR, and RZ.

occur under combined stresses. Especially significant in this regard are the HCP metals with their inherent anisotropy as they often exhibit a pronounced increase in resistance to yielding under conditions of biaxial tension as compared to that under uniaxial loading.

Both Tresca and von Mises postulated criteria for yielding of isotropic materials under conditions of combined stresses. Hill (21) has generalized the von Mises criterion in formulating a yield criterion for anisotropic materials. The Hill criterion, however, predicts loci which are centered about the origin, a restriction which is unsatisfactory for materials such as the HCP metals which deform extensively by twinning (22). At present there is no simple mathematical yield criterion for such materials, and considerable experimental data is required to establish the yielding behavior for a given material of this type (23).

It is convenient to represent yield criteria graphically by assuming conditions of plane stress, i.e. the stress in one of the three orthogonal directions is taken to be zero. This representation of yield criteria is not severely restrictive since yielding is virtually insensitive to the level of hydrostatic stress, and any state of triaxial stress can therefore be represented by a hydrostatic stress plus a plane-stress state. The yield locus represents all of the various combinations of biaxial stress that will produce yielding.

In the experimental determination of a yield locus by mechanical testing, two types of data are useful; the values of the stresses at yielding serve to fix points on the locus, and measurements of the plastic strains accompanying yielding can be used to establish the slopes of the locus at these points. The significance of the plastic strain measurements follows from the principle of normality of the plastic strain vector to the yield locus (24), so that the slope of the plane-stress locus, $\tan\theta$ (i.e. $d\sigma_y/d\sigma_x$), equals $-d\epsilon_x/d\epsilon_y$.

Measuremements of the lateral strains as well as the yield stresses were made in two uniaxial tension and three uniaxial compression tests to fix five points on the locus (a, c, e, f and i in Fig. 23) and the slopes at these points. A sixth test, tension in the thickness direction, was considered impractical. The yield stresses observed in the plane-strain compression tests presented earlier were used to fix the stresses at which $\tan\theta = 0, \infty$, and 1 (lines d and h, b and g, and k and j in Fig. 23). The resulting yield loci, at 1% strain, are shown in Fig. 24 and the data used to construct them are listed in Table 3.

Pure magnesium yield locus: The yield locus for the textured pure magnesium (Fig. 24) is extremely interesting because of its highly non-symmetrical shape. Fundamentally, the non-symmetry consists of two distinct factors: the greater strength in tension than in compression, and the greater tensile strength in the transverse direction than

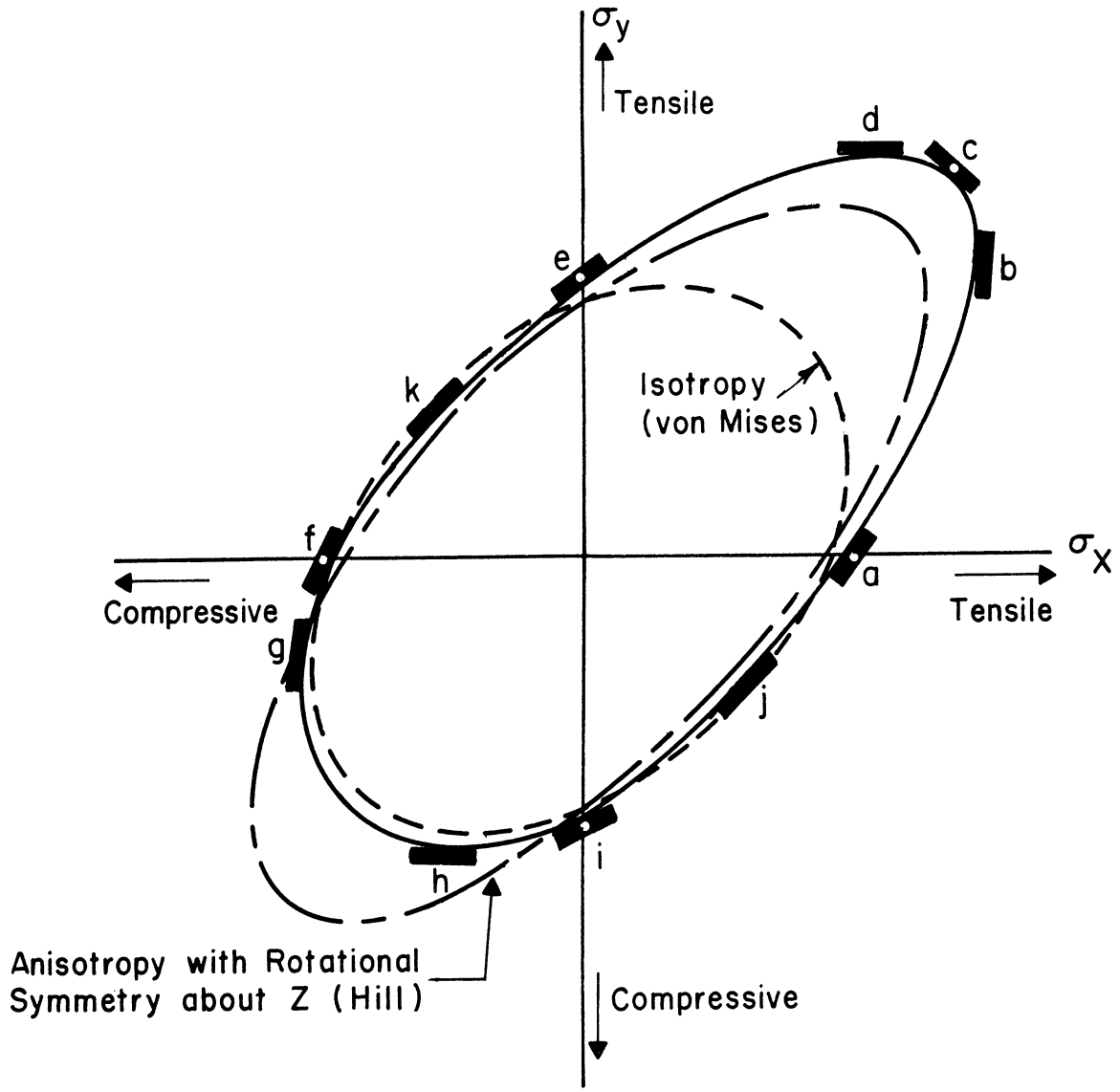

Fig. 23. Plane-stress ($\sigma_z = 0$) Yield Locus (schematic). Points and slopes are determined as follows: a and f, x-direction uniaxial tension and compression; e and i, y-direction uniaxial tension and compression; c, z-direction uniaxial compression; b and d, z-direction plane-strain compression; g and k, x-direction plane-strain compression; h and j, y-direction plane-strain compression. The loci predicted by von Mises and Hill criteria are shown for comparison. Adapted from Hosford.[23]

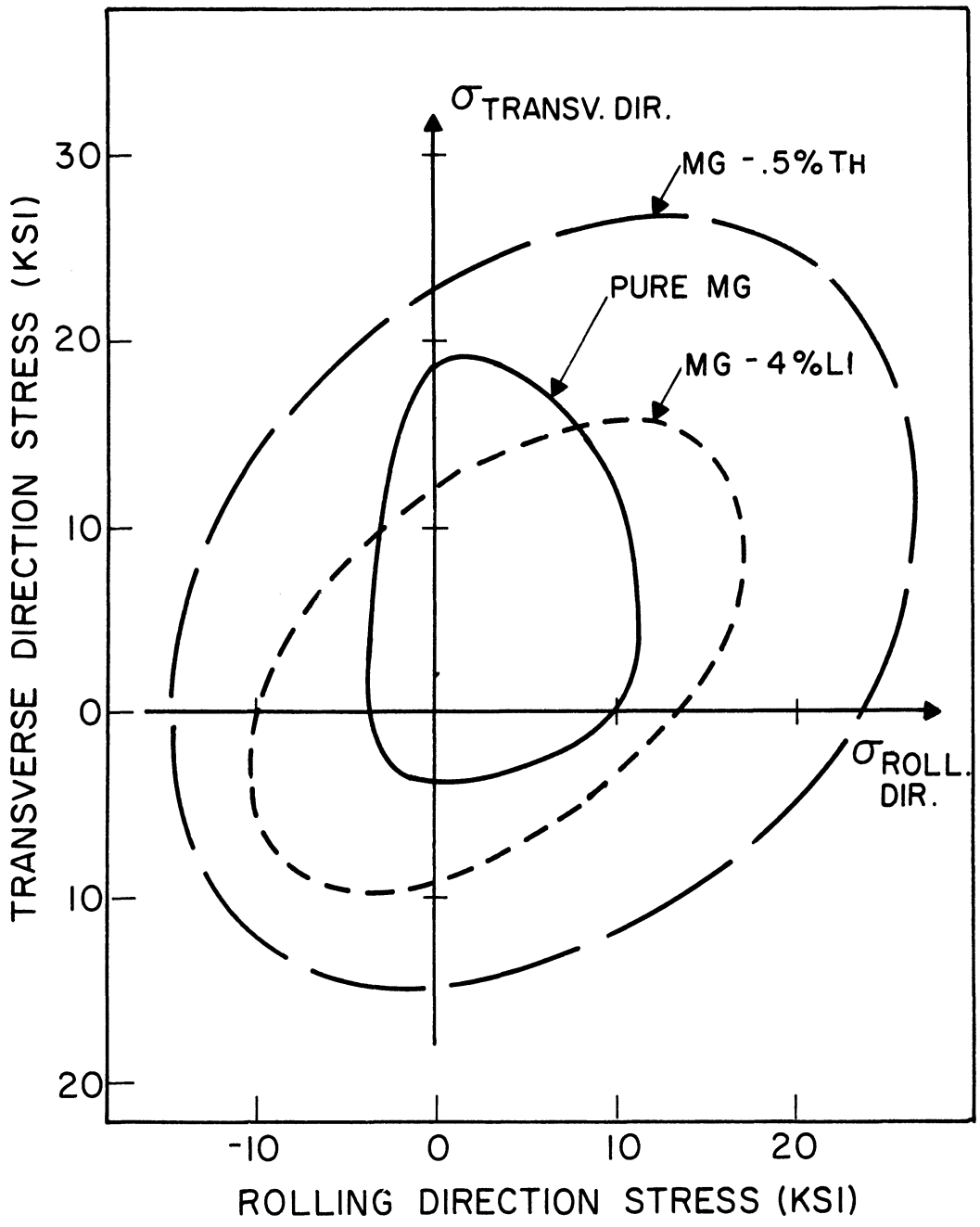

Fig. 24. 1% Strain Yield Loci for Biaxial Stresses in Textured Polycrystalline Magnesium and Magnesium Alloys with Thorium and with Lithium.

Table 3.

Experimentally Determined Yield Stresses

for 1% Strain in Textured Magnesium Sheets

		Pure Mg		Mg-.5%Th		Mg-4%Li	
Locus Point	Specimen orient.	Stress (ksi)	Slope	Stress (ksi)	Slope	Stress (ksi)	Slope
a	R_{tens}	10.5	6.5	26.7	4.6	13.9	2.5
b	ZR	10.9	∞	27.0	∞	16.7	∞
c	Z_{comp}	10.3	-2.5	27.5	-.7	14.3	-.7
d	ZT	19.5	0	26.6	0	15.9	0
e	T_{tens}	18.8	.37	24.5	.37	11.6	.50
f	R_{comp}	3.7	9.5	14.2	17.0	10.0	4.5
g	RZ	3.8	∞	14.3	∞	10.1	∞
h	TZ	4.4	0	14.7	0	10.0	0
i	T_{comp}	4.1	.18	14.6	.07	9.4	.14
j	TR	10.8	1.0	24.6	1.0	10.7	1.0
k	RT	15.0	1.0	24.4	1.0	11.2	1.0

in the rolling direction. The low strengths in compression are due to yielding by $\{10\bar{1}2\}$ twinning since this mode is active in compression but not in tension along the c-axis. The texture, with strong alignment of the basal pole in the thickness direction (Fig. 17), is such that $\{10\bar{1}2\}$ twinning is readily activated by compression perpendicular to this direction. The tensile strength in the rolling direction is significantly lower than in the transverse direction owing to the greater spread of the texture about the transverse direction, thus permitting more widespread operation of basal slip under conditions of rolling direction stress.

Mg-.5%Th yield locus: The yield locus for the textured magnesium-thorium alloy (Fig. 24) is much more elliptical than is the locus for pure magnesium. In the thorium-bearing alloy the yield strengths for the transverse and rolling directions are essentially identical, and also are markedly greater than those of the pure metal. These observations are explained by the relatively symmetrical pole figure (Fig. 19) and the solution hardening effect of the thorium. In addition, the compressive yield strengths of the alloy are from 60 to 65% of the values for the tensile yield strengths, whereas in the pure metal the compressive yield strengths are only 20 to 40% of the tensile values. This reflects the greater effect of solution hardening on $\{10\bar{1}2\}$ twinning than on $\{10\bar{1}1\}$ banding that was observed in the single crystal tests, in addition to the weaker texture.

Mg-4%Li yield locus: The yield locus for the textured magnesium-lithium material is similar in shape to that for the thorium-bearing alloy (see Fig. 24), but with greatly reduced yield stress values even though solute strengthening is slightly greater in the Mg-4%Li. These reduced values are the result of the occurrence of prism slip and of the weaker crystallographic texture. The prism slip is considered to have a greater influence in reducing the strengths in the second and fourth quadrants of the yield locus because the biaxial stress states (orthogonal combinations of tension and compression) in these quadrants are the most favorable for the prism slip mode. The reduction of yield strengths in the first and third quadrants, on the other hand, is attributed primarily to the weak texture of the alloy which allows the activation of basal slip in a greater fraction of the grains. The compressive yield strengths more nearly approach the tensile values in the lithium-bearing alloy also because of the weakness of the texture.

CONCLUSIONS

As a result of this investigation the following conclusions have been drawn:

1. $\{10\bar{1}1\}$ banding, consisting of $\{10\bar{1}1\}$ twinning followed by $\{10\bar{1}2\}$ retwinning and basal slip within the doubly twinned band, is a significant deformation mechanism, along with basal slip and $\{10\bar{1}2\}$ twinning, in pure magnesium at room temperature. Neither $\{10\bar{1}0\}\langle 1\bar{2}10\rangle$ prism slip nor $\{10\bar{1}1\}\langle 1\bar{2}10\rangle$ pyramidal slip, both previously reported, are confirmed at room temperature. Instead, in crystals ideally oriented for these modes, deformation occurs by $\{10\bar{1}1\}$ banding operating simultaneously with $\{10\bar{1}2\}$ twinning. It is concluded that activation shear stresses for prism and pyramidal slip are greater at room temperature than ~8.7 ksi and ~7.6 ksi respectively.

2. Fracture in pure magnesium occurs on $\{11\bar{2}4\}$ under compression along the c-axis, and on $\{10\bar{1}1\}$ by compression perpendicular to the c-axis.

3. Thorium of .5 wt% in magnesium raises the activation stresses for basal slip and $\{10\bar{1}2\}$ twinning, but not for $\{10\bar{1}1\}$ banding or for fracture.

4. Lithium of 4 wt% in magnesium reduces the resistance to $\{10\bar{1}0\}\langle 1\bar{2}10\rangle$ prism slip so that it becomes active at room temperature, while the basal slip and $\{10\bar{1}2\}$ twinning systems are hardened. Under compression along the

c-axis, 4 wt% lithium lowers the fracture strength and changes the fracture habit from $\{11\bar{2}4\}$ to $\{10\bar{1}1\}$.

5. Yielding in polycrystalline aggregates of magnesium is extremely dependent on the texture of the material and the shear stresses required to activate the various deformation modes.

APPENDIX A

THE PRODUCTION OF SINGLE CRYSTALS

The single crystals necessary for plane-strain compression specimens were grown from seed crystals by a modified Bridgeman technique. The seed crystals were grown under helium in a solid graphite channel in a horizontal resistance furnace moving at a speed of approximately 1 cm/hr. Seed crystals thus produced were checked for crystallographic orientation by the Laue back-reflection x-ray method. Each of those with an orientation suitable for use in seeding was then clamped into a fixture which allowed accurate orientation adjustment by three rotations. The fixture was designed to hold both a seed and the polycrystalline blank from which the single crystal was to be grown. By x-raying the seed in the fixture it was accurately oriented with respect to the polycrystalline blank, and then heliarc welded to one end of the 1/4 in. by 1/2 in. by 6 in. blank.

Each polycrystalline blank was converted into a single crystal of a desired orientation in a graphite mold utilized to hold the blank and seed. The mold was placed in the furnace which was now positioned nearly vertically to facilitate the gravity feeding of the molten metal to the solidifying crystal during the growing process. The furnace was brought up to temperature while centered about the

upper end of the mold, melting the upper portion of the polycrystalline blank. The furnace was then lowered slowly until the blank was entirely molten and the liquid-solid interface was stabilized in the single crystal seed. At this point an electric motor was used to move the furnace upward at about 1 cm/hr, allowing the molten metal to solidify with the liquid-solid interface moving upward from the seed. A helium atmosphere was employed in the furnace during the crystal growing operation. The center of the furnace was maintained at approximately 60°C above the melting point of magnesium with an appropriate fixed setting of the power input.

For the two compositions, pure magnesium and Mg-.5%Th, a cylindrical split-mold of solid graphite was employed that incorporated a channel of rectangular cross section (1/4 in. by 1/2 in.) running the length of the mold. The channel was enlarged at the bottom of the mold for a length of about three inches to permit the seed to be tightly packed in powdered graphite. The mold was held together with graphite caps at both ends. The upper cap had a small hole to vent the mold to the helium atmosphere of the furnace tube and the lower cap was equipped with a thermocouple so that the seed temperature might be monitored during the crystal growing process.

Because molten magnesium-lithium alloys react with graphite a modified mold was developed for growing crystals of the 4% lithium alloy. Instead of a solid split-mold,

a graphite hollow tube split-mold was used in which the entire blank and its attached seed could be packed in powdered MgO. A large opening through the MgO packing at the upper end served to accommodate the expansion and contraction of the metal during the crystal growing operation. Except for the modified mold, the technique for growing single crystals of Mg-4%Li was identical to that used with the other materials.

Although pure magnesium crystals could be grown at furnace speeds of up to at least 3 cm/hr, furnace speeds of more than about 1 cm/hr resulted in the nucleation of random grains in alloy crystals. Furthermore, the alloy compositions were prone to the development of randomly oriented grains at the seed-to-blank junction unless a generous taper was provided at that point. Microscopically, the pure magnesium crystals appeared to be relatively free from defects and substructure. The alloy crystals, however, exhibited well developed substructure which was readily discernible under the microscope.

Representative single crystals of the two alloy compositions were analyzed by Dow Chemical Company for end-to-end segregation of the alloying elements. Spectrographic analyses of the Mg-.5%Th alloy disclosed that end-to-end segregation was significant with the thorium concentration increasing from approximately .3 wt% at mid-length to about .5 wt% at the last-to-freeze end of the crystal. Chemical analyses indicated that end-to-end

segregation was less severe in the Mg-4%Li alloy with the lithium concentration ranging from 3.2% at mid-length to 3.8% at the last-to-freeze end. In view of these results all alloy single crystal specimens were taken from locations in the crystals between mid-length and the last-to-freeze end.

APPENDIX B

PLANE-STRAIN COMPRESSION TESTING PROCEDURE

Plane-strain compression tests were made in a hardened steel fixture on an Instron testing machine. The test fixture consisted of a channel with provision for width adjustment and an indentor designed to fit down into the channel. The indentor was mounted on the end of a supporting shaft which also served to actuate a cantilever beam deflectometer bolted to the top of the steel channel (see Fig. 1). The deflectometer utilized two SR-4 strain gauges as sensing elements permanently affixed to the cantilever beam.

The channel portion of the test fixture was bolted to the base of a steel die holder and the indentor support shaft was affixed to the movable top piece of the die holder (see Fig. 1). The die holder provided accurate and reproducible alignment of the indentor in the channel and also insured precise vertical movement of the indentor during compression. The specimens were placed in the test fixture with 2-mil teflon film between the specimen and the contacting surfaces of the channel. The adjustable side of the fixture was then tightened with finger pressure on the adjusting screw to provide width constraint of the specimen during the test. The indentor was placed on the top of the specimen with teflon film between the indentor and the

specimen.

For testing, the die holder was positioned on the platform of the compression load cell of the Instron and the load was applied to the top of the die holder by the Instron crosshead. The specimen was compressed at a rate of .01 in/min (a strain rate of ~.0067 sec^{-1} for the 1/4 in. specimens).

Load data was taken directly from the Instron recorder while deformation data was obtained from three independent sources which were used to check one another. The first of these was the crosshead displacement which was recorded automatically by the Instron recorder. This was corrected to account for the elasticity of the Instron and test fixture by running calibrating tests on a hardened steel specimen. A second system utilized to measure deformation was the SR-4 deflectometer connected to a strain indicator. The third source of deformation data was micrometer measurements of the specimen before and after compression. In some instances compression tests were halted at selected increments of load and the specimen removed from the fixture so that it could be measured with the micrometer to insure positive plastic deformation data in critical regions of the stress-strain curve. A dial indicator actuated by the movable jaw of the test fixture served to insure that the width constraint that existed before removal of the specimen was accurately reapplied when the specimen was reinserted into the fixture for further deformation. This

technique was most helpful in the low strain region of the curve where plastic strain was just beginning.

APPENDIX C

ANALYSIS OF THE FRICTIONAL EFFECTS IN COMPRESSION TESTS

The stress relationships in plane-strain compression can be represented as indicated below. The y direction has been taken as the axis of compression, z the lateral (constraint) direction, and x the direction of extension. The coefficient of friction is indicated by μ; and L, h and w are the dimensions of the specimen in the respective directions, x, y and z.

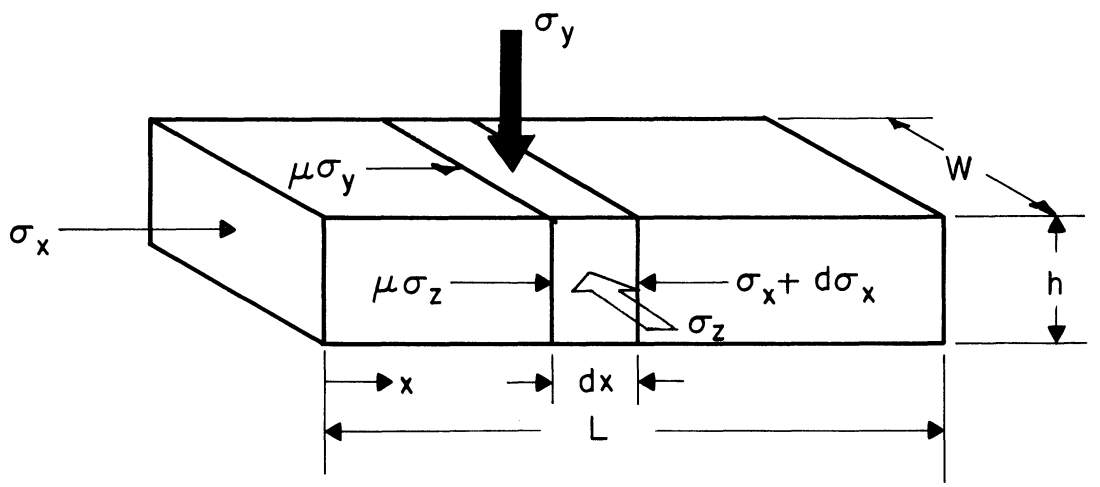

Consider the forces acting on an element of the specimen under the applied stress, σ_y. A force balance in the x direction gives:

$$(hw)\sigma_x + 2(hdx)\mu\sigma_z + 2(wdx)\mu\sigma_y = (hw)(\sigma_x + d\sigma_x) \qquad (1)$$

In plane-strain, the lateral constraining stress, σ_z, may be approximated by assuming that the Hencky-Mises flow rules apply even though the material is anisotropic. This gives:

$$\epsilon_z = 1/\lambda \left[\sigma_z - \tfrac{1}{2}(\sigma_x + \sigma_y)\right] \tag{2}$$

In plane-strain, where $\epsilon_z = 0$, (2) leads to:

$$\sigma_z = \tfrac{1}{2}(\sigma_x + \sigma_y) \tag{3}$$

For plane-strain yielding (where σ_o = yield stress):

$$\sigma_y - \sigma_x = \sigma_o \tag{4}$$

$$\sigma_x = \sigma_y - \sigma_o \tag{5}$$

$$d\sigma_x = d\sigma_y \tag{6}$$

Substituting (3) and (5) into (1) and simplifying:

$$d\sigma_x = \frac{\mu}{hw}\, dx \left[2(h+w)\sigma_y - h\sigma_o\right] \tag{7}$$

Substituting (6) into (7):

$$d\sigma_y = \frac{\mu}{hw}\, dx \left[2(h+w)\sigma_y - h\sigma_o\right] \tag{8}$$

$$2\frac{(h+w)}{hw}\mu\, dx = d\sigma_y \,/\, \left(\sigma_y - \frac{h}{2(h+w)}\sigma_o\right) \tag{9}$$

Integrating:

$$2\frac{(h+w)}{hw}\mu \int_o^x dx = \int_{\sigma_o}^{\sigma_y} d\sigma_y \,/\, \left(\sigma_y - \frac{h}{2(h+w)}\sigma_o\right)$$

$$2\frac{(h+w)}{hw}\mu x = \ln\frac{\sigma_y - \frac{h}{2(h+w)}\sigma_o}{\sigma_o\left[1 - \frac{h}{2(h+w)}\right]} \tag{10}$$

Rewriting, and letting $k = h/2(h+w)$:

$$\sigma_y = k\sigma_o + (\sigma_o - k\sigma_o)\, e^{\frac{\mu}{kw}x} \tag{11}$$

The average compressive stress in plane-strain, $\overline{\sigma}_{y_{ps}}$, at yielding is:

$$\overline{\sigma}_{y_{ps}} = \frac{\int \sigma_y dx}{\int dx} \tag{12}$$

$$\overline{\sigma}_{y_{ps}} = \frac{2\int_o^{L/2}\left[k\sigma_o + (\sigma_o - k\sigma_o)e^{\frac{\mu}{kw}x}\right]dx}{2\int_o^{L/2} dx} \tag{13}$$

$$\overline{\sigma}_{y_{ps}} = k\sigma_o + \frac{2}{L}(\sigma_o - k\sigma_o)\frac{kw}{\mu}\left[e^{\frac{\mu L}{2kw}} - 1\right] \tag{14}$$

By series expansion of $e^{\frac{\mu L}{2kw}}$:

$$\overline{\sigma}_{y_{ps}} = k\sigma_o + \frac{2}{L}(\sigma_o - k\sigma_o)\frac{kw}{\mu}\left[1 + \frac{\mu L}{2kw} + \frac{1}{2}\left\{\frac{\mu L}{2kw}\right\}^2 + \ldots - 1\right] \tag{15}$$

$$\overline{\sigma}_{y_{ps}} = k\sigma_o + (\sigma_o - k\sigma_o)\left[1 + \frac{\mu L}{4kw}\right] \tag{16}$$

Substituting for k:

$$\overline{\sigma}_{y_{ps}} = \sigma_o\left[1 + \frac{\mu L(2W+h)}{4hw}\right] \tag{17}$$

In this work, $w \approx 2h$ for all specimens. Therefore:

$$\bar{\sigma}_{y_{ps}} = \sigma_o \left[1 + \frac{5\mu L}{8h}\right] \tag{18}$$

For frictionless plane-strain:

$$\sigma_o = 1.15\bar{\sigma}_y \tag{19}$$

From the aluminum data (where $L = 1.8h$):

$$\bar{\sigma}_{y_{ps}} = 1.33\bar{\sigma}_{y_{tensile}} \tag{20}$$

Substituting (20) into (19):

$$\sigma_o = 1.15(\bar{\sigma}_{y_{ps}} / 1.33) \tag{21}$$

Substituting for σ_o from (18):

$$\bar{\sigma}_{y_{ps}} / \left[1 + (1.8)(5/8)\mu\right] = .86\bar{\sigma}_{y_{ps}} \tag{22}$$

$$\mu = .147 \tag{23}$$

Let f be a frictional factor such that:

$$\sigma_o = f\bar{\sigma}_y \tag{24}$$

Substituting (18) into (24) and using the average L/h of 1.3:

$$f_{plane\text{-}strain} = 1/\left[1 + (L/h)(5/8)\mu\right]$$

$$= 1/\left[1 + (1.3)(5/8)(.147)\right]$$

$$f_{plane\text{-}strain} = .89 \quad \text{for plane strain loading}$$

For uniaxial compression, $\sigma_z = 0$, and a similar mathematical analysis will produce:

$$\bar{\sigma}_{y_{ua}} = \sigma_o \left[1 + (L/h)(1/2)\mu\right] \qquad (25)$$

Substituting (25) into (24):

$$f_{uniaxial} = 1/\left[1 + (L/h)(1/2)\mu\right]$$

$$f_{uniaxial} = .91 \qquad \text{for uniaxial loading}$$

APPENDIX D

YIELD STRESSES FOR $\{10\bar{1}1\}$ BANDING IN ORIENTATIONS C AND D

The $\{10\bar{1}1\}$ banding mechanism in orientations C and D involves the simultaneous operation of $\{10\bar{1}2\}$ twinning against c-axis constraint and $\{10\bar{1}1\}$ twinning as a result of the constraint stress. The shear stress to activate the $\{10\bar{1}1\}$ twinning is generated by the constraining stress built up through the operation of $\{10\bar{1}2\}$ twinning. Although the $\{10\bar{1}1\}$ twinning probably has an activation shear stress greater than the average stress on the crystal at the time banding begins, the latter is taken to be representative of the yield stress for banding in this analysis. Furthermore, because orientations C and D are equally favorable for non-basal slip, any orientation factor in the activation stress for $\{10\bar{1}1\}$ twinning is assumed to be identical for the two orientations. Therefore, for C and D-oriented crystals, one activation shear stress is assumed to exist for $\{10\bar{1}1\}$ banding and another for $\{10\bar{1}2\}$ twinning. The compressive stress to cause yielding in each orientation, then, is that loading stress that raises the constraint stress sufficiently to activate $\{10\bar{1}1\}$ banding on an appropriate system. The analysis developed here is only assumed to hold for the beginning of banding where $\{10\bar{1}2\}$ twinning against c-axis constraint operates simultaneously with $\{10\bar{1}1\}$ twinning.

To show that the compressive stress for yielding is the same in orientation C as it is in orientation D, identical expressions are derived below for both.

Let:

α = shear stress to activate $\{10\bar{1}2\}$ twins

β = shear stress to activate $\{10\bar{1}1\}$ bands

σ_y = compressive load stress at yielding

σ_z = constraint stress at yielding

m = Schmid's law factor ($\cos\phi\cos\lambda$)

Orientation C

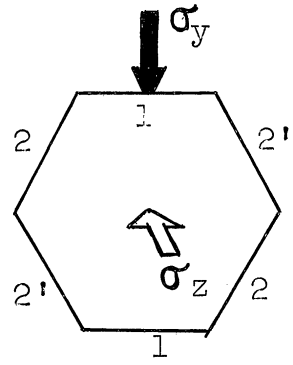

At yielding, $\{10\bar{1}2\}$ twinning on systems 1 is activated by σ_y with $\phi_{\alpha 1} = 47^\circ$ and $\lambda_{\alpha 1} = 43^\circ$. $\{10\bar{1}1\}$ banding is activated by σ_z on systems 2 with $\phi_{\beta 2} = 62^\circ$ and $\lambda_{\beta 2} = (180-28)^\circ$. Therefore:

$$m_{y\alpha 1} = \cos 47^\circ \cos 43^\circ = .499$$

$$m_{z\alpha 1} = \cos 43^\circ \cos(180-47)^\circ = -.499$$

$$m_{z\beta 2} = \cos 62^\circ \cos(180-28)^\circ = -.414$$

$$m_{y\beta 2} = \cos 28^\circ \cos 62^\circ \cos^2 60^\circ = .414\cos^2 60^\circ$$

Resolution of stresses at yielding gives:

$$\alpha = \sigma_y m_{y\alpha 1} + \sigma_z m_{z\alpha 1} \quad (1)$$

$$\beta = \sigma_y m_{y\beta 2} + \sigma_z m_{z\beta 2} \quad (2)$$

Rewriting (1):

$$\sigma_z = \frac{1}{-.499}\left(\alpha - .499\sigma_y\right) \quad (3)$$

Substituting (3) into (2):

$$\beta = \sigma_y .414\cos^2 60^\circ + \frac{.414}{.499}(\alpha - .499\sigma_y) \quad (4)$$

$$\sigma_y = (\beta - .830\alpha)/\left[-.414(1-\cos^2 60^\circ)\right] \quad (5)$$

$$\sigma_y = (\beta - .830\alpha)/\left[-.414\cos^2 30^\circ\right] \quad (6)$$

Orientation D

At yielding, $\{10\bar{1}2\}$ twinning is activated by σ_y on systems 3 and $\{10\bar{1}1\}$ banding is activated by σ_z on systems 4. Then:

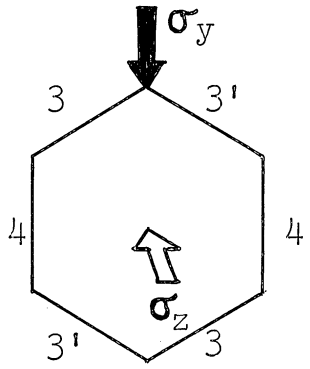

$$m_{y\alpha 3} = \cos 47^\circ \cos 43^\circ \cos^2 30^\circ = .499\cos^2 30^\circ$$
$$m_{z\alpha 3} = \cos 43^\circ \cos(180-47)^\circ = -.499$$
$$m_{z\beta 4} = \cos 62^\circ \cos(180-28)^\circ = -.414$$
$$m_{y\beta 4} = \cos 28^\circ \cos 62^\circ \cos^2 90^\circ = 0$$

Resolution of stresses at yielding gives:

$$\alpha = \sigma_y m_{y\alpha 3} + \sigma_z m_{z\alpha 3} \quad (7)$$

$$\beta = \sigma_y m_{y\beta 4} + \sigma_z m_{z\beta 4} \quad (8)$$

Rewriting (7):

$$\sigma_z = \frac{1}{-.499}(\alpha - \sigma_y .499\cos^2 30^\circ) \quad (9)$$

Substituting (9) into (8):

$$\beta = 0\sigma_y + \frac{.414}{.499}(\alpha - \sigma_y .499\cos^2 30^\circ) \quad (10)$$

$$\sigma_y = (\beta - .830\alpha)/\left[-.414\cos^2 30^\circ\right] \qquad (11)$$

Equations (6) and (11) are identical and therefore:

$$\sigma_{y_C} = \sigma_{y_D}$$

Thus, the loading stresses for $\{10\bar{1}1\}$ banding are identical in orientations C and D.

BIBLIOGRAPHY

1. C. S. Roberts, Magnesium and its Alloys, Chapt. 4, Wiley and Sons (1960).

2. R. E. Reed-Hill and W. D. Robertson, "Deformation of Magnesium Single Crystals by Non-basal Slip", AIME Trans., 209, p 496 (1957).

3. F. E. Hauser, P. R. Landon and J. E. Dorn, "Deformation and Fracture Mechanisms of Polycrystalline Magnesium at Low Temperatures", Trans. ASM, 48, p 986 (1955).

4. P. W. Flynn, J. Mote and J. E. Dorn, "On Thermally Activated Mechanism of Prismatic Slip in Magnesium Single Crystals", AIME Trans., 221, p 1148 (1961).

5. C. S. Barrett and C. T. Haller, "Twinning in Polycrystalline Magnesium", AIME Trans., 171, p 246 (1947).

6. R. E. Reed-Hill and W. D. Robertson, "Additional Modes of Deformation Twinning in Magnesium", Acta Met, 5, p 717 (1957).

7. G. I. Taylor, "Plastic Strain in Metals", J. Inst. Metals, 62, p 307 (1938).

8. B. C. Wonsiewicz and W. A. Backofen, to be published (Wonsiewicz Ph.D. Thesis, MIT, 1966).

9. E. C. Burke and W. R. Hibbard, "Plastic Deformation of Magnesium Single Crystals", AIME Trans., 194, p 295 (1952).

10. S. L. Couling, J. F. Pashak and L. Sturkey, "Unique Deformation and Aging Characteristics of Certain Mg-based Alloys", Trans. ASM, 51, p 94 (1959).

11. R. E. Reed-Hill, "A Study of the $\{10\bar{1}1\}$ and $\{10\bar{1}3\}$ Twinning Modes in Magnesium", AIME Trans., 218, p 554 (1960).

12. S. L. Couling, Dow Chemical Company, private communication.

13. R. E. Reed-Hill and W. D. Robertson, "Crystallographic Characteristics of Fracture in Magnesium Single Crystals", Acta Met, 5, p 728 (1957).

14. W. F. Sheely and R. R. Nash, "Mechanical Properties of Magnesium Monocrystals", AIME Trans., 218, p 417 (1960).

15. H. Yoshinaga and R. Horiuchi, "On the Nonbasal Slip in Magnesium Crystals", Trans. Jap. Inst. of Metals, 5, p 14 (1963).

16. R. L. Bell and R. W. Cahn, "The Dynamics of Twinning and the Interrelation of Slip and Twinning in Zinc Crystals", Proc. Roy. Soc., A239, p 494 (1957).

17. R. E. Reed-Hill and W. D. Robertson, "Pyramidal Slip in Magnesium", AIME Trans., 212, p 256 (1958).

18. W. F. Sheely, E. D. Levine and R. R. Nash, "Temperature Dependence of the Critical Stress for Slip in Magnesium Alloy Monocrystals", AIME Trans., 215, p 693 (1959).

19. F. E. Hauser, P. R. Landon and J. E. Dorn, "Deformation and Fracture of α Solid Solution of Lithium in Magnesium", Trans. ASM, 50, p 856 (1958).

20. H. Yoshinaga and R. Horiuchi, "On the Flow Stress of α Solid Solution Mg-Li Alloy Single Crystals", Trans. Jap. Inst. of Metals, 4, p 134 (1963).

21. R. Hill, Mathematical Theory of Plasticity, Chapt. XII, Oxford Univ. Press (1960).

22. W. F. Hosford, Jr. and W. A. Backofen, "Strength and Plasticity of Textured Metals", Fundamentals of Deformation Processing, Syracuse Univ. Press, p 259 (1964).

23. W. F. Hosford, Jr., "Texture Strengthening", ASM Metals Engr. Qtrly., 6, No. 4, p 13 (1966)

24. D. C. Drucker, "A More Fundamental Approach to Plastic Stress-Strain Relations", Proc. 1st U.S. Nat. Cong. of Appl. Mech., p 487 (1951).

DATA

PLAIN-STRAIN COMPRESSION

Plain-strain compression data is presented in four columns for each specimen as follows:

1st column - applied load (thousands of pounds)
2nd column - height of specimen in load direction (inches)
3rd column - calculated true stress (ksi)
4th column - calculated true strain (percent)

Specimen original width and length is given in parentheses following the specimen identification.

* denotes specimen fracture

$ indicates that the test was halted after each increment of load, the specimen removed and measured with micrometers, and the specimen then reinserted and the load reapplied. The specimen heights given are micrometer data.

PURE MAGNESIUM SINGLE CRYSTALS (in plane-strain compression):

A11 (.485"x.450")

0.0	.2516	0.0	0.00
3.0	.2509	13.7	0.28
4.0	.2504	18.3	0.47
5.0	.2497	22.9	0.76
6.0	.2490	27.5	1.04
7.0	.2481	32.1	1.40
8.0	.2471	36.6	1.80
9.0	.2459	41.2	2.28

A21 (.490"x.450")

0.0	.2508	0.0	0.00
3.0	.2502	13.6	0.24
4.0	.2497	18.2	0.44
5.0	.2487	22.7	0.84
6.0	.2475	27.2	1.33
7.0	.2465	31.7	1.72
8.0	.2453	36.3	2.21

A22 (.490"x.450")

0.0	.2519	0.0	0.00
3.0	.2513	13.6	0.24
4.0	.2507	18.2	0.47
5.0	.2499	22.7	0.80
6.0	.2489	27.2	1.19
7.0	.2478	31.7	1.64
8.0	.2467	36.3	2.08
9.0	.2452	40.9	2.70

A23 (.480"x.450")

0.0	.2453	0.0	0.00
3.0	.2445	13.9	0.32
4.0	.2439	18.5	0.57
5.0	.2432	23.2	0.86
6.0	.2422	27.8	1.26
7.0	.2412	32.4	1.68
8.0	.2398	37.0	2.28
9.0	.2382	41.7	2.94
9.4	.2370	43.6	3.45

A24 (.480"x.450")

0.0	.2438	0.0	0.00
3.0	.2433	13.9	0.21
4.0	.2428	18.5	0.41
5.0	.2423	23.2	0.62
6.0	.2416	27.8	0.91
7.0	.2409	32.4	1.19
8.0	.2399	37.0	1.61
9.0	.2385	41.7	2.20
9.9	.2371	46.3	2.82

A25 (.480"x.4297")

0.0	.2419	0.0	0.00
2.0	.2409	9.7	0.42
3.0	.2403	14.4	0.67
4.0	.2398	19.1	0.87
5.0	.2392	23.9	1.12
6.0	.2383	28.6	1.50
7.0	.2373	33.3	1.92
8.0	.2359	37.9	2.51
9.0	.2342	42.5	3.24
9.9	.2320	46.9	4.17

A26 (.480"x.4065")

0.0	.2432	0.0	0.00
4.0	.2413	20.3	0.78
5.0	.2405	25.3	1.11
6.0	.2399	30.3	1.35
7.0	.2387	35.2	1.86
8.0	.2374	40.0	2.41
9.0	.2355	44.7	3.21
9.8*	.2334	48.2	4.11

A27 (.480"x.4101")

0.0	.2457	0.0	0.00
3.0	.2448	15.2	0.36
4.0	.2443	20.2	0.57
5.0	.2439	25.2	0.72
6.0	.2430	30.1	1.10
7.0	.2421	35.0	1.45
8.0	.2408	39.8	2.01
9.0	.2390	44.5	2.76
9.4	.2382	46.3	3.10

B12 (.485"x.450")

0.0	.2548	0.0	0.00
2.0	.2541	9.2	0.27
3.0	.2436	13.8	0.47
4.0	.2531	18.3	0.67
5.0	.2526	22.9	0.87
6.0	.2521	27.5	1.07
7.0	.2515	32.1	1.30
8.0	.2508	36.6	1.58
9.0	.2497	41.2	2.02
9.5	.2483	43.5	2.57

B14 (.480"x.3922")

0.0	.2450	0.0	0.00
2.0	.2441	10.6	0.36
3.0	.2436	15.8	0.57
4.0	.2430	21.1	0.82
5.0	.2422	26.2	1.15
6.0	.2414	31.4	1.48
7.0	.2405	36.5	1.85
8.0	.2395	41.5	2.27
9.0	.2381	46.5	2.85
9.1*	.2370	46.8	3.33

B15 (.480"x.3963")

0.0	.2488	0.0	0.00
2.0	.2478	10.5	0.40
3.0	.2472	15.7	0.64
4.0	.2465	20.8	0.93
5.0	.2457	26.0	1.25
6.0	.2448	31.1	1.62
7.0	.2439	36.1	1.98
8.0	.2424	41.0	2.60
8.4	.2406	42.8	3.35

B19 (.480"x.3122") $

0.0	.2462	0.0	0.00
1.0	.2461	6.7	0.04
2.0	.2458	13.4	0.16
4.0	.2450	26.6	0.48
6.0	.2431	39.5	1.26

B21 (.480"x.450")

0.0	.2471	0.0	0.00
2.0	.2465	9.3	0.24
3.0	.2460	13.9	0.45
4.0	.2455	18.5	0.65
5.0	.2450	23.2	0.85
6.0	.2445	27.8	1.06
7.0	.2439	32.4	1.30
8.0	.2429	37.0	1.70
9.0	.2420	41.7	2.08
9.9*	.2401	46.3	2.90

B22 (.480"x.450")

0.0	.2470	0.0	0.00
2.0	.2461	9.3	0.36
5.0	.2446	23.2	0.98
8.0	.2422	37.0	1.95
9.9	.2401	46.3	2.85

o*o*o*o

G15 (.485"x.450")

.00	.2397	.00	0.00
.02	.2386	.09	0.46
.04	.2375	.18	0.92
.06	.2362	.27	1.46
.08	.2345	.36	2.18
.10	.2285	.46	4.78
.15	.2040	.69	16.1
.20	.1990	.92	18.6
.30	.1832	1.4	21.6
.40	.1682	1.8	24.1
.50	.1537	2.3	26.5
.60	.1814	2.7	27.8

G16 (.485"x.450")

.00	.2394	.00	0.00
.04	.2382	.18	0.58
.06	.2375	.27	0.80
.08	.2367	.36	1.12
.10	.2337	.46	2.40
.15	.2110	.69	12.4
.20	.2075	.92	14.2
.30	.2022	1.4	16.7
.40	.1975	1.8	19.2
.50	.1932	2.3	21.4

G17 (.485"x.450")

.00	.2398	.00	0.00
.04	.2378	.18	0.84
.06	.2360	.27	1.59
.08	.2325	.36	3.09
.10	.2242	.46	6.72
.15	.1960	.69	20.1
.20	.1798	.92	28.7

C11 (.485"x.450")

0.0	.2495	0.0	0.00
1.0	.2488	4.6	0.28
2.0	.2481	9.2	0.56
3.0	.2472	13.7	0.93
4.0	.2465	18.3	1.21
5.0	.2456	22.9	1.57
5.5	.2446	25.2	1.98
6.0	.2422	27.5	2.97
6.4	.2382	29.3	4.63

C12 (.485"x.450")

0.0	.2497	0.0	0.00
1.0	.2489	4.6	0.32
2.0	.2481	9.2	0.64
3.0	.2475	13.7	0.88
4.0	.2466	18.3	1.24
5.0	.2456	22.9	1.65
6.0	.2447	27.5	2.02
6.5	.2439	29.8	2.35
7.0	.2406	32.1	3.71
7.1	.2357	32.6	5.75
7.0	.2319	32.1	7.40
6.9	.2306	31.6	7.95

C13 (.485"x.450")

0.0	.2505	0.0	0.00
1.0	.2498	4.6	0.28
2.0	.2491	9.2	0.56
3.0	.2485	13.7	0.80
4.0	.2479	18.3	1.03
5.0	.2472	22.9	1.31
6.0	.2466	27.5	1.56
6.5	.2458	29.8	1.89
6.9	.2415	31.6	3.66

C18 (.480"x.2750")

0.0	.2390	0.0	0.00
0.5	.2385	3.7	0.20
1.0	.2381	7.4	0.37
1.5	.2377	11.3	0.54
2.0	.2372	15.0	0.75
2.5	.2367	18.8	0.97
3.0	.2362	22.5	1.18
3.8	.2348	28.7	1.76
4.0	.2323	29.5	2.84
4.2	.2260	29.9	5.60
4.1	.2225	28.6	7.16

C19 (.480"x.2467")

0.0	.2346	0.0	0.00
0.5	.2340	4.2	0.25
1.0	.2334	8.4	0.51
1.5	.2328	12.6	0.77
2.0	.2321	16.7	1.06
2.5	.2317	20.8	1.24
3.0	.2306	24.9	1.71
3.3	.2291	26.8	2.37
3.5	.2259	28.5	3.78
3.6	.2227	28.9	5.20
3.1	.2198	24.6	6.51

C31 (.480"x.4300")

0.0	.2319	0.0	0.00
1.0	.2310	4.8	0.39
2.0	.2300	9.6	0.82
3.0	.2290	14.4	1.25
4.0	.2281	19.1	1.65
5.0	.2270	23.7	2.13
5.5	.2261	26.0	2.55
6.0	.2228	28.0	4.00
6.1	.2207	28.0	4.94
6.0	.2182	27.4	6.07
5.9	.2177	26.9	6.31

C34 (.480"x.3791")

0.0	.2346	0.0	0.00
2.0	.2326	11.0	0.94
3.0	.2316	16.3	1.19
4.0	.2306	21.6	1.70
5.0	.2282	26.8	2.76
5.5	.2256	28.9	4.80
6.0	.2156	30.5	8.45
6.1	.2136	30.4	9.36
6.0	.2116	29.8	10.3
5.0	.2003	23.8	15.8
3.7	.1874	16.9	22.4
4.0	.1771	18.5	28.1
5.0	.1555	23.2	41.0
6.0	.1086	27.8	77.0

D21 (.490"x.450")

0.0	.2508	0.0	0.00
1.0	.2496	4.5	0.48
2.0	.2485	9.1	0.92
3.0	.2474	13.6	1.36
4.0	.2463	18.2	1.81
5.0	.2450	22.7	2.33
5.5	.2440	25.0	2.74
6.0	.2421	27.2	3.53
6.3	.2363	28.6	5.95

D22 (.490"x.450")

0.0	.2512	0.0	0.00
1.0	.2502	4.5	0.40
2.0	.2492	9.1	0.80
3.0	.2482	13.6	1.20
4.0	.2472	18.2	1.60
5.0	.2460	22.7	2.08
5.5	.2453	25.0	2.37
6.0	.2432	27.2	3.24
6.2	.2390	27.9	4.97

D23 (.490"x.450")

0.0	.2512	0.0	0.00
1.0	.2504	4.5	0.32
2.0	.2496	9.1	0.64
3.0	.2488	13.6	0.96
4.0	.2480	18.2	1.28
5.0	.2467	22.7	1.80
5.5	.2456	25.0	2.25
6.0	.2438	27.2	3.00
6.2	.2413	28.1	4.04

D26 (.480"x.450")

0.0	.2415	0.0	0.00
1.0	.2404	4.6	0.46
2.0	.2396	9.3	0.79
3.0	.2388	13.9	1.12
4.0	.2379	18.5	1.50
5.0	.2368	23.2	1.97
6.0	.2349	27.8	2.76
6.2	.2320	28.7	4.00
6.3	.2270	29.2	6.19
6.5	.2175	30.1	10.6
6.7	.2127	31.0	12.7
6.9	.2060	31.9	15.8
6.7	.2000	31.0	18.9
6.5	.1970	30.1	20.4
6.2	.1941	28.7	21.9

D27 (.485"x.3865")

0.0	.2321	0.0	0.00
1.0	.2311	5.4	0.43
2.0	.2303	10.6	0.78
3.0	.2295	15.9	1.12
4.0	.2285	21.0	1.55
5.0	.2271	26.2	2.18
5.3	.2258	27.6	2.76
5.5	.2205	28.0	5.12
5.7	.2090	27.6	10.5
6.0	.2034	28.4	13.2
6.5	.1955	29.8	17.2
7.0	.1845	32.1	22.9
6.5	.1757	29.8	27.8
4.0	.1610	18.7	36.6

D28 (.480"x.3190") $

0.0	.2346	0.0	0.00
0.6	.2342	3.9	0.17
1.4	.2340	9.1	0.25
2.5	.2337	16.3	0.38
3.6	.2313	23.2	1.42
4.1	.2230	25.3	5.07
4.8	.1998	26.8	15.9

E11 (.485"x.450")

0.0	.2507	0.0	0.00
0.5	.2461	2.3	1.86
1.0	.2390	4.6	4.78
2.0	.2365	9.2	5.83
3.0	.2357	13.7	6.17
4.0	.2351	18.3	6.42
5.0	.2346	22.9	6.55
6.0	.2341	27.5	6.85
7.0	.2334	32.1	7.16
8.0	.2329	36.6	7.36

E12 (.490"x.450")

0.0	.2508	0.0	0.00
0.3	.2478	1.4	1.20
0.5	.2433	2.3	3.04
1.0	.2391	4.5	5.60
2.0	.2353	9.1	6.37
3.0	.2346	13.6	6.67
4.0	.2342	18.1	6.85
5.0	.2338	22.7	7.01
6.0	.2334	27.2	7.19
7.0	.2330	31.7	7.36
8.0	.2324	36.3	7.61
9.0	.2317	40.8	7.91
9.9	.2307	45.4	8.36

E24 (.480"x.3285")

0.0	.2250	0.0	0.00
0.2	.2223	1.3	1.20
0.3	.2190	1.9	2.70
0.5	.2150	3.1	4.55
1.0	.2127	6.0	5.62
2.0	.2117	12.0	6.10
3.0	.2113	17.9	6.27
4.0	.2109	23.9	6.47
5.0	.2103	29.8	6.76
6.0	.2095	35.6	7.14
7.0	.2086	41.4	7.57
8.0	.2077	47.1	7.98
9.0	.2068	52.8	8.44
9.9	.2060	58.4	8.83

E25 (.485"x .3452")

0.0	.2412	0.0	0.00
0.2	.2380	1.2	1.32
0.3	.2357	1.8	2.30
0.5	.2312	2.9	4.23
1.0	.2287	5.7	5.31
2.0	.2276	11.3	5.80
3.0	.2271	16.9	6.02
4.0	.2267	22.6	6.20
5.0	.2262	28.2	6.32
6.0	.2256	33.7	6.70
7.0	.2248	39.2	7.05
8.0	.2239	44.6	7.45
9.0	.2230	50.0	7.84
9.9	.2212	55.1	8.66

E27 (.485"x.2620")

0.0	.2271	0.0	0.00
0.5	.2198	3.8	3.27
1.0	.2161	7.5	4.96
1.5	.2151	11.2	5.42
2.0	.2148	14.9	5.57
3.0	.2141	22.3	5.90
4.0	.2134	29.6	6.22
5.0	.2127	36.9	6.56
6.0	.2117	44.1	7.04
7.0	.2104	51.2	7.65
8.0	.2088	58.0	8.51
8.4*	.2079	60.7	8.91

E28 (.485"x.2730")

0.0	.2406	0.0	0.00
0.5	.2323	3.6	3.50
1.0	.2272	7.1	5.73
1.5	.2261	10.7	6.22
2.0	.2256	14.2	6.44
3.0	.2250	21.2	6.70
4.0	.2242	28.2	7.07
5.0	.2233	35.1	7.46
6.0	.2222	42.0	7.95
7.0	.2210	48.7	8.50
8.0	.2191	55.2	9.35
8.7*	.2169	59.6	10.3

E29 (.480"x.3015") $

0.0	.2412	0.0	0.00
0.1	.2410	0.8	0.08
0.2	.2404	1.4	0.33
0.3	.2391	2.1	0.87
0.4	.2371	2.7	1.71
0.5	.2352	3.4	2.52
1.0	.2301	6.6	4.70
3.5	.2263	22.8	6.33

F14 (.480"x.450")

0.0	.2402	0.0	0.00
0.2	.2392	0.9	0.41
0.5	.2379	2.3	0.96
0.7	.2355	3.5	1.97
1.0	.2329	4.6	2.85
1.3	.2305	6.0	4.03
1.6	.2288	7.4	4.86
2.0	.2270	9.3	5.66
3.0	.2253	13.9	6.40
4.0	.2245	18.5	6.76
5.0	.2240	23.2	6.98
6.0	.2233	27.8	7.30
6.5	.2227	30.1	7.56
6.9	.2195	31.9	9.01
6.5	.2155	30.1	10.8
6.0	.2103	27.8	13.3
5.0	.1970	23.2	19.8
4.5	.1850	20.8	26.2
4.0	.1645	18.5	37.9
4.2	.1505	19.4	46.7

F15 (.480"x.450")

0.0	.2307	0.0	0.00
0.2	.2297	0.9	0.44
0.5	.2285	2.3	0.95
0.7	.2269	3.5	1.66
1.0	.2244	4.6	2.77
1.3	.2215	6.0	4.07
1.6	.2197	7.4	4.89
2.0	.2181	9.3	5.62
3.0	.2168	13.9	6.21
4.0	.2162	18.5	6.50
5.0	.2155	23.2	6.82
6.0	.2149	27.8	7.10
6.5	.2144	30.1	7.33
6.9	.2118	31.9	8.55
6.5	.2053	30.1	12.4
6.0	.2007	27.8	13.9
5.0	.1890	23.2	19.9
4.5	.1787	20.8	25.5
4.3	.1725	19.9	29.0

F23 (.480"x.3557") $

0.0	.2433	0.0	0.00
0.3	.2402	2.0	1.29
0.5	.2375	2.9	2.40
0.9	.2328	5.3	4.40

F31 (.485"x.450")

0.0	.2519	0.0	0.00
0.5	.2488	2.3	1.32
1.0	.2450	4.6	3.60
1.5	.2379	6.9	5.72
2.0	.2356	9.2	6.68
3.0	.2337	13.7	7.50
4.0	.2327	18.3	7.92
5.0	.2320	22.9	8.22
6.0	.2310	27.5	8.64
6.9	.2275	31.6	10.4

F32 (.490"x.450")

0.0	.2523	0.0	0.00
0.5	.2487	2.3	1.16
1.0	.2436	4.5	3.50
1.5	.2384	6.8	5.66
2.0	.2362	9.1	6.59
3.0	.2341	13.6	7.50
4.0	.2333	18.2	7.82
5.0	.2327	22.7	8.09
6.0	.2315	27.2	8.60
6.9	.2295	31.3	9.37

F33 (.490"x.450")

0.0	.2522	0.0	0.00
0.5	.2480	2.3	1.67
1.0	.2421	4.5	4.08
1.5	.2375	6.8	6.00
2.0	.2352	9.1	6.96
3.0	.2334	13.6	7.74
4.0	.2325	18.2	8.13
5.0	.2317	22.7	8.46
6.0	.2309	27.2	8.82
6.7	.2286	30.4	9.80

Mg-.5%Th SINGLE CRYSTALS (in plane-strain compression):

TA11 (.480"x.450")

0.0	.2410	0.0	0.00
3.0	.2406	13.9	0.17
4.0	.2404	18.5	0.25
5.0	.2402	23.2	0.33
6.0	.2400	27.8	0.41
7.0	.2395	32.4	0.62
8.0	.2388	37.0	0.91
9.0	.2381	41.7	1.20
9.9	.2371	46.3	1.61

TA12 (.480"x.450")

0.0	.2440	0.0	0.00
3.0	.2436	13.9	0.16
4.0	.2434	18.5	0.25
5.0	.2431	23.2	0.37
6.0	.2427	27.8	0.53
7.0	.2421	32.4	0.78
8.0	.2413	37.0	1.10
9.0	.2405	41.7	1.43
9.9	.2396	46.3	1.80

TA14 (.485"x.2220")

0.0	.2400	0.0	0.00
1.0	.2393	9.3	0.29
2.0	.2384	18.6	0.67
3.0	.2370	27.8	1.25
4.0	.2355	36.8	1.88
5.0	.2338	45.7	2.61
5.5*	.2329	50.0	3.00

TA15 (.480"x.2220")

0.0	.2495	0.0	0.00
1.0	.2487	9.4	0.32
2.0	.2478	18.6	0.68
3.0	.2465	27.8	1.20
4.0	.2451	36.9	1.78
5.0	.2432	45.7	2.56
5.8*	.2405	52.7	3.68

TA17 (.485"x.3070") $

0.0	.2446	0.0	0.00
1.0	.2447	6.7	0.00
2.0	.2447	13.4	0.00
5.0	.2432	44.2	0.57
6.7	.2401		1.86

TB12 (.480"x.450")

0.0	.2430	0.0	0.00
3.0	.2424	13.9	0.24
5.0	.2416	23.2	0.57
7.0	.2409	32.4	0.87
8.0	.2403	37.0	1.11
9.0	.2394	41.7	1.48

TB14 (.480"x.450")

0.0	.2421	0.0	0.00
3.0	.2415	13.9	0.24
4.0	.2410	18.5	0.45
5.0	.2406	23.2	0.62
6.0	.2401	27.8	0.83
7.0	.2393	32.4	1.16
8.0	.2384	37.0	1.54
9.0	.2372	41.7	2.04
9.9	.2358	46.3	2.64

TB22 (.490"x.2437")

0.0	.2210	0.0	0.00
1.0	.2205	8.4	0.22
2.0	.2200	16.7	0.45
3.0	.2193	24.9	0.77
4.0	.2184	33.1	1.18
5.0	.2174	41.2	1.63
6.0	.2165	49.2	2.04
6.9*	.2149	56.2	2.79

TB21 (.490"x.2110")

0.0	.2410	0.0	0.00
1.0	.2400	9.6	0.41
2.0	.2390	19.2	0.83
3.0	.2379	28.6	1.30
4.0	.2368	38.0	1.75
5.0	.2356	47.3	2.26
6.0	.2340	56.4	2.96
6.1*	.2337	57.2	3.08

TB24 (.490"x.3801") $

0.0	.2415	0.0	0.00
1.0	.2412	5.4	0.12
2.0	.2412	10.7	0.12
3.5	.2409	18.8	0.24
5.0	.2399	26.7	0.62
8.0	.2389	42.5	1.08

TC13 (.480"x.450")

0.0	.2450	0.0	0.00
1.0	.2443	4.6	0.28
2.0	.2436	9.3	0.57
3.0	.2430	13.9	0.82
4.0	.2424	18.5	1.07
5.0	.2403	23.2	1.93
5.5	.2366	25.5	3.49
6.0	.2314	27.8	5.61
6.4	.2283	29.7	7.06

TC21 (.485"x.2180")

0.0	.2400	0.0	0.00
1.0	.2385	9.3	0.62
2.0	.2370	18.7	1.25
2.5	.2360	23.3	1.68
3.0	.2338	27.7	2.60
3.5	.2298	31.7	4.35
3.8	.2210	32.8	8.24
4.0	.2125	33.7	12.2
4.1	.2100	33.8	13.3
4.0	.2075	33.0	14.5
3.5	.1995	27.9	18.5
3.1	.1929	23.7	21.8

TC23 (.480"x.2634")

0.0	.2404	0.0	0.00
1.0	.2394	7.9	0.41
2.0	.2383	15.7	0.88
3.0	.2371	23.4	1.36
3.5	.2348	27.0	2.35
4.0	.2276	30.0	5.47
4.5	.2178	32.4	9.87
4.6	.2145	32.7	11.4
4.0	.2032	27.1	16.6
3.6	.1961	23.3	20.4

TC24 (.480"x.2565")

0.0	.2397	0.0	0.00
1.0	.2388	8.1	0.46
2.0	.2376	16.1	0.88
3.0	.2344	24.0	1.38
3.5	.2351	28.0	1.68
4.0	.2273	30.9	5.06
4.6	.2187	34.3	8.91

TD43 (.485"x.2869")

0.0	.1748	0.0	0.00
1.0	.1740	8.2	0.46
2.0	.1727	16.2	1.21
3.0	.1705	24.0	2.48
4.0	.1664	31.3	4.90
4.5	.1622	34.4	7.50
5.0	.1483	35.2	16.5
5.5	.1299	34.8	29.6
5.7	.1220	34.4	36.0
5.5	.1180	32.4	39.2

TD44 (.485"x.2410")

0.0	.1751	0.0	0.00
1.0	.1741	8.5	0.57
2.0	.1727	16.9	1.37
3.0	.1702	25.0	2.84
4.0	.1634	32.0	6.92
4.5	.1417	31.8	21.1
4.8	.1303	31.4	29.5
4.5	.1239	28.7	34.6
4.1	.1191	25.3	38.5

TD45 (.485"x.2460")

0.0	.1780	0.0	0.00
1.0	.1770	8.3	0.56
2.0	.1755	16.5	1.41
3.0	.1733	24.5	2.67
4.0	.1694	31.9	4.94
4.2	.1658	33.3	7.10
4.5	.1493	32.1	17.5
5.1	.1320	32.9	30.0
4.5	.1220	27.4	37.7

TD46 (.490"x.2491")

0.0	.1970	0.0	0.00
1.0	.1959	8.1	0.56
2.0	.1947	16.2	1.17
3.0	.1927	24.0	2.20
4.0	.1876	31.2	4.90
4.5	.1756	33.1	11.4
4.8	.1634	32.8	18.6
5.2	.1390	31.4	34.8
5.0	.1330	29.4	39.3

TD21 (.485"x.2869") $

0.0	.2432	0.0	0.00
1.0	.2432	7.2	0.00
2.0	.2425	14.3	0.28
3.0	.2419	21.4	0.53
4.5	.2375	31.5	2.36
5.0	.2177	32.0	11.0

TE14(.480"x.2120")

0.0	.2413	0.0	0.00
0.3	.2386	2.9	1.13
0.5	.2338	4.8	3.15
0.7	.2302	6.6	4.71
1.0	.2290	9.3	5.22
1.5	.2281	14.0	5.62
2.0	.2276	18.6	5.85
4.0	.2255	36.8	6.76
5.0	.2242	45.8	7.34
5.6*	.2212	50.6	8.70

TE15 (.485"x.1980")

0.0	.2478	0.0	0.00
0.3	.2452	3.0	1.06
0.5	.2410	5.0	2.78
0.7	.2365	7.0	4.66
1.0	.2345	9.9	5.52
1.5	.2335	14.7	5.95
2.0	.2329	19.6	6.21
3.0	.2319	29.3	6.63
5.0	.2292	48.2	7.83
6.0*	.2261	57.2	9.15

TE23 (.480"x.450")

0.0	.2480	0.0	0.00
0.3	.2464	1.4	0.65
0.5	.2452	2.3	1.13
0.7	.2435	3.2	1.83
1.0	.2398	4.6	3.35
1.5	.2355	6.9	5.27
2.0	.2342	9.3	5.72
4.0	.2330	18.5	6.24
6.0	.2320	27.8	6.66
8.0	.2309	37.0	7.15
9.9	.2297	46.3	7.69

TE26 (.485"x.2835") $

0.0	.2502	0.0	0.00
0.2	.2492	1.4	0.40
0.3	.2472	2.2	1.21
0.4	.2440	2.8	2.50
0.5	.2399	3.6	4.20
1.0	.2360	6.9	5.85
3.0	.2348	20.5	6.35
5.0	.2342	34.1	6.60

TF11 (.480"x.450")

0.0	.2511	0.0	0.00
0.5	.2503	2.5	0.32
1.0	.2489	4.6	0.88
1.5	.2469	6.9	1.70
2.0	.2437	9.3	3.00
3.0	.2365	13.9	5.98
4.0	.2341	18.5	7.02
5.0	.2331	23.2	7.45
6.0	.2322	27.8	7.82
7.0	.2311	32.4	8.30
8.3	.2262	38.4	10.4

TF12 (.480"x.450")

0.0	.2543	0.0	0.00
1.0	.2513	4.6	1.18
1.5	.2486	6.9	2.26
2.0	.2440	9.3	4.12
3.0	.2395	13.9	6.00
4.0	.2362	18.5	6.55
5.0	.2373	23.2	6.92
6.0	.2367	27.8	7.18
7.0	.2361	32.4	7.41
8.0	.2350	37.0	7.90
8.5	.2332	39.4	8.65

TF13 (.480"x.2130")

0.0	.2524	0.0	0.00
0.2	.2515	1.9	0.35
0.5	.2491	4.8	1.32
1.0	.2437	9.4	3.50
1.5	.2389	13.9	5.50
2.0	.2371	18.4	6.26
2.5	.2360	22.9	6.72
3.0	.2351	27.4	7.20
3.5	.2340	31.8	7.56
4.1	.2310	36.4	8.85
3.6	.2275	31.4	10.4

TF15 (.490"x.2888") $

0.0	.2556	0.0	0.00
0.2	.2553	1.4	0.11
0.4	.2540	2.8	0.62
0.6	.2519	4.2	1.46
1.0	.2468	6.8	3.50
2.0	.2408	13.3	5.96

Mg-4%Li SINGLE CRYSTALS (in plane-strain compression):

LA21 (.495"x.3000")

0.0	.1675	0.0	0.00
1.0	.673	6.7	0.12
2.0	.1670	13.4	0.29
3.0	.1667	20.1	0.47
4.0	.1663	26.7	0.72
5.0	.1656	33.3	1.14
6.0	.1646	39.7	1.75
6.6	.1638	43.5	2.22

LA23 (.490"x.2790")

0.0	.1760	0.0	0.00
1.0	.1757	7.3	0.17
2.0	.1754	14.6	0.34
3.0	.1750	21.8	0.57
4.0	.1744	29.0	0.91
5.0	.1734	36.0	1.48
5.8	.1724	41.2	2.06

LA25 (.490"x.3260")

0.0	.1817	0.0	0.00
1.0	.1814	6.3	0.16
2.0	.1811	12.5	0.33
3.0	.1807	18.7	0.55
4.0	.1802	24.8	0.83
5.0	.1794	30.9	1.27
6.0	.1780	36.8	2.04
6.6*	.1758	40.0	3.30

LA28 (.500"x.3636") $

0.0	.2010	0.0	0.00
1.0	.2010	5.2	0.00
2.0	.2010	10.4	0.00
3.5	.2008	18.2	0.10
5.0	.2003	26.0	0.35
7.5	.1980	38.5	1.50
7.7*	-	-	-

LB21 (.495"x.2296")

0.0	.2035	0.0	0.00
1.0	.2022	8.8	0.14
2.0	.2015	17.5	0.49
3.0	.2009	26.2	0.79
3.5	.2005	30.5	0.99
4.0	.2000	34.8	1.25
4.3	.1985	37.4	2.00

LB23 (.495"x.2470")

0.0	.2050	0.0	0.00
1.0	.2047	8.1	0.14
2.0	.2043	16.3	0.34
3.0	.2038	24.4	0.58
4.0	.2032	32.4	0.88
4.5	.2025	36.4	1.23
4.7	.2019	37.7	1.53

LB25 (.495"x.2170")

0.0	.2136	0.0	0.00
1.0	.2133	9.3	0.14
2.0	.2128	18.6	0.37
3.0	.2120	27.7	0.75
3.5	.2114	32.2	1.04
4.0	.2107	36.7	1.36
4.1	.2104	34.3	1.52

LB27 (.490"x.3241") $

0.0	.2412	0.0	0.00
1.0	.2412	6.3	0.00
2.0	.2412	12.6	0.00
3.5	.2412	22.0	0.00
5.0	.2408	31.5	0.16
5.9*	.2400	37.0	0.50

LC21 (.490"x.3080")

0.0	.1957	0.0	0.00
0.5	.1954	3.3	0.15
1.0	.1951	6.6	0.30
1.5	.1946	9.9	0.56
2.0	.1936	13.1	1.08
2.5	.1915	16.3	2.16
3.0	.1878	19.1	4.11
4.0	.1768	24.1	10.2
5.0	.1673	28.7	15.7
5.7	.1601	31.6	18.4

LC23 (.495"x.2690")

0.0	.2035	0.0	0.00
0.5	.2033	3.7	0.10
1.0	.2026	7.5	0.44
1.5	.2013	11.1	1.09
2.0	.1992	14.7	2.12
3.0	.1900	21.1	6.87
4.0	.1800	26.6	12.2
5.0	.1627	30.7	22.4
5.5	.1502	31.7	30.4
6.0	.1367	32.2	39.8
6.5	.1260	33.2	47.0
7.0	.1180	34.2	54.5

LC25 (.485"x.2610")

0.0	.1899	0.0	0.00
0.5	.1896	3.9	0.15
1.0	.1893	7.9	0.31
1.5	.1861	11.7	0.95
2.0	.1844	15.3	2.94
2.5	.1780	18.6	6.48
3.0	.1710	21.5	10.4
3.5	.1649	24.2	14.1
4.2	.1564	27.5	19.4

LC27 (.495"x.2579") $

0.0	.2230	0.0	0.00
1.0	.2229	7.8	0.04
1.5	.2211	11.8	0.85
2.3	.2155	17.0	3.42

LD42 (.490"x.2030")

0.0	.1689	0.0	0.00
0.5	.1678	5.0	0.65
1.0	.1666	9.9	1.37
1.5	.1652	14.7	2.20
2.0	.1626	.914	3.80
2.5	.1582	23.6	6.55
3.0	.1500	26.9	11.9
3.5	.1409	29.8	18.2
3.8	.1361	31.1	21.6

LD44 (.490"x.2050")

0.0	.1587	0.0	0.00
0.5	.1578	4.9	0.57
1.0	.1565	9.9	1.40
1.5	.1549	14.6	2.41
2.0	.1523	19.1	4.12
2.5	.1494	23.5	6.04
3.0	.1446	27.4	9.15
3.5	.1380	30.6	14.0
4.0	.1270	32.6	22.2

LD46 (.490"x.1940")

0.0	.2122	0.0	0.00
0.5	.2113	5.0	0.42
1.0	.2097	10.4	1.19
1.5	.2074	15.4	2.27
2.0	.2038	20.2	4.02
2.5	.1990	24.7	6.41
3.0	.1903	29.8	10.9
3.5	.1790	31.5	17.1

LD48 (.495"x.2312") $

0.0	.2607	0.0	0.00
0.5	.2604	4.4	0.11
1.0	.2590	8.7	0.65
1.6	.2564	13.6	1.66
2.0	.2527	17.0	3.10
2.8	.2388	22.2	8.80

LE42 (.495"x.2130")

0.0	.2379	0.0	0.00
0.2	.2373	2.0	0.25
0.5	.2334	4.7	1.90
0.8	.2285	6.8	4.01
1.0	.2254	9.0	5.38
1.5	.2238	13.4	6.10
2.0	.2231	17.8	6.42
3.0	.2223	26.6	6.87
4.0	.2215	35.4	7.18
4.1	.2208	36.2	7.45

LE44 (.495"x.2160")

0.0	.2261	0.0	0.00
0.3	.2240	2.8	0.93
0.5	.2190	4.5	3.18
0.8	.2152	6.7	4.93
1.0	.2133	8.8	5.82
1.5	.2124	13.2	6.25
2.0	.2119	17.6	6.50
3.0	.2113	26.3	6.76
4.0	.2104	34.9	7.20
4.2	.2100	36.1	7.40

LE46 (.495"x.2150")

0.0	.2049	0.0	0.00
0.3	.2030	2.8	0.93
0.5	.1990	4.6	2.92
0.8	.1952	6.7	4.85
1.0	.1938	8.9	5.56
1.5	.1927	13.3	6.14
2.0	.1923	17.7	6.36
3.0	.1916	26.4	6.70
3.5	.1911	30.8	6.97
3.9	.1896	33.6	7.75

LE48 (.500"x.2481") $

0.0	.2751	0.0	0.00
0.5	.2732	3.6	0.69
0.8	.2648	6.5	3.88
2.0	.2564	15.2	6.27
4.7	.2562	35.1	7.11

LF42 (.495"x.1790")

0.0	.2440	0.0	0.00
0.2	.2431	2.2	0.37
0.5	.2403	5.6	1.52
0.8	.2370	8.2	2.90
1.0	.2338	10.8	4.70
1.5	.2284	15.9	6.60
2.0	.2266	21.0	7.40
3.0	.2235	31.1	8.80
4.0	.2182	40.0	14.0
4.1	.2080	39.4	16.0

LF44 (.495"x.2090")

0.0	.2057	0.0	0.00
0.4	.2048	3.9	0.43
0.7	.2030	6.7	1.33
1.0	.2003	9.4	2.65
1.5	.1982	13.9	4.72
2.0	.1938	18.3	5.96
3.0	.1919	27.1	6.94
3.5	.1910	31.5	7.40
4.0	.1893	35.7	8.30
4.7	.1784	39.4	14.3

LF46 (.495"x.2210")

0.0	.2611	0.0	0.00
0.5	.2597	4.8	0.53
0.8	.2581	6.8	1.16
1.0	.2554	8.9	2.20
1.5	.2484	13.1	4.98
2.0	.2452	17.2	6.28
2.5	.2437	21.4	6.90
3.0	.2430	25.6	7.17
4.0	.2401	33.7	8.38
4.5	.2341	37.1	10.9

LF47 (.495"x.2163") $

0.0	.2753	0.0	0.00
0.2	.2750	1.9	0.10
0.4	.2730	3.7	0.84
0.8	.2687	7.2	2.42
1.5	.2611	13.1	5.28
2.0	.2587	17.4	6.20

TEXTURED PURE MAGNESIUM POLYCRYSTALS (in plane-strain compression):

ZT1 (.495"x.3953")

0.0	.2430	0.0	0.00
1.0	.2422	5.1	0.33
2.0	.2413	10.1	0.70
3.0	.2402	15.2	1.16
4.0	.2388	20.1	1.74
5.0	.2369	24.9	2.54
5.5	.2358	27.3	3.00
6.0	.2341	29.6	3.73
6.5	.2318	31.7	4.72
6.8	.2270	32.5	6.81

ZT3 (.495"x.2760")

0.0	.2460	0.0	0.00
1.0	.2455	7.3	0.20
2.0	.2446	14.5	0.57
3.0	.2427	21.7	1.35
4.0	.2396	28.5	2.63
4.5	.2375	31.8	3.52
4.7	.2352	33.3	4.50
4.9	.2310	33.7	6.30
4.7	.2258	31.7	8.56

ZT6 (.495"x.2537") $

0.0	.2487	0.0	0.00
0.8	.2484	6.4	0.12
1.5	.2479	11.9	0.32
2.0	.2473	15.8	0.56
3.0	.2460	23.8	1.09
4.4	.2410	33.6	3.15

ZR1 (.495"x.2300")

0.0	.2470	0.0	0.00
0.5	.2462	4.4	0.32
1.0	.2453	8.7	0.69
1.5	.2433	13.0	1.51
2.0	.2408	17.1	2.54
2.5	.2382	21.2	3.60
3.0	.2341	25.0	5.35
3.2	.2286	26.3	7.73
3.1	.2250	24.9	9.33

ZR3 (.495"x.2280")

0.0	.2452	0.0	0.00
0.5	.2447	4.4	0.20
1.0	.2442	8.8	0.41
1.5	.2431	13.2	0.86
2.0	.2404	17.4	1.98
2.5	.2376	21.5	3.15
3.0	.2332	25.3	5.02
3.2	.2277	26.8	7.40
3.3	.2250	26.9	8.61
3.2	.2232	26.3	9.40

ZR6 (.490"x.2454") $

0.0	.2490	0.0	0.00
1.0	.2484	8.3	0.24
2.0	.2446	16.3	1.78
3.0	.2387	23.9	4.22

TR1 (.500"x.2231")

0.0	.2533	0.0	0.00
1.0	.2519	8.9	0.55
2.0	.2486	17.6	1.87
3.0	.2437	25.9	3.85
4.0	.2368	33.6	6.71
4.5	.2321	37.1	9.72
5.0	.2261	40.2	11.4
5.2	.2228	41.4	12.5

TR2 (.500"x.2520")

0.0	.1682	0.0	0.00
1.0	.1676	7.9	0.35
2.0	.1659	15.7	1.37
3.0	.1630	23.1	3.14
4.0	.1589	30.1	5.68
5.0	.1536	36.4	9.07
5.5	.1502	39.2	11.3
6.0	.1430	41.0	16.2
5.9	.1405	40.0	18.0

TR3 (.500"x.2090")

0.0	.1757	0.0	0.00
1.0	.1743	9.5	0.80
2.0	.1717	18.7	2.30
3.0	.1680	27.5	4.48
4.0	.1620	35.4	8.12
4.5	.1583	39.0	10.4
5.0	.1505	41.4	15.5
4.9	.1490	40.6	16.6

TZ1 (.495"x.2483")

0.0	.2451	0.0	0.00
0.5	.2436	4.0	0.61
1.0	.2378	7.9	3.62
1.5	.2327	11.6	5.19
2.0	.2301	15.3	6.30
4.0	.2250	30.0	8.55
5.0	.2213	36.9	10.2
5.3	.2181	38.6	11.7
5.0	.2141	35.9	13.5

TZ2 (.495"x.2471")

0.0	.2381	0.0	0.00
0.5	.2353	4.0	1.18
1.0	.2309	7.9	3.07
1.5	.2254	11.6	5.48
2.0	.2225	15.3	6.77
4.0	.2165	29.9	9.52
5.0	.2130	36.8	11.1
5.4	.2095	39.2	12.8
5.3	.2079	38.2	13.6

TZ3 (.495"x.2487")

0.0	.2591	0.0	0.00
0.5	.2580	4.0	0.42
1.0	.2515	7.9	3.16
1.5	.2462	11.6	5.10
2.0	.2437	15.3	6.13
4.0	.2363	30.0	8.37
5.0	.2348	37.0	9.86
5.5	.2305	40.0	11.7
5.3	.2283	38.2	12.7

RZ1 (.495"x.2490")

0.0	.2171	0.0	0.00
0.5	.2157	4.0	0.64
1.0	.2092	7.9	3.70
1.5	.2044	11.5	6.02
2.0	.2018	15.2	7.30
3.0	.1986	22.5	8.90
3.5	.1965	25.9	9.96
4.0	.1934	29.2	11.6
4.2	.1913	30.4	12.6

RZ2 (.495"x.2480")

0.0	.2249	0.0	0.00
0.5	.2223	4.0	1.16
1.0	.2158	7.8	4.12
1.5	.2115	11.5	6.15
2.0	.2086	15.2	7.52
3.0	.2051	22.5	9.20
3.5	.2032	25.9	10.1
4.0	.2001	29.2	11.7
4.3	.1971	30.6	13.2

RZ3 (.500"x.2485")

0.0	.2179	0.0	0.00
0.5	.2160	4.0	0.87
1.0	.2096	7.7	3.94
1.5	.2052	11.4	6.01
2.0	.2026	15.0	7.28
3.0	.1998	22.2	8.66
3.5	.1981	25.7	9.55
4.0	.1957	29.1	10.7
4.3	.1901	30.1	13.6

RT1 (.500"x.2320")

0.0	.2167	0.0	0.00
1.0	.2156	8.6	0.51
2.0	.2137	17.0	1.40
3.0	.2107	25.2	2.80
4.0	.2044	32.6	5.83
4.5	.1986	35.7	8.70
5.0	.1894	38.0	13.5
5.2	.1828	38.2	17.0
5.1	.1788	36.8	19.3

RT2 (.500"x.2675")

0.0	.2183	0.0	0.00
1.0	.2175	7.4	0.36
2.0	.2161	14.8	1.00
3.0	.2138	22.0	2.08
4.0	.2098	28.8	3.96
5.0	.2006	34.5	8.45
5.5	.1926	36.6	12.5
5.7	.1840	36.7	17.2
5.6	.1805	35.5	19.1

RT3 (.500"x.2700")

0.0	.1929	0.0	0.00
1.0	.1920	7.4	0.46
2.0	.1908	14.7	1.10
3.0	.1886	21.7	2.23
4.0	.1850	28.5	4.18
5.0	.1770	34.1	8.60
5.5	.1707	36.3	12.2
6.0	.1570	36.9	20.6
5.9	.1546	36.1	22.1

TEXTURED Mg-.5%Th POLYCRYSTALS (in plane-strain compression):

Th-ZT1 (.495"x.279")

0.0	.2525	0.0	0.00
1.0	.2521	7.2	0.16
2.0	.2516	14.4	0.35
3.0	.2507	21.6	0.71
4.0	.2484	28.5	1.65
5.0	.2446	35.0	3.16
5.7	.2402	39.3	5.00

Th-ZT2 (.495"x.251")

0.0	.2528	0.0	0.00
1.0	.2521	8.0	0.27
2.0	.2513	16.0	0.59
3.0	.2494	23.8	1.36
4.0	.2459	31.3	2.76
4.5	.2425	34.8	4.20
4.9	.2362	37.1	6.84

Th-ZT3 (.490"x.233")

0.0	.2510	0.0	0.00
1.0	.2503	8.7	0.27
2.0	.2495	17.4	0.60
3.0	.2470	25.8	1.60
4.0	.2423	33.8	3.53
4.6	.2360	37.9	6.16

Th-ZT6 (.490"x.2382) $

0.0	.2541	0.0	0.00
1.0	.2540	8.6	0.03
2.0	.2539	16.1	0.07
3.0	.2530	25.6	0.43
3.8	.2508	32.1	1.31
4.2	.2479	35.1	2.47
4.7	.2402	38.1	5.65

Th-ZR1 (.495"x.250")

0.0	.2526	0.0	0.00
1.0	.2523	8.1	0.12
2.0	.2518	16.1	0.32
3.0	.2507	24.0	0.75
4.0	.2477	31.7	1.96
4.8	.2415	36.8	4.50

Th-ZR2 (.495"x.233")

0.0	.2513	0.0	0.00
1.0	.2509	8.7	0.16
2.0	.2504	17.3	0.36
3.0	.2488	25.8	1.00
4.0	.2454	33.9	2.37
4.5	.2398	37.3	4.70

Th-ZR3 (.500"x.246")

0.0	.2538	0.0	0.00
1.0	.2535	8.1	0.11
2.0	.2531	16.2	0.27
3.0	.2524	24.3	0.55
4.0	.2502	32.0	1.42
4.8	.2413	37.4	5.05

Th-ZR6 (.495"x.2750) $

0.0	.2530	0.0	0.00
1.0	.2489	7.4	0.03
2.0	.2528	14.7	0.07
3.0	.2525	22.0	0.19
3.9	.2512	28.5	0.71
4.3	.2498	30.9	1.28

Th-TR1 (.500"x.217")

0.0	.2463	0.0	0.00
1.0	.2457	9.3	0.24
2.0	.2448	18.6	0.63
3.0	.2436	27.7	1.10
4.0	.2377	35.8	3.61
4.4	.2330	38.4	5.62

Th-TR2 (.495"x.219")

0.0	.2148	0.0	0.00
1.0	.2137	9.2	0.51
2.0	.2122	18.2	1.22
3.0	.2098	27.0	2.35
3.5	.2075	31.2	3.45
4.0	.2031	34.9	5.60
4.5	.1966	38.1	8.85
4.9	.1880	40.1	13.3

Th-TR3 (.500"x.213")

0.0	.2219	0.0	0.00
1.0	.2212	9.3	0.31
2.0	.2201	18.6	0.81
3.0	.2181	27.7	1.73
3.5	.2153	31.9	3.01
4.0	.2095	35.5	5.75
4.5	.2023	38.7	9.25
4.9	.1928	40.2	14.1

Th-TR6 (.500"x.2971) $

0.0	.2320	0.0	0.00
1.0	.2320	6.7	0.00
2.0	.2319	13.5	0.04
3.1	.2314	20.5	0.25
4.0	.2303	26.7	0.73
4.9	.2280	32.1	1.74

Th-TZ1 (.495"x.253")

0.0	.2635	0.0	0.00
1.0	.2629	7.9	0.22
1.5	.2623	11.9	0.45
2.0	.2589	15.7	1.76
2.5	.2515	19.1	4.66
3.0	.2480	22.6	6.07
4.0	.2434	29.6	7.92
5.0	.2390	36.4	9.77
6.0	.2316	42.4	12.9

Th-TZ2 (.490"x.252")

0.0	.2431	0.0	0.00
1.0	.2426	8.1	0.20
1.5	.2418	12.1	0.53
2.0	.2383	15.9	1.98
2.5	.2308	19.3	5.20
3.0	.2276	22.8	6.60
4.0	.2232	29.8	8.55
5.0	.2187	36.7	10.5
5.9	.2100	41.7	14.6

Th-TZ3 (.495"x.253")

0.0	.2508	0.0	0.00
1.0	.2504	7.9	0.15
1.5	.2500	11.9	0.32
2.0	.2468	15.7	1.62
2.5	.2397	19.1	4.53
3.0	.2363	22.6	5.95
4.0	.2323	29.6	7.67
5.3	.2272	38.5	9.90

Th-TZ6 (.490"x.2523) $

0.0	.1952	0.0	0.00
1.0	.1951	8.1	0.05
1.5	.1950	12.1	0.10
1.9	.1949	15.5	0.41
2.1	.1934	16.8	0.93
2.4	.1886	18.8	3.43
3.5	.1826	26.5	6.70

Th-RZ1 (.490"x.253")

0.0	.1957	0.0	0.00
1.0	.1951	8.0	0.30
1.5	.1945	12.0	0.61
2.0	.1903	15.7	2.79
2.5	.1861	19.2	5.02
3.0	.1838	22.8	6.27
4.0	.1807	29.9	8.00
5.0	.1777	36.8	9.65
5.9	.1717	42.1	13.1

Th-RZ2 (.495"x.254")

0.0	.2131	0.0	0.00
1.0	.2125	7.9	0.28
1.5	.2117	11.9	0.66
2.0	.2085	15.6	2.17
2.5	.2032	19.0	4.76
3.0	.2009	22.5	5.90
4.0	.1978	29.6	7.45
5.0	.1947	36.5	9.03
5.7	.1915	40.9	10.7

Th-RZ3 (.495"x.254")

0.0	.2071	0.0	0.00
1.0	.2066	7.9	0.24
1.5	.2061	11.9	0.48
2.0	.2039	15.7	1.56
2.5	.1982	19.0	4.40
3.0	.1956	22.6	5.70
4.0	.1924	29.6	7.36
5.0	.1896	36.5	8.85
5.7	.1871	41.4	10.2

Th-RZ6 (.500"x.253") $

0.0	.2410	0.0	0.00
1.5	.2409	11.8	0.04
2.0	.2399	15.7	0.45
2.3	.2350	17.4	2.52
3.0	.2285	22.5	5.35
4.5	.2221	32.9	8.30

Th-RT1 (.490"x.309")

0.0	.2114	0.0	0.00
1.0	.2111	6.6	0.14
2.0	.2107	13.2	0.33
5.0	.2100	19.7	0.66
4.0	.2075	25.9	1.86
5.0	.2029	31.7	4.10
6.0	.1970	37.0	7.05
7.0	.1898	40.9	12.9
7.8	.1811	44.6	15.5

Th-RT2 (.500x.231")

0.0	.2170	0.0	0.00
1.0	.2164	8.6	0.27
2.0	.2156	17.2	0.64
3.0	.2135	25.6	1.62
4.0	.2073	33.1	4.56
5.0	.1986	39.8	8.87
5.9	.1871	44.5	14.8

Th-RT3 (.495"x.269")

0.0	.2161	0.0	0.00
1.0	.2156	7.5	0.23
2.0	.2151	15.0	0.46
3.0	.2141	22.3	0.93
4.0	.2104	29.3	2.66
5.0	.2045	35.6	5.52
5.6	.2015	39.0	7.00

Th-RT6 (.500"x.2375) $

0.0	.2528	0.0	0.00
1.0	.2528	8.4	0.00
2.0	.2525	16.8	0.11
3.0	.2513	25.1	0.59
3.5	.2500	28.8	1.12
3.8	.2460	31.5	2.73

TEXTURED Mg-4%Li POLYCRYSTALS (in plane-strain compression):

Li-ZT1 (.495"x.232")

0.0	.2573	0.0	0.00
0.5	.2569	4.3	0.15
1.0	.2562	8.7	0.43
1.5	.2549	12.9	0.94
2.0	.2525	17.1	1.90
2.5	.2499	21.2	2.92
3.0	.2465	25.0	4.29
4.0	.2355	32.0	8.84
4.6	.2242	35.1	13.8

Li-ZT2 (.495"x.252")

0.0	.2554	0.0	0.00
1.0	.2545	8.0	0.35
1.5	.2537	12.0	0.67
2.0	.2521	15.8	1.30
2.5	.2501	19.6	2.08
3.0	.2475	23.3	3.15
4.0	.2403	30.2	6.10
5.0	.2256	35.7	12.3

Li-ZT5 (.495"x.270")

0.0	.2569	0.0	0.00
1.0	.2561	7.5	0.31
1.5	.2554	11.2	0.58
2.0	.2543	14.8	1.02
2.5	.2525	18.4	1.73
3.0	.2504	21.7	2.55
4.0	.2445	28.3	4.95
4.9	.2340	33.3	9.33

Li-ZT6 (.500"x.307") $

0.0	.2597	0.0	0.00
1.0	.2595	6.5	0.07
2.0	.2590	13.0	0.27
3.0	.2566	19.3	1.20
4.2	.2500	26.6	3.82

Li-ZR1 (.495"x.241")

0.0	.2541	0.0	0.00
0.5	.2537	4.2	0.15
1.0	.2529	8.3	0.47
1.5	.2517	12.5	0.95
2.0	.2498	16.5	1.72
3.0	.2451	24.3	3.61
4.0	.2355	31.2	7.60
5.0	.2160	36.0	16.2
5.3	.2097	37.3	19.2

Li-ZR2 (.500"x.218")

0.0	.2590	0.0	0.00
0.5	.2586	4.6	0.15
1.0	.2579	9.1	0.42
1.5	.2566	13.6	0.93
2.0	.2543	18.0	1.83
2.5	.2516	22.3	2.90
3.0	.2483	26.4	4.22
4.0	.2346	33.4	9.90
4.4	.2245	35.3	14.4

Li-ZR3 (.485"x.216")

0.0	.2562	0.0	0.00
1.0	.2551	9.5	0.43
2.0	.2513	18.7	1.93
3.0	.2450	27.4	4.47
4.0	.2299	34.5	10.8
4.3	.2220	35.9	14.3

Li-ZR6 (.495"x.2583) $

0.0	.2595	0.0	0.00
1.0	.2594	7.8	0.03
2.0	.2580	15.5	0.58
3.0	.2554	23.1	1.60
4.0	.2498	30.1	3.82

Li-TR1 (.500"x.200")

0.0	.2780	0.0	0.00
0.5	.2770	5.0	0.36
1.0	.2752	9.9	1.01
1.5	.2721	14.7	2.14
2.0	.2665	19.2	4.22
2.5	.2591	23.4	7.04
3.0	.2496	27.1	10.7
3.3	.2435	28.9	13.3

Li-TR2 (.500"x.219")

0.0	.2160	0.0	0.00
0.5	.2152	4.6	0.37
1.0	.2140	9.1	0.93
1.5	.2122	13.5	1.78
2.0	.2088	17.7	3.39
2.5	.2044	21.6	5.52
3.0	.1993	25.4	8.05
3.8	.1872	30.0	14.3

Li-TR3 (.495"x.217")

0.0	.2070	0.0	0.00
1.0	.2054	9.3	0.77
2.0	.2004	18.0	3.24
3.0	.1901	25.7	8.53
3.9	.1770	31.4	15.7

Li-TZ1 (.495"x.259")

0.0	.2551	0.0	0.00
0.5	.2548	3.9	0.11
0.8	.2545	6.2	0.23
1.0	.2539	7.8	0.47
1.5	.2487	11.4	2.55
2.0	.2451	14.9	4.82
3.0	.2357	21.7	7.90
4.0	.2298	28.4	10.5
5.0	.2205	34.0	14.7
6.1	.2020	38.6	23.3

Li-TZ2 (.495"x.258")

0.0	.2390	0.0	0.00
0.5	.2386	3.6	0.16
0.8	.2381	6.2	0.37
1.0	.2375	7.8	0.63
1.5	.2328	11.4	2.64
2.0	.2274	14.9	4.98
3.0	.2206	21.8	8.00
4.0	.2148	28.3	10.7
5.0	.2056	34.0	15.1
5.6	.1970	36.8	19.3

Li-TZ3 (.495"x.259")

0.0	.2332	0.0	0.00
0.5	.2327	3.9	0.21
1.0	.2317	7.8	0.64
1.5	.2277	11.4	2.36
2.0	.2222	14.9	4.83
2.5	.2188	18.3	6.36
3.0	.2158	21.7	7.75
4.0	.2108	28.3	10.1
4.6	.2070	32.3	11.9

Li-TZ6 (.485"x.2587) $

0.0	.2992	0.0	0.00
1.0	.2990	8.0	0.06
1.4	.2978	10.9	0.47
1.6	.2947	12.2	1.52
1.9	.2898	14.3	3.18
2.5	.2830	18.9	5.57

Li-RZ1 (.495"x.257")

0.0	.2011	0.0	0.00
0.5	.2005	3.9	0.29
1.0	.1997	7.8	0.70
1.5	.1969	11.5	2.12
2.0	.1915	15.0	4.89
2.5	.1881	18.4	6.68
3.0	.1854	21.8	8.13
4.0	.1809	28.4	10.6
5.3	.1709	35.8	16.2

Li-RZ2 (.495"x.258")

0.0	.1990	0.0	0.00
0.5	.1985	3.9	0.25
1.0	.1979	7.8	0.55
1.5	.1945	11.5	2.27
2.0	.1896	14.9	4.74
2.5	.1864	18.4	6.55
3.0	.1840	21.8	7.85
4.0	.1797	28.4	10.2
5.4	.1677	36.1	17.1

Li-RZ3 (.490"x.259")

0.0	.2041	0.0	0.00
1.0	.2024	7.9	0.83
2.0	.1951	15.1	4.51
3.0	.1881	21.9	8.17
4.0	.1838	28.6	10.5
4.8	.1790	33.5	13.1

Li-RZ6 (.500"x.2590) $

0.0	.2668	0.0	0.00
0.5	.2667	3.8	0.03
1.0	.2660	7.7	0.30
1.6	.2627	12.5	1.56
1.9	.2575	14.4	3.55
2.9	.2498	20.6	6.59

Li-RT1 (.500"x.288")

0.0	.2108	0.0	0.00
0.5	.2105	3.6	0.14
1.0	.2100	6.9	0.38
1.5	.2091	10.3	0.81
2.0	.2068	13.6	2.10
2.5	.2040	16.8	3.28
3.0	.2006	19.8	4.95
4.0	.1916	25.3	9.55
5.0	.1815	30.2	14.9
5.6	.1750	32.5	18.6

Li-RT2 (.500"x.269")

0.0	.2002	0.0	0.00
0.5	.1999	3.7	0.15
1.0	.1995	7.4	0.35
1.5	.1982	11.0	1.00
2.0	.1959	14.5	2.16
2.5	.1928	17.9	3.76
3.0	.1880	21.0	6.28
4.0	.1795	26.8	10.9
5.1	.1664	32.0	18.5

Li-RT3 (.500"x.275")

0.0	.2175	0.0	0.00
1.0	.2167	7.2	0.36
1.5	.2157	10.8	0.83
2.0	.2137	14.3	1.76
2.5	.2107	17.6	3.18
3.0	.2067	20.8	5.10
4.0	.1968	26.4	10.0
4.9	.1865	30.9	15.4

UNIAXIAL TENSILE AND COMPRESSIVE TESTS OF POLYCRYSTALS

R is specimen dimension in the rolling direction; T is specimen dimension in the transverse direction; Z is specimen dimension in the thickness direction of the textured polycrystalline sheet material. e_R, e_T, and e_Z are calculated true strains in the three respective directions.

Rolling Direction Tensile Test (Pure Mg):

Load (lb)	Stress (ksi)	R (in)	e_R (%)	T (in)	e_T (%)	Z (in)	e_Z (%)
0	0.0	2.600	0.00	.2606	0.00	.2500	0.00
580	8.8	2.621	0.80	.2604	0.07	.2493	0.68
800	12.1	2.634	1.30	.2600	0.23	.2476	0.96
970	14.6	2.650	1.90	.2596	0.38	.2467	1.33
1100	16.5	2.667	2.54	.2590	0.61	.2458	1.70
1165	17.3	2.680	3.03	.2586	0.77	.2452	1.93
1280	18.9	2.705	3.94	.2577	1.12	.2439	2.48
1325	19.4	2.719	4.47	.2573	1.28	.2430	2.86

Transverse Direction Tensile Test (Pure Mg):

0	0.0	.2634	0.00	2.600	0.00	.2500	0.00
730	11.1	.2633	0.03	2.602	0.07	.2499	0.03
910	13.8	.2632	0.07	2.606	0.23	.2498	0.07
1020	15.4	.2629	0.19	2.610	0.38	.2496	0.16
1260	18.9	.2625	0.34	2.625	0.96	.2493	0.28
1385	20.7	.2616	0.68	2.638	1.46	.2485	0.60
1445	21.5	.2613	0.81	2.648	1.83	.2483	0.68
1520	22.5	.2607	1.03	2.664	2.41	.2478	0.88
1530	22.4	.2594	1.53	2.685	3.22	.2471	1.17

Rolling Direction Tensile Test (Mg-.5%Th):

0	0.0	2.600	0.00	.2620	0.00	.2543	0.00
900	13.5	2.605	0.19	.2618	0.07	.2541	0.07
1300	19.5	2.608	0.30	.2617	0.11	.2540	0.11
1700	25.5	2.615	0.57	.2615	0.19	.2537	0.23
1820	27.3	2.630	1.15	.2611	0.34	.2530	0.51
1850	27.7	2.638	1.45	.2605	0.57	.2524	0.75
1870	28.0	2.645	1.72	.2600	0.76	.2520	0.91
1890	28.3	2.652	1.98	.2596	0.92	.2515	1.11
1900	28.4	2.660	2.27	.2591	1.11	.2510	1.30

Transverse Direction Tensile Test (Mg-.5%Th):

0	0.0	.2604	0.00	2.600	0.00	.2537	0.00
800	12.1	.2602	0.07	2.606	0.23	.2533	0.15
1460	22.1	.2600	0.15	2.612	0.46	.2529	0.32
1590	24.0	.2598	0.23	2.620	0.76	.2523	0.55
1640	24.8	.2593	0.42	2.630	1.15	.2518	0.75
1670	25.3	.2589	0.57	2.638	1.45	.2514	0.91
1695	25.6	.2584	0.77	2.647	1.79	.2510	1.07
1705	25.7	.2581	0.89	2.654	2.06	.2506	1.23
1725	25.8	.2575	1.12	2.664	2.44	.2502	1.38

Rolling Direction Tensile Test (Mg-4%Li):

0	0.0	2.610	0.00	.2586	0.00	.2579	0.00
800	12.0	2.618	0.30	.2584	0.07	.2577	0.07
900	13.4	2.631	0.80	.2578	0.31	.2572	0.27
960	14.2	2.641	1.18	.2572	0.54	.2569	0.38
1000	14.8	2.649	1.49	.2567	0.74	.2566	0.50
1055	15.5	2.662	1.98	.2559	1.05	.2562	0.66
1085	15.9	2.670	2.26	.2555	1.21	.2559	0.78

Transverse Direction Tensile Test (Mg-4%Li):

0	0.0	.2612	0.00	2.600	0.00	.2608	0.00
500	7.3	.2611	0.03	2.603	0.11	.2607	0.03
685	10.0	.2607	0.19	2.613	0.50	.2601	0.26
740	10.9	.2605	0.26	2.620	0.76	.2599	0.34
820	11.9	.2599	0.50	2.631	1.19	.2594	0.53
880	12.7	.2594	0.69	2.643	1.64	.2590	0.69
935	13.4	.2584	1.08	2.655	2.08	.2586	0.85

Rolling Direction Compression (Pure Mg):

0	0.0	.2685	0.00	.2991	0.00	.2450	0.00
280	3.8	.2668	0.63	.2995	0.13	.2473	0.93
350	4.7	.2637	1.80	.2998	0.23	.2513	2.53
450	5.9	.2599	3.25	.3006	0.50	.2550	3.98
600	7.8	.2569	4.41	.3018	0.90	.2590	5.55
900	11.6	.2527	6.06	.3030	1.30	.2630	7.10

Transverse Direction Compression (Pure Mg):

0	0.0	.2563	0.00	.3070	0.00	.2499	0.00
200	3.1	.2566	0.11	.3065	0.16	.2506	0.28
300	4.6	.2571	0.31	.3037	1.08	.2539	1.60
450	6.8	.2583	0.78	.2990	2.63	.2589	3.56
700	10.5	.2608	1.74	.2933	4.57	.2632	5.18
1000	14.8	.2620	2.18	.2900	5.70	.2660	6.23

Thickness Direction Compression (Pure Mg):

0	0.0	.2671	0.00	.3031	0.00	.2470	0.00
400	4.9	.2674	0.11	.3032	0.03	.2467	0.12
800	9.9	.2698	1.01	.3042	0.36	.2450	0.81
1000	12.2	.2721	1.86	.3060	0.95	.2433	1.52
1200	14.5	.2744	2.69	.3063	1.05	.2417	2.17
1500	17.9	.2782	4.05	.3079	1.57	.2388	3.37
1700	20.1	.2820	5.43	.3095	2.08	.2363	4.42

Rolling Direction Compression (Mg-.5%Th):

0	0.0	.2780	0.00	.2979	0.00	.2500	0.00
800	10.7	.2779	0.03	.2979	0.00	.2500	0.00
1160	15.6	.2770	0.36	.2980	0.03	.2521	0.84
1225	16.2	.2735	1.64	.2983	0.13	.2562	2.46
1400	18.1	.2680	3.69	.2994	0.50	.2604	4.07
1700	21.4	.2580	7.43	.3009	1.00	.2642	5.52

Transverse Direction Compression (Mg-.5%Th):

0	0.0	.2780	0.00	.3077	0.00	.2500	0.00
1000	14.4	.2781	0.03	.3061	0.52	.2520	0.80
1100	15.8	.2781	0.03	.3052	0.81	.2536	1.44
1200	16.9	.2786	0.21	.3020	1.87	.2572	2.86
1400	19.3	.2797	0.61	.2948	4.28	.2622	4.77
1800	24.4	.2820	1.43	.2889	6.30	.2670	6.60

Thickness Direction Compression (Mg-.5%Th):

0	0.0	.2800	0.00	.2990	0.00	.2512	0.00
500	6.7	.2799	-.03	.2990	0.00	.2510	0.08
1000	13.3	.2799	-.03	.2990	0.00	.2509	0.11
1600	21.3	.2802	0.07	.2995	0.16	.2503	0.35
2000	26.4	.2814	0.50	.3012	0.73	.2485	1.08
2500	32.3	.2849	1.75	.3054	2.12	.2436	3.08

Rolling Direction Compression (Mg-4%Li):

0	0.0	.2908	0.00	.3000	0.00	.2511	0.00
810	10.7	.2895	0.44	.3004	0.13	.2521	0.39
900	11.7	.2856	1.82	.3015	0.50	.2552	1.63
1000	12.9	.2829	2.75	.3025	0.83	.2579	2.66
1200	15.2	.2770	4.86	.3037	1.23	.2620	4.25
1600	19.8	.2700	7.43	.3055	1.83	.2680	6.51

Transverse Direction Compression (Mg-4%Li):

0	0.0	.2870	0.00	.3069	0.00	.2502	0.00
700	9.7	.2873	0.10	.3053	0.52	.2520	0.71
850	11.6	.2887	0.59	.3002	2.20	.2559	2.22
1000	13.5	.2892	0.76	.2977	3.04	.2579	3.00
1250	16.4	.2910	1.38	.2890	6.00	.2648	5.67
1600	20.6	.2920	1.73	.2832	8.03	.2689	7.20

Thickness Direction Compression (Mg-4%Li):

0	0.0	.2860	0.00	.3011	0.00	.2540	0.00
1000	11.6	.2867	0.24	.3018	0.23	.2532	0.31
1300	15.0	.2872	0.41	.3030	0.63	.2517	0.91
1700	19.3	.2891	1.08	.3052	1.36	.2483	2.25
2000	22.5	.2911	1.78	.3077	2.14	.2461	3.15
2400	26.3	.2951	3.12	.3130	3.87	.2394	5.90